

# Control of pulsed light propagation through multimode optical fibers

THÈSE N° 7590 (2017)

PRÉSENTÉE LE 17 MARS 2017

À LA FACULTÉ DES SCIENCES ET TECHNIQUES DE L'INGÉNIEUR  
LABORATOIRE DE DISPOSITIFS PHOTONIQUES APPLIQUÉS  
PROGRAMME DOCTORAL EN PHOTONIQUE

ÉCOLE POLYTECHNIQUE FÉDÉRALE DE LAUSANNE

POUR L'OBTENTION DU GRADE DE DOCTEUR ÈS SCIENCES

PAR

Edgar Emilio MORALES DELGADO

acceptée sur proposition du jury:

Prof. Y. Bellouard, président du jury  
Prof. C. Moser, directeur de thèse  
Prof. E. Bossy, rapporteur  
Prof. H. Giessen, rapporteur  
Prof. D. Psaltis, rapporteur



ÉCOLE POLYTECHNIQUE  
FÉDÉRALE DE LAUSANNE

Suisse  
2017



# Acknowledgements

*I would like to start by thanking my thesis director Professor Christophe Moser for believing in me and letting me undertake this challenging project. Thank you for your enlightening guidance and support during this last four years and for the great research environment in the LAPD lab. I also want to thank Professor Demetri Psaltis for trusting in our project, for his helpful discussions and delightful collaboration. Without his support and access to the facilities of his laboratory, this project wouldn't have reached the great impact and scope achieved.*

*I also want to thank Salma Farahi and Ioannis Papadopolous, former postdocs in LAPD and LO at EPFL, for their guidance and inspiration at the beginning of my PhD.*

*I take the opportunity to thank all the past and present LAPD lab members. Thank you all for making such a nice and enjoyable experience in the lab. I also want to thank my friends from the surrounding labs LO, LOB and LBP. Thanks guys for the fun experiences outside EPFL.*

*Aprovecho la oportunidad para agradecer a Estefany Reyes por su incondicional apoyo, paciencia e increíbles y maravillosas experiencias que hemos vivido juntos estos últimos años. También agradezco a mis padres Gloria y Eduardo y a mi hermano Eduardo por su ejemplo y eterno apoyo a lo largo de mi existencia.*

*Finalmente, ahora que me encuentro en la etapa culminante de mis estudios, me gustaría agradecer a las instituciones de mi país que me ayudaron a llegar hasta este punto: A la Universidad Nacional Autónoma de México por brindarme la mejor educación en el país de manera pública y gratuita y al Consejo Nacional de Ciencia y Tecnología por su apoyo.*

*Emilio Morales, 8th of January 2017. Lausanne, Switzerland*





And God said, Let there be light: and there was light.



# Abstract

Visualization of organs and cells in the interior of living beings is a challenging task due to the light absorption and multiple light scattering occurring in biological tissue that prevents the direct transmission of images. A standard visualization approach is based on the use of endoscopes which is accomplished through apertures in the body. Since their invention, the light transmission capability of optical fibers has enabled fiber optic based endoscopy with devices based on bundles of optical fibers that can directly relay images. Due to their small diameter, fiber optic endoscopes are standard in minimally invasive applications either with a white light illumination or as a fluorescent imaging device. The principle behind fluorescent endoscopy consists on the scanning of light intensity over a fluorescent sample, which is achieved by sequential illumination of each one of the fiber bundles or by mechanical scanning of a single-mode double-cladding fiber. Collecting the fluorescent signal through the light guiding medium, an image can be reconstructed. The main drawback of fiber bundle endoscopes is the pixelated limited resolution given by the presence of thousands of cores that conform the bundle. In the double cladding fiber endoscopes, there is a limit to the miniaturization of the endoscope due to the requirement of mechanical elements at the tip of the fiber to scan the illumination over the sample.

In this thesis, methods for focusing and digital scanning of optical light pulses through multimode optical fibers without any distal mechanical element are developed. Such techniques are based on spatial light modulation. Spatial phase modulation allows the control of light propagation in scrambling media, as in a multimode fiber, enabling the generation of intensity light foci or arbitrary intensity profiles. The high intensity of the transmitted pulses permits multiphoton imaging through multimode optical fibers, resulting in imaging probes of higher resolution than in the case of fiber bundles. We demonstrate in a working prototype that this approach provides all the advantages of multiphoton microscopy at the tip of an ultra-thin probe, such as a reduced photo bleaching of the sample, optical sectioning and enhanced image contrast.

The developed methods can also be employed for material processing that requires high intensity light pulses. In specific, we demonstrate additive manufacturing, also known as 3D printing, at the tip of an ultra-thin needle. The working principle is based on two-photon polymerization, which is accomplished by scanning intense light pulses on a photosensitive material that hardens when exposed to light. All other additive manufacturing methods require very large nozzles or components in close proximity to the structure that they build, up to now. With an ultra-thin 3D printing probe we enable micro-fabrication through very small apertures, in places of difficult access or in the interior of living beings. We call it, endofabrication.

**Keywords:** Fiber optic endoscopy, multimode fiber endoscopy, 3d printing, endofabrication, digital holography, wavefront shaping

# Zusammenfassung

Die Visualisierung von Organen und Zellen im Inneren der Lebewesen ist eine anspruchsvolle Aufgabe. In biologischem Gewebe ist die direkte Übertragung von Bildern aufgrund der Absorption von Licht und der Lichtstreuung nicht möglich. Ein gemeinsamer Visualisierungsansatz basiert auf der Verwendung von Endoskopen. Die Lichtdurchlässigkeit von optischen Fasern ermöglicht die Endoskopie mit Faserbündeln, die direkt Bilder übertragen können. Der kleine Durchmesser von Lichtwellenleitern erlaubt die Übertragung von Bildern mit einer Weißlicht-Beleuchtung oder mit Fluoreszenz auf minimal-invasive Weise. Das Prinzip der fluoreszierenden Endoskopie besteht in der Abtastung von Licht in einer fluoreszierenden Probe. Das Fluoreszenzsignal wird durch die optische Faser gesammelt. Auf diese Weise wird ein Bild rekonstruiert. Bei den Lichtleitfaserbündeln erfolgt die Abtastung durch sequentielle Beleuchtung der einzelnen Fasern. Dies führt zu einer Pixilierung und begrenzt die Auflösung aufgrund des Vorhandenseins mehrerer Fasern im Faserbündel. Bei Einmodenfasern mit doppelter Ummantelung erfordert das Abtasten distale mechanische Elemente, um die Beleuchtung in Bezug auf die Probe zu bewegen. Das Vorhandensein von Abtastelementen schränkt die Miniatürisierung des Endoskops ein.

In dieser Arbeit werden Verfahren zur Fokussierung und Abtastung von Lichtpulsen durch Multimode-Lichtleitfasern entwickelt. Die Techniken basieren auf der räumlichen Lichtmodulation. Die räumliche Phasenmodulation ermöglicht die Steuerung der Lichtausbreitung in opaken Medien, wie bei einer Multimode-Lichtleitfaser, die die Erzeugung beliebiger Intensitätsprofile ermöglicht. Die hohe Intensität der gesendeten Impulse erlaubt die Zwei-Photonen-Bildübertragung durch Multimode-Lichtleitfasern. Dies ermöglicht Sonden für eine Bildübertragung mit einer höheren Auflösung als mit Faserbündeln. Wir demonstrieren in einem Prototyp, dass dieser Ansatz alle Vorteile der Multi-Photonen-Mikroskopie an der Spitze einer ultradünnen Nadel bietet.

Die in dieser Arbeit entwickelten Methoden können auch für die Materialbearbeitung genutzt werden. Im Einzelnen zeigen wir den 3D-Druck mit einer ultradünnen Nadel. Das Arbeitsprinzip beruht auf der Zwei-Photonen-Polymerisation. Bei diesem Ansatz härt optische Lichtpulse, die auf ein lichtempfindliches Material fokussiert sind, das Material aus. Alle anderen 3D-Druckverfahren verwenden große Düsen oder sehr große Komponenten in der Nähe der Struktur, die sie bauen. Mit unserer ultra-dünnen 3D-Drucksonde ermöglichen wir die Mikro-Fertigung durch sehr kleine Öffnungen, an schwer zugänglichen Stellen oder im Inneren von Lebewesen. Wir nennen es, dreidimensionale Endodruck.

**Stichwörter:** Faseroptische Endoskopie, Multimode-Faser-Endoskopie, 3D-Drucken, Endodruck, Digitale Holographie, Wellenfront-Formgebung.



# Contents

<b>Acknowledgements.....</b>	<b>iii</b>
<b>Abstract.....</b>	<b>vii</b>
<b>Zusammenfassung .....</b>	<b>ix</b>
<b>Contents .....</b>	<b>xi</b>
<b>List of Figures.....</b>	<b>xiv</b>
<b>Chapter 1 Introduction.....</b>	<b>19</b>
1.1 General introduction.....	19
1.2 Thesis objectives .....	21
1.3 Thesis outline .....	22
1.4 List of published articles .....	23
1.4.1 Presentations in international conferences .....	23
1.4.2 Peer reviewed publications .....	24
1.5 References .....	24
<b>Chapter 2 Control of pulsed light propagation in multimode fibers.....</b>	<b>27</b>
2.1 Light propagation in free space and scattering media .....	27
2.2 Propagation of ultrafast pulses in MMFs.....	29
2.2.1 Characteristics of optical pulses .....	29
2.2.2 Ray trace approach of light propagation in MMFs.....	30
2.2.3 Electromagnetic wave approach for light propagation in MMFs.....	33
2.2.4 Material dispersion.....	35
2.2.5 Modal dispersion .....	36
2.3 Focusing light using the transmission matrix.....	37
2.3.1 Experimental setup for the measurement of the transmission matrix.....	39
2.3.2 Advantages and limitations of the transmission matrix approach.....	44
2.4 Control of pulsed light propagation using time-gated digital phase conjugation .....	45
2.4.1 Time-grated digital phase conjugation in step and graded index MMFs.....	48
2.5 Applications.....	49
2.6 Limits of controlled light propagation in multimode fibers.....	49
2.6.1 Fiber bending.....	49
2.6.2 Spatial light modulators.....	50

---

2.7	References .....	50
<b>Chapter 3</b>	<b>Focusing optical pulses through multimode fibers.....</b>	<b>54</b>
3.1	Introduction .....	54
3.2	Experimental setup for selective modal excitation .....	56
3.2.1	Chirped pulse amplification .....	56
3.2.2	Calibration – mode selection.....	57
3.2.3	Delivery of focused pulses (reconstruction).....	60
3.3	Temporal characterization of the delivered focused pulses .....	63
3.4	Spatial scanning and temporal multiplexing of the focused pulses .....	65
3.4.1	Light scanning through the multimode fiber.....	65
3.4.2	Temporal multiplexing through the multimode fiber .....	66
3.4.3	Spatial multiplexing through the multimode waveguide .....	67
3.5	Discussion and conclusions.....	68
3.6	References .....	68
<b>Chapter 4</b>	<b>The multimode fiber two-photon endoscope .....</b>	<b>71</b>
4.1	Introduction to optical fiber-based endoscopy .....	72
4.2	Focusing pulses through the multimode fiber.....	73
4.2.1	Calibration .....	74
4.2.2	Reconstruction.....	74
4.3	Scanning focused pulses through the multimode fiber.....	76
4.3.1	Spatial characterization .....	76
4.3.2	Temporal characterization.....	77
4.4	Imaging through the multimode fiber .....	79
4.4.1	Two-photon imaging.....	79
4.4.2	First demonstration of two-photon imaging through a multimode fiber .....	80
4.4.3	Imaging of fluorescent beads through the multimode fiber .....	81
4.4.4	Characterization and compensation of the non-uniform resolution over the field of view .....	83
4.4.5	Imaging of biological samples with the two-photon multimode fiber endoscope .....	85
4.4.6	Increasing the resolution of the multimode fiber endoscope.....	87
4.4.7	Two-photon imaging of biological samples with the multimode fiber endoscope .....	90
4.5	Conclusions .....	93
4.6	Acknowledgements.....	94



---

4.7	References .....	94
<b>Chapter 5</b>	<b>3D printing through a multimode fiber .....</b>	<b>97</b>
5.1	Introduction to photo-polymerization.....	97
5.2	Principle of two-photon polymerization.....	99
5.3	Demonstration of two-photon polymerization with a microscope objective .....	101
5.4	Two-photon polymerization through the multimode fibre .....	103
5.5	Two-photon polymerization at the tip of a needle.....	106
5.6	The multimode fiber as a 3D printer.....	109
5.7	Discussion on pulsed light focusing through MMFs .....	110
5.8	Conclusions .....	111
5.9	Acknowledgements.....	112
5.10	References .....	112
<b>Chapter 6</b>	<b>Conclusions and future work .....</b>	<b>117</b>
6.1	Achieved results.....	117
6.2	Future work.....	118
6.3	References .....	119
	<b>Curriculum Vitae .....</b>	<b>121</b>

# List of Figures

Figure 1:1 Lens systems for optical endoscopes. (a) Conventional system with glass lenses invented by Nitze in 1877. (b) Hopkins rod-lens system [2].	19
Figure 1:2 Optical fiber endoscopes. (a) Double clad fiber system. Mechanical elements are required to scan the illumination on the sample. (b) Fiber bundle system. Each core relays a “pixel” of the distal scene. (c) Multimode fiber system. Using wavefront shaping, light point scanning on the specimen followed by the collection of the fluorescent signal allows fluorescent imaging.	20
Figure 2:1 Representation of a phase-conjugate mirror. (a) Normal mirror. (b) Phase conjugate mirror.	28
Figure 2:2 A transform-limited Gaussian pulse of 8 fs pulse length at a central wavelength of 800 nm.	30
Figure 2:3 Linearly chirped optical pulses. (a) An 8 fs optical pulse after propagation in 0.7 mm of Silica at a central wavelength of 800 nm. (b) Same as a, but after propagation through a material with the opposite sign of dispersion.	30
Figure 2:4 (a) Step index fiber. (b) Graded index fiber.	31
Figure 2:5 Ray tracing in a step index optical fiber.	32
Figure 2:6 Ray tracing in a graded index optical fiber.	33
Figure 2:7 Intensity profile of some $LP_{lm}$ modes.	34
Figure 2:8 intensity scrambling in MMFs. Light is focused with a 40X microscope objective on one end producing the shown scrambled intensities. The fiber is 200 $\mu\text{m}$ fiber in core diameter. From top left to lower right the excitation is scanned in a 20 $\mu\text{m}$ step along the cross section at the optical axis of the fiber, starting 10 $\mu\text{m}$ off centered. Scale bar is 40 $\mu\text{m}$ .	35
Figure 2:9 Plot of the mode velocity as a function of the l and M indices. There are group of modes that travel at the same speed. The control of such mods can lead to interference phenomena such as light focusing and projection of patterns.	37
Figure 2:10 Measurement of a transmission matrix of a multimode optical fiber. (a) Transmission matrix measurement. (b) Inversion of the transmission matrix and modulation at the input to generate the target intensity distribution at the output of the fiber.	38
Figure 2:11 Experimental setup to perform a measurement of the transmission matrix of a multimode optical fiber. The depicted delay line is only implemented when a pulsed source is used.	40
Figure 2:12 Off-axis holographic arrangement for the measurement of a complex field. (a) Digital hologram. (b) Fourier transform of the digital hologram. (c) Reconstructed phase from the first order of the digital hologram (Inverse Fourier transform of the filtered first order). (d) Reconstructed phase with shifted spectrum to the zero order (k vector removed) (e) Reconstructed amplitude.	41
Figure 2:13 Common path principle for the measurement of a complex field. (a) A basis function is modulated on the SLM with together with four different reference phases in independent sequential measurements. (b) For each one of the referenced input functions the intensity on the other fiber end is measured. (c) Using Equation 2:25 phase and amplitude of the distal field is calculated.	42
Figure 2:14. Light focusing using the transmission matrix method. Spot size is 8.5 $\mu\text{m}$ . (a) Example of a phase conjugated intensity spot generated using a measured transmission matrix. (b) Similar to (a) but using singular value decomposition for noise reduction (20% of inverted singular values were discarded). Enhancement denotes the spot to background intensity ratio.	43
Figure 2:15. Enhancement of a focused spot using the noise reduced matrix inversion.	44

Figure 2:16. Optical phase conjugation in a multimode optical fiber. A light beam is focused in the facet of a multimode fiber generating a speckle pattern on the other side. With a Phase conjugate mirror, light counter propagates through the fiber converging at the location of the initial focus or intensity pattern.	45
Figure 2:17. Characterization of the complex field at the multimode fiber output using off-axis digital holography. The figure describes the characterization in the general case in which the laser beam can be either monochromatic or a pulsed light source. In the pulsed case the reference not only interferes to acquire the hologram, but also acts as a time-gating window.	46
Figure 2:18. Off-axis digital holography. (a) Digital hologram. (b) Fourier transform of the digital hologram. All holographic terms are separated in the spectral domain. Fiber diameter is 200 micrometers.	47
Figure 2:19. Reconstruction of the phase-conjugate replica of the characterized field. Light counter propagates through the fiber generating the original excitation.	47
Figure 2:20. Time-gated digital phase conjugation in a step multimode optical fiber. (a) Intensity profile on the other side of the fiber when a large mode excitation is modulated on the SLM. (b) Intensity profile on the other side of the fiber when a phase-conjugate modulation is performed by the SLM. (c) Interferometric cross correlation between a reference beam and the fiber beam. Time gated DPC excites modes with the same modal speed giving a shorter temporal profile of coherence. (Not to confuse with pulse length). Fiber is step index multimode 200 $\mu\text{m}$ core, NA=.39, length= 30 cm, $\eta = 10$ , Spot size 13.8 $\mu\text{m}$ .	48
Figure 2:21. Time-gated digital phase conjugation in a graded-index multimode optical fiber. (a) Intensity profile on the other side of the fiber when a large mode excitation is modulated on the SLM. (b) Intensity profile on the other side of the fiber when a phase-conjugate modulation is performed by the SLM. (c) Interferometric cross correlation between a reference beam and the fiber beam. Time gated DPC excites modes with the same modal speed giving a shorter temporal profile of coherence. (Not to confuse with pulse length). The temporal profile of the random phase is shorter than in the step index case due to the reduced modal dispersion of graded index fibers. Fiber is graded index, multimode, core diameter 200 $\mu\text{m}$ , NA = 0.27, length = 30 cm, $\eta = 1'100$ , 5 $\mu\text{m}$ spot size.	49
Figure 2:22. Types of spatial light modulators. (a) Phase only SLM (Holoeye AG). (b) DMD (Texas Instruments). (c) Deformable mirror (Adaptive Optics and Astronomy Pierre-Yves Madec). (d) Piston based phase modulator (Fraunhofer Institute).	50
Figure 3:1 Chirped pulse amplification.	56
Figure 3:2 Pulse stretcher.	57
Figure 3:3 Pulse compressor.	57
Figure 3:4 Experimental Setup. Calibration step. The beam from the CPA unit is divided by a polarizing beam splitter PBS into a reference and an object beam. The object beam is coupled into the multimode fiber by a 20X microscope objective OBJ2. The output of the fiber is imaged on the infrared Camera 1 by a 20X microscope objective (OBJ1) and the lens (L1), $f=150$ mm, where it is interfered with the reference beam obtained by reflection from the beam splitter BS1. For each delay $\tau$ , a digital hologram is recorded. Reconstruction step. The time-sampled field is reconstructed by the reference and phase conjugated using a spatial light modulator SLM. The reconstruction is imaged on the fiber by the lens L1 and the 20X microscope objective OBJ1. The reconstructed field counter-propagates generating the short focused spot on the distal side of the fiber. This spot is imaged on Camera 2 using a 4f system (OBJ2 and lens L2, $f=300$ mm). Moreover, the spatio-temporal duration of the phase conjugated spot and its surrounding background is measured on each pixel of a silicon-based detector (Camera 3) using second order (interferometric) autocorrelation, by introducing on the reference the collinear time-delayed replicas required for this measurement, using the Michelson interferometer. The non-linearity in the second order autocorrelation is a two-photon process occurring in the silicon camera. The dashed polygon encloses a possible embodiment of an imaging device based on our method.	58
Figure 3:5 Propagation and characterization of an ultrashort pulse through a multimode fiber. (a) Optical intensity as seen on the proximal end (Camera 1) containing the superposition of the excited modes arriving at all times. (b) Normalized optical power of (a) over the whole area of the Camera 1 as a function of time.	

(c)-(f) Time-gated snapshots of the sampled field (Eq. (3)) taken at times  $\tau_1=2.9$  ps,  $\tau_1=7.7$  ps,  $\tau_1=13.3$  ps, and  $\tau_1=15.1$  ps respectively. Scale bars are 25  $\mu\text{m}$ . Dashed circles indicate the edge of the multimode fiber core. ....59

Figure 3:6 Spatio-temporal characterization of the reconstructed phase conjugated spot. (a)-(d) intensity of the spatial profile measured with Camera 2 and (e) temporal profile of the phase conjugated spots generated from the reconstructed holograms of Fig. 2(c)-(f) taken at time delays  $\tau_1$  equal to 2.9 ps, 7.7 ps, 13.3 ps, and 15.1 ps respectively.  $\tau_1$  denotes the time at which the hologram was recorded and  $t$  is the time dependence of the intensity autocorrelation trace of the phase conjugated spot. (f) Size of the phase conjugated spot as a function of  $\tau_1$ . Points represent experimental data and the solid curve a polynomial fit.60

Figure 3:7 Reconstructed amplitude and spectrum of the time gated fields. Gating occurs at time delays equal to 0.64, 10.88, and 21.12 ps. (Left) Reconstructed amplitude of the time-gated field. (Center) Fourier transform of the digital hologram (only the first order term is shown). (Right) Optical power at different time delays. ....61

Figure 3:8 Example of a phase conjugated spot using the proposed selective mode launching process. (a) Intensity of the phase conjugated spot generated at the distal end as seen on camera 2. (b) Temporal profile (coherence length) comparison with (red curve) and without (blue curve) using selective mode launching. The temporal coherence of the phase conjugated spot is 515fs. The temporal coherence of the pulse without using wavefront control is 5ps. Scale bars are 30 $\mu\text{m}$ . Dashed circles indicate the edge of the core of the multimode fiber. ....63

Figure 3:9 Comparison between the excitation of a large number of modes and the selective DPC method. (a) Intensity when many fiber modes are excited. (b) Intensity of a phase conjugated spot generated using DPC. The size of the spot is 7  $\mu\text{m}$  and is 16 times more intense than the background. (c) and (d) are the spatio-temporal maps of pulse duration when many fiber modes are excited and when DPC is performed respectively. (e) Envelope of the second order autocorrelation trace of the delivered pulse for the excitation of many fiber modes (black curve, averaged over the camera area) and for the DPC case (blue curve, averaged over the FWHM of the spot size). Dashed red lines are their respective Gaussian fit. The broad pulse (black curve) was scaled to enhance its visibility on the graph. Both pulses possess the same energy. Scale bars are 25  $\mu\text{m}$ . Yellow circles on (a), (b), (c), and (d) indicate the edge of the core of the multimode fiber. ..65

Figure 3:10 Two-photon measurement of the phase conjugated spot. (a) Two-photon signal versus normalized power produced by the phase conjugated spot measured on a silicon-based detector (Camera 3 in the setup). Measured (black curve) and theoretical curve (dashed red curve). (b) Two-photon phase conjugated spot. The spot size is 5  $\mu\text{m}$ . The contrast ratio between the maximum intensity to the average background is 270. ....65

Figure 3:11 Scanning of the phase conjugated focus. The pulsed intensity focused can be generated at different locations. Scale bars are 25  $\mu\text{m}$ . ....66

Figure 3:12 Generation of two time multiplexed phase conjugated spots. The time envelope is measured by time-gated interferometry (solid curve). The phase conjugated pulses are centered at  $t=2.9$  ps and  $t=7.7$  ps respectively. Dashed curves: second order autocorrelation envelopes of phase conjugated pulses 1 and 2. Their pulse widths are 500 fs and 800 fs respectively. ....67

Figure 3:13 Generation of two simultaneous spots through fiber bundles. (a) 6'000 cores fiber. FWHM spot size=4.3 $\mu\text{m}$ .  $\eta=139$ . (b) 17'000 cores fiber. FWHM spot size=4.3 $\mu\text{m}$ ,  $\eta=102$ . (c) 6'000 cores fiber.  $\eta=135$ , 119. (d) 17'000 cores fiber.  $\eta=73$ . ....68

Figure 4:1 Conventional fiber endoscopes. (a) Double clad fiber endoscope. (b) Multi-core or fiber bundle endoscope. ....72

Figure 4:2 Experimental setup for multimode fiber endoscopy. ....74

Figure 4:3 Interferometer for pulse width measurement. ....75

Figure 4:4 Scanning of the focused spot at the fundamental wavelength of 800 nm. (a) Sequential superposition of a focused pulse scanned in a 80x80  $\mu\text{m}$  field of view. Scanning step is 4  $\mu\text{m}$ . (b) Intensity enhancement of the focused pulse as a function of scanning position. (c) FWHM size of the focused pulses as a function of scanning position. ....76

tion of scanning position. (d) Line profile of (b) at the location of the dashed lines. (e) Line profile of (c) at the location of the dashed lines. Scale bars are 10 $\mu\text{m}$ . The dashed orange circle represents the core of the multimode fiber. ....	77
Figure 4:5 Pulse width characterizations. (a) Intensity autocorrelation of the delivered pulse when no wave-front control is used. (b), (c) Sample interferometric autocorrelation traces of the central focused pulses with and without GVD compensation respectively. (d) Pulse width vs position.....	79
Figure 4:6. Intensity characterization of light focus through the fiber. (a) Line of focused spots. (b) Intensity enhancement of the focused spots shown in (a). Scale bar is 10 $\mu\text{m}$ . ....	79
Figure 4:7 The first two-photon image acquired through a multimode optical fiber. (a) Bright-field transmission image using a 40x objective. (b) Two-photon excitation image through a 200 micrometer core multimode fiber. The bead looks dark because, in this case, the surrounding medium is fluorescent and the bead is not. The yellow circle represents the scanning window used for the acquisition of the two-photon image. ....	81
Figure 4:8 3D volume of fluorescent beads suspended in non-fluorescent PDMS. ....	81
Figure 4:9 Two-photon images of fluorescent beads. Scanning volume is 28x49x50 $\mu\text{m}$ . Scale bars are 10 $\mu\text{m}$ . ....	82
Figure 4:10 Two-photon images of fluorescent beads. (Left) y-z plane, (right) x-z.....	83
Figure 4:11 Normalized fluorescent photons as a function of position. Scale bar is 10 $\mu\text{m}$ . ....	84
Figure 4:12 Experimental PSF of the multimode fiber imaging system. (a) Single-photon fluorescence. (b) Two-photon fluorescence. (c) Normalized PSF of (a) and (b) at $y = 0$ . ....	85
Figure 4:13 Multimode fiber probe. The white horizontal lines are the reflection of the lamp of the microscope. The fiber is 20 cm length (only the lensed side of the fiber is shown).....	86
Figure 4:14 Imaging of biological tissue through the multimode fiber. (Above) Bright field transmission image of the sample. (Below) Sectioned images acquired through the multimode fiber. ....	87
Figure 4:15 Multimode fiber lensed with a half-ball lens. (a) Graded index multimode fiber with a half sphere attached to one end. Fiber length is 5 cm. (b) Proximal side of the fiber endoscope. (c) Distal side of the fiber endoscope. The white circle in the center of the half sphere is the reflection of the lamp of the microscope used to acquire the image. ....	88
Figure 4:16 Preferred embodiment of the fiber lensed with a half-ball or semi-sphere lens. In terms of optical performance this arrangement is equivalent to the one shown in Figure 4:15 (a). This embodiment could not be attached with conventional methods.....	88
Figure 4:17 Calculated NA versus lateral x position for the MMF lensed with a half-sphere sapphire lens shown in Figure 4:15. The calculation starts at the working distance with the highest resolution ( $wd = 180 \mu\text{m}$ ). ....	89
Figure 4:18 Calculated axial resolution versus lateral x position of the multimode fiber endoscope shown in Figure 4:15. ....	89
Figure 4:19 Calculated lateral resolution versus lateral x position of the multimode fiber endoscope shown in Figure 4:15. ....	90
Figure 4:20 Two-photon imaging configuration. ....	90
Figure 4:21 White light transmission image of the mouse cochlea. ....	91
Figure 4:22 Two-photon images of the stained mouse cochlea acquired with the multimode fiber endoscope. The circle structures are the hearing cells. These are the raw images, no image processing or noise reduction filter has been applied. Scale bars are 9 $\mu\text{m}$ . ....	91
Figure 4:23 White light transmission image of the mouse cochlea. ....	92

Figure 4:24 Two-photon images of the stained mouse cochlea over an extended field of view acquired with the multimode fiber endoscope. The circle structures are the hearing cells. These are the raw images, no image processing or noise reduction filter has been applied. Scale bars are 14 $\mu\text{m}$ .	92
Figure 4:25 Two-photon images of the stained mouse cochlea acquired with a commercial two-photon microscope (Leica TSC SP5 multiphoton microscope). The rounded structures are the hearing cells. Scale bars are 25 $\mu\text{m}$ .	93
Figure 5:1 Working principle of direct laser writing (DLW). (a) DLW based on a microscope objective. (b) DLW based on a multimode fiber. The fiber can enter and micro-fabricate inside areas difficult to access.	100
Figure 5:2 Two-photon polymerization with a 40x microscope objective (NA 0.65). (a) Calculated PSFs (one and two-photon). (b) DLW arrangement. (c) Linewidth dependence on writing speed. (d) Threshold power dependence on writing speed with and without the presence of oxygen.	102
Figure 5:3 Experimental setup. (a) Calibration. (b) Reconstruction for 3D printing.	103
Figure 5:4 Pulsed light transmission through the multimode fiber. (a) Speckle-like pattern produced on one end of the fiber when light is focused with a microscope objective on the other end. (b) Intensity autocorrelation of the speckle like pulse shown in (a). Pulse length is 210 fs. (c) Intensity pattern when light is focused through the fiber using spatial light modulation. (d) Second order interferometric autocorrelation of the spot shown in (c). Pulse length is 115 fs. (e) One-photon 2D PSF of the pulse delivered through the fiber (simulation). (f) Two-photon 2D PSF of the pulse delivered through the fiber (simulation).	105
Figure 5:5 Characterization of the 3D printing system. (a) Grid of voxels printed through the multimode fiber. (b) Grid of voxels printed through the multimode fiber in the case of exposure time correction. A radial correction of exposure is applied to polymerize voxels of uniform size. (c) Voxel diameter versus radial position for (a) and (b).	107
Figure 5:6 Voxel dependence on exposure time. (a-b) Example of voxels printed with 1.5, 1.1, 0.7, 0.3, 0.15, 0.1, 0.05, 0.03, 0.025, 0.0125 seconds of exposure. Scale bars are 7.5 $\mu\text{m}$ . (c) Voxel diameter dependence on exposure time. The logarithmic behavior arises due to an exponential decay of monomer concentration when the photoresists is exposed to light.	108
Figure 5:7 3D printed structures. (a) Helix. (b) Base of a scaffold structure. (c) Scaffold structure at a height of 40 micrometers.	109
Figure 5:8 Model of the Pyramid of Chichén Itzá 3D printed through a multimode optical fiber. The base diameter is as small as the thickness of a human hair. (a) Image of the pyramid acquired with a differential interference microscope. (b) Two-photon image of the pyramid acquired a 16 $\mu\text{m}$ height from the base. (c,d) Images of the pyramid acquired with a scanning electron microscope.	110
Figure 5:9 Picture of the lensed side of the multimode fiber 3D printing probe. The black case around the fiber and the grin lens holds the fiber and the lens and procures a mechanical stability when the lensed side is manually cleaned after each print. The fiber core and cladding are 400 and 560 micrometers diameter respectively. The fiber length is 5 cm.	111

# Chapter 1 Introduction

## 1.1 General introduction

An endoscope is a device that allows the visualization of the interior of orifices, canals, cavities or organs inside of the body. Endoscopes can be divided into two major groups: videoscopes and optical endoscopes. The videoscopes consist of optical and electronic elements that form an image of the scene of interest onto an imaging sensor, such as a CMOS or CCD chip, placed at the distal tip of the endoscope. The image is acquired and transmitted through wires to the proximal side (the “outside” side of the endoscope). On the other hand, optical endoscopes consist of a combination of optical components in a rigid or flexible configuration such as relay lenses, rod lenses, graded index probes or fiber bundles [1] as demonstrated by Hopkins in 1954 to directly relay an image from the distal scene to the proximal side. During the first half of the 20th century, endoscopes consisted of relay lenses with glass rods and large air lenses as shown in Figure 1:1 (a) [2]. But in 1959, Hopkins demonstrated a novel system composed of large glass rods placed between small air spaces that act as thin lenses. Such arrangement allows wider viewing angles and smaller diameters of the endoscope [2] and started being manufactured by Karl Storz after being improved with Hopkins [3].

Both videoscopes and optical endoscopes can be made or coated with materials that are not harmful for living beings. They are being widely used in research and medicine. However, as will be explained next, optical endoscopes are the type that can reach the smallest diameters, enabling ultra-thin minimally invasive probes, which are required for some specific applications.

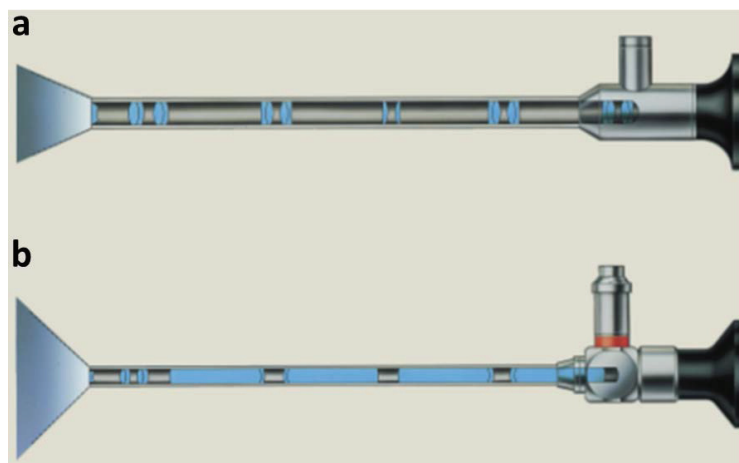


Figure 1:1 Lens systems for optical endoscopes. (a) Conventional system with glass lenses invented by Nitze in 1877. (b) Hopkins rod-lens system [2].

In practical terms, the selection of an endoscope is application dependent. In videoscopes, the diameter of the probe is limited to the size of the image sensor. In applications where the orifices diameter range in the tens of millimeters and where the application is tissue imaging over a field of view in the centimeter range, videoscopes or Storz-Hopkins rod lens systems can be employed. However, for imaging at a cellular level through small orifices, a higher resolution imaging system is required and is usually achieved by fiber optic endoscopes shown in Figure 1:2.

Fiber optic endoscopes not only can transmit images with a white light illumination, but also allow fluorescent imaging in one and two-photon fluorescent modality [4]. The principle of fluorescent imaging through a light guiding probe is very simple: a focused illumination is scanned over the sample while the fluorescent signal is collected through the same probe, allowing the acquisition of an image point by point. This can be achieved through long graded index lenses, double clad fibers [5], multi-core fibers and, as demonstrated very recently [6], through multimode optical fibers.

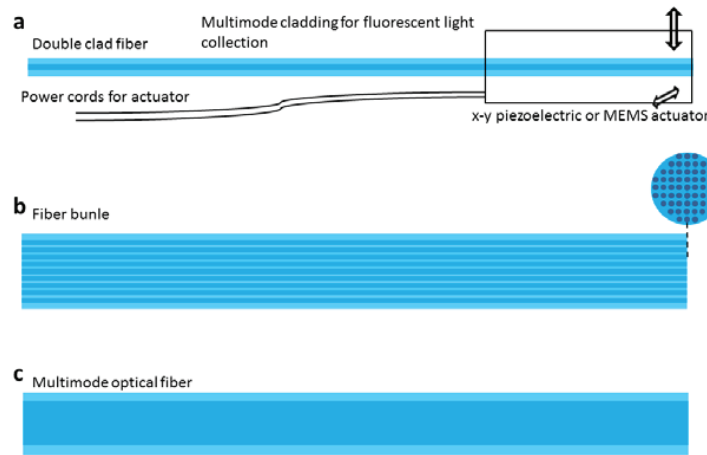


Figure 1:2 Optical fiber endoscopes. (a) Double clad fiber system. Mechanical elements are required to scan the illumination on the sample. (b) Fiber bundle system. Each core relays a "pixel" of the distal scene. (c) Multimode fiber system. Using wavefront shaping, light point scanning on the specimen followed by the collection of the fluorescent signal allows fluorescent imaging.

The present work aims at demonstrating an ultra-thin minimally invasive multimode fiber endoscope capable of acquiring high resolution images with optical sectioning, which is achieved by the introduction of a multi-photon imaging modality through multimode optical fibers. This approach provides all the advantages of multi-photon microscopy at the tip of a needle, such as a reduced photo bleaching of the sample, optical sectioning and enhanced image contrast. To achieve this goal, a method to focus and scan optical pulses through multimode fibers is developed. The developed method is inspired by previous work on light control through multimode fibers and scattering media demonstrated for the continuous wave case.

In addition to the work in multimode fiber imaging, we realized that the same core technology used to scan optical pulses with capability of producing nonlinear phenomena at the tip of a multimode fiber can also be used to trigger two-photon polymerization. As its name suggests, in two photon polymerization, a high energy pulse produces the polymerization of a liquid



photoresist, which is followed by a removal of the non-exposed photoresist or “development”. The whole process allows additive manufacturing also known as 3D printing.

3D printing comprises different manufacturing methods applicable to the fabrication of three-dimensional objects starting from a computer aided designed (CAD) model. The generated objects can be built with macroscopic and microscopic dimensions with different resolutions depending on the application and the specific method employed.

Among the 3D printing techniques there is a subset known as direct laser writing methods, in which lasers can produce various chemical and physical processes on almost any material [7], allowing the fabrication of high-resolution micro-structures. Two-photon polymerization lies in this category. At a glance, a nonlinear multiphoton absorption process is produced by high power laser focused beams impinging on a photo-sensitive material that polymerizes at spatially confined volume. Scanning of the focused beam with respect to the material hardens the polymer enabling the creation of three-dimensional objects. The resolutions that can be achieved with two-photon polymerization are of the order of the excitation wavelength [8, 9].

To achieve the high intensities required for this nonlinear material processing usually high peak power laser beams are focused on the material using high numerical aperture microscope objectives. These optical elements have to be in close proximity to the material that they polymerize (from hundreds of micrometers to several mm). This technological constrain prevents the use of additive manufacturing through small apertures or in places of difficult access. Using the wavefront shaping methods to focus optical pulses through multimode fibers developed in this thesis, those limitations are disrupted. Specifically, the present work aims at developing 3D printing through a multimode fiber based on two-photon polymerization, overcoming completely those limitations allowing additive manufacturing in places of difficult access. We call it endofabrication. As in endoscopy, endofabrication enables the remote fabrication of micro structures and could eventually allow a whole new set of applications such as in situ tissue regeneration, creation of scaffolds for cellular growth, or simply high resolution manufacturing directly inside of living animals or places of difficult access, which were unthinkable with previous technologies.

## 1.2 Thesis objectives

This thesis deals with the application of light control methods in the field of fiber endoscopy and 3D printing. In specific, the objectives of this thesis are the following:

- Study and development of wavefront shaping methods that not only produce a pre-defined spatial intensity profile on the other side of a multimode optical fiber, but also transmit an ultrashort pulse with a pulse length in the order of hundreds of femtoseconds.
- Design, development and demonstration of a minimally-invasive multi-photon endoscope that, based on the methods mentioned above, can acquire high resolution images at different planes deep inside biological tissue, allowing the visualization of cells.

- Design and development of an ultra-thin 3D printer based on two-photon polymerization. The working principle relies on the methods to focus optical pulses mentioned above.

### 1.3 Thesis outline

Chapter 1 presents a general introduction about optical fiber endoscopes, what type of fiber endoscopes exist as well as the advantages and disadvantages of each one of them. Also presents a recent paradigm in endoscopy based on multimode fibers. An overview about 3D printing and how a multimode optical fiber can be used as an ultra-thin 3D printer is also shown.

Chapter 2 presents an overview about light propagation in free space and scattering media. The similarities between light propagation in scattering media and multimode fiber are also discussed. Propagation of optical pulses in multimode fibers is presented. Digital holography applied to optical phase conjugation and the transmission matrix measurement are introduced and demonstrated experimentally for light focusing through multimode optical fibers in the continuous wave case. Limitations and possible applications of these methods are also mentioned.

An extension of the wavefront shaping methods for light focusing through opaque media named as time-gated digital phase conjugation is presented in chapter 3. This is a method to transmit and focus optical pulses through multimode optical fibers. The intrinsic counter-propagation of modes of similar velocity among them allows a reduction in the temporal broadening produced by modal dispersion. Experimental demonstration of delivery of focused ultrashort pulses is presented. Generation of nonlinear phenomena on the other end of the multimode fiber is also demonstrated.

The application of the developed methods based on digital holography and wavefront shaping in the field of multimode fiber endoscopy are presented in chapter 4. In this chapter, a multimode fiber two-photon endoscope is demonstrated. This endoscope allows the acquisition of high resolution images at different depths inside biological tissue. Characterization of the performance of the endoscope in terms of lateral and axial resolution, pulse length of the scanned focused pulses and imaging field of view are also mentioned.

In chapter 5 the methods introduced and demonstrated in chapter 2 are applied to a completely different field: 3D printing. In this chapter, three-dimensional fabrication of microstructures is demonstrated through an ultra-thin needle as thick as three human hairs. The presented work enables a new sub-area in the field of 3D printing that allows the fabrication of 3D structures and objects inside small apertures or within cavities inside a body. We call it **endofabrication**.

Chapter 6 concludes the thesis presenting a discussion and a general conclusion of the results achieved in this thesis. Future improvements and future work foreseen in the field is also discussed.

## 1.4 List of published articles

The work presented in this thesis has resulted in the publication of 9 conference papers and 3 peer review papers enlisted in detail below:

### 1.4.1 Presentations in international conferences

#### **OSA Frontiers in optics 2014**

E. Morales, S. Farahi, I. Papadopoulos, D. Psaltis, and C. Moser, "Focusing of an ultrashort pulse through a multimode fiber using Digital Phase Conjugation," in *Frontiers in Optics 2014*, OSA Technical Digest (online) (Optical Society of America, 2014), paper FTh1G.7, Tucson AZ, October 19–23, 2014.

<https://www.osapublishing.org/abstract.cfm?uri=fio-2014-FTh1G.7>

#### **SPIE Photonics west 2015**

Edgar E. Morales Delgado ; Ioannis N. Papadopoulos ; Salma Farahi ; Demetri Psaltis ; Christophe Moser; Delivery of an ultrashort spatially focused pulse to the other end of a multimode fiber using digital phase conjugation. Proc. SPIE 9335, Adaptive Optics and Wavefront Control for Biological Systems, 93350J (March 10, 2015); doi:10.1117/12.2078023, San Francisco CA, February 7-12, 2015.

<http://proceedings.spiedigitallibrary.org/proceeding.aspx?articleid=2203192>

#### **SPIE Biophotonics South America 2015**

E. Morales, S. Farahi, I. Papadopoulos, D. Psaltis, and C. Moser, "Delivery of ultrashort spatially focused pulses through a multimode fiber for two photon endoscopic imaging," in *Biophotonics South America 2015*, SPIE, Rio de Janeiro, Brazil, May 23-25, 2015.

<http://proceedings.spiedigitallibrary.org/proceeding.aspx?articleid=2330665>

#### **Photorefractive Villars 2015**

E. Morales, S. Farahi, I. Papadopoulos, D. Psaltis, and C. Moser, "Focusing pulsed light through a multimode fiber," in *Photorefractive Photonics 2015*. Villars, Switzerland, June 16-19, 2015.

#### **CLEO Munich 2015**

E. Morales, S. Farahi, I. Papadopoulos, D. Psaltis, and C. Moser, "Towards a multimode fiber two-photon endoscope," in *CLEO 2015*, OSA, Munich Germany, June 21-25, 2015.

[https://www.osapublishing.org/abstract.cfm?uri=cleo\\_europe-2015-CL\\_5\\_5](https://www.osapublishing.org/abstract.cfm?uri=cleo_europe-2015-CL_5_5)

#### **Adaptive Optics and Wavefront Control in Microscopy and Ophthalmology 2015**

E. Morales, S. Farahi, I. Papadopoulos, D. Psaltis, and C. Moser, "Towards a multimode fiber two-photon endoscope", Paris France, 5-7 October 2015.

### SPIE Biophotonics Japan 2015

E. Morales, S. Farahi, I. Papadopoulos, D. Psaltis, and C. Moser, "Time-gated digital phase conjugation for two-photon excitation microscopy through multimode optical fibers", Tokyo Japan, 27-28 October 2015.

<http://proceedings.spiedigitallibrary.org/proceeding.aspx?articleid=2475809>

### SPIE Photonics West 2016

E. Morales, D. Psaltis, and C. Moser, "Two-photon excitation endoscopy through a multimode optical fiber", San Francisco CA, February 13-18, 2016.

<http://proceedings.spiedigitallibrary.org/proceeding.aspx?articleid=2504640>

### OSA Australian Conference on Optical Fibre Technology (ACOFT)

E. Morales, D. Psaltis, and C. Moser, "Focusing and scanning of femtosecond pulses through a multimode fiber: applications in two-photon imaging and polymerization", Sidney Australia, September 5-8, 2016.

#### 1.4.2 Peer reviewed publications

Morales-Delgado E. E., Psaltis D., Moser C., *Two-photon imaging through a multimode fiber*, Optics Express, Vol. 23, Issue 25, pp. 32158-32170, 2015.

Morales-Delgado E. E., Farahi S., Papadopoulos N. I., Psaltis D., Moser C., *Delivery of focused short pulses through a multimode fiber*, Optics Express, Vol. 23, Issue 7, pp. 9109-9120, 2015.

Conkey D., Stasio N., Morales-Delgado E., Romito M., Moser C., Psaltis D. *Lensless two-photon imaging through a multi-core fiber with coherence-gated digital phase conjugation*, (in peer-review process).

Morales-Delgado E. E., Conkey D., Stasio N., Psaltis D., Moser C., ***"Three-dimensional micro-fabrication through a multimode optical fiber"***. This article is currently under peer-reviewed process.

## 1.5 References

1. H. H. Hopkins and N. S. Kapany, "A Flexible Fibrescope, Using Static Scanning," *Nature* **173**, 39-41 (1954).
2. A. Di Ieva, M. Tam, M. Tschabitscher, and M. D. Cusimano, "A Journey into the Technical Evolution of Neuroendoscopy," *World Neurosurg* **82**(2014).
3. G. Zada, C. Liu, and M. L. J. Apuzzo, ""Through the Looking Glass": Optical Physics, Issues, and the Evolution of Neuroendoscopy," *World Neurosurg* **79**, S3-S13 (2013).
4. B. A. Flusberg, E. D. Cocker, W. Piyawattanametha, J. C. Jung, E. L. M. Cheung, and M. J. Schnitzer, "Fiber-optic fluorescence imaging," *Nat Methods* **2**, 941-950 (2005).
5. M. T. Myaing, D. J. MacDonald, and X. D. Li, "Fiber-optic scanning two-photon fluorescence endoscope," *Opt Lett* **31**, 1076-1078 (2006).

6. I. N. Papadopoulos, S. Farahi, C. Moser, and D. Psaltis, "High-resolution, lensless endoscope based on digital scanning through a multimode optical fiber," *Biomed Opt Express* **4**, 260-270 (2013).
7. I. Gibson, D. Rosen, and B. Stucker, *Additive Manufacturing Technologies* (Springer-Verlag New York 2015).
8. T. Baldacchini, *Three-Dimensional Microfabrication Using Two-Photon Polymerization, Fundamentals, Technology, and Applications* (Elsevier 2016).
9. S. Maruo, O. Nakamura, and S. Kawata, "Three-dimensional microfabrication with two-photon-absorbed photopolymerization," *Opt Lett* **22**, 132-134 (1997).



# Chapter 2 Control of pulsed light propagation in multimode fibers

## 2.1 Light propagation in free space and scattering media

Light propagates through a uniform medium in a straight line. In the presence of inhomogeneities or refractive index variations of size comparable to the wavelength, light waves are deviated from their original direction at every wave-scatterer interaction. This phenomenon is known as multiple scattering and can be commonly seen in opaque media such as white paint, milk, fog, clouds or biological tissues.

Multiple scattering represents an obstacle for optical imaging through disordered media, because it randomizes the polarization, phase and amplitude of the incident field producing a speckle pattern on the other side of the medium [1].

Non uniform intensity distributions and the generation of a speckle like pattern not only occur when light is transmitted through scattering media, but also when light propagates through a multimode waveguide. In optical fibers, light propagates as a finite number of modes which are solutions to the wave equation in the fiber that satisfy its boundary conditions. Those modes include traveling modes that propagate longitudinally in the fiber. In a single mode fiber only a single mode is a propagating solution and is well defined by a single spatial profile along the fiber. In multimode fibers there are more than one traveling wave solutions that allow the transport of energy from one end of the fiber to the other. The interaction between various modes in terms of phase and mode coupling and also the coherent interference between them changes the intensity and phase profile of the field, leading to the formation of an intensity profile similar to a speckle like pattern on the other end of the fiber [2-7].

Although such intensity distributions look random, their origin is linear and deterministic. Therefore, it is a time-reversible phenomenon. This implies that it is possible to alter the field so that the effect of the scattering medium can be compensated. For instance, that scrambling effect can be corrected by the use of so called wavefront correction techniques, which consist, in a first step, of measuring the scrambled field at the output of a scattering medium or a multimode fiber and then, in a second step, providing an appropriate input wavefront which, in essence pre-compensates the distortion caused the scattering medium. By phase or amplitude modulation of the incident beam obtained for example via a heuristic measurement, such as the optimization of an intensity signal, focusing and generation of light patterns through the turbid media become possible. Another approach is the linear transformation characterization of the medium or by means of a counter-propagation process such as digital phase conjugation. These methods will be explained in more detail in this chapter.

One of the first attempts to control light through scattering media was demonstrated using iterative methods. Based on iterative algorithms the phase or intensity of a light beam incident on a scattering media is spatially shaped and the field at the output is measured [8-10]. By providing feedback to the spatial light modulator (SLM), input phase is changed until scrambling vanishes and the desired field distribution is obtained.

An alternative technique consists of characterizing the linear input-output complex field response of a disordered medium or an optical waveguide by measuring its optical transmission matrix [11-13]. This is illustrated in Figure 2:10. By knowing the transmission matrix, it is possible to recreate any desired intensity profile by spatially modulating a light beam with the correct phase or amplitude that pre-compensates for the scrambling effects of light propagation in the medium. The ability to generate any arbitrary intensity pattern makes of the transmission matrix a more powerful light focusing tool.

The last method that can be used to focus light in turbid media is digital phase conjugation. It directly exploits the time-reversibility nature of the multiple scattering processes or of the linear light transmission in multimode fibers. It consists of two steps. In the first step, an intensity distribution is projected on one side of a disordered media emerging on the other side as a speckle like pattern. Then, using a phase conjugate mirror, as illustrated in Figure 2:1 (b) light is not reflected, but instead re-traces back exactly as it came, traveling in reverse as it did before converging at the location of the initially projected intensity pattern. The phase conjugate mirror, in the monochromatic case, can be implemented with a combination of a camera and a SLM as will be explained in this chapter.

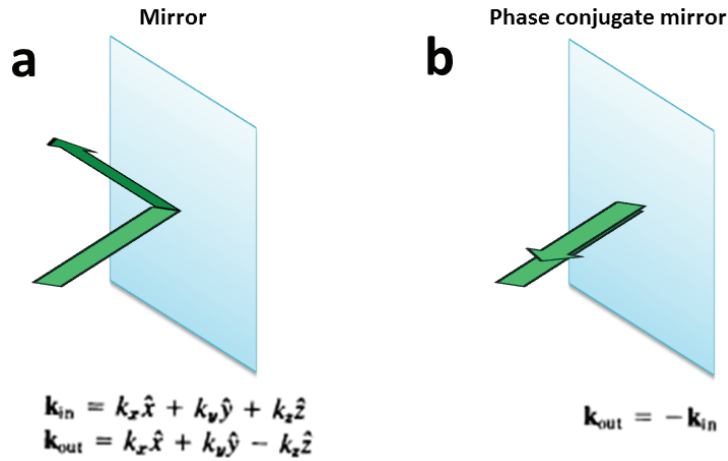


Figure 2:1 Representation of a phase-conjugate mirror. (a) Normal mirror. (b) Phase conjugate mirror.

Digital phase conjugation and the transmission matrix method have been used to acquire images through multimode fibers. A way to achieve this is by first scanning a diffraction limited spot over the whole facet of a fiber and then collecting, through the same fiber, the light scattered or fluorescently emitted by the sample [12-19]. Scanning is achieved without moving the fiber with respect to the sample. With wavefront shaping methods, a lensless endoscope capable of scanning without movable components can be conceived as will be demonstrated in chapter 3.



This chapter presents theoretical and experimental verification of pulsed light propagation in multimode optical fibers. Additionally, the transmission matrix method and digital phase conjugation for the control of pulsed light are introduced.

## 2.2 Propagation of ultrafast pulses in MMFs

### 2.2.1 Characteristics of optical pulses

Ultrashort optical pulses are periodic bursts of energy with very high peak powers followed by long periods of zero amplitude. An optical pulse is considered as an ultrashort pulse if its full width at half maximum (FWHM) pulse duration is smaller than a picosecond. Such optical pulses possess a broad spectrum and are commonly generated by mode locked oscillators. To generate ultrashort optical pulses, various modes, each one centered at a specific wavelength in a laser cavity, are amplified. The wavelength spacing between modes is constant. When the modes are all in phase (mode locked) a high peak power pulse is generated [20, 21]. A frequency comb can be represented as a linear combination of equally frequency spaced monochromatic waves whose electric field, assuming a linear polarization, is given by:

$$E(t) = \sum_{n=-N/2}^{N/2-1} E_n e^{i[(\omega_0+n\Delta\omega)t+\varphi_n]}$$

Equation 2:1 – Frequency comb.

Where  $N$  is the number of discrete spectral components or modes that conform the optical pulse,  $\omega_0$  is the central angular frequency,  $\Delta\omega$  is the angular frequency spacing between modes and  $\varphi_n$  is the modal phase. Representation of a single pulse in the temporal domain can be given by a Gaussian envelope modulating an optical carrier:

$$E(t) = e^{-(t-t_0)^2/(2\sigma^2)} \cos(2\pi\omega_0 t)$$

Equation 2:2 – Gaussian optical pulse.

Where  $\sigma$  is the standard deviation of the Gaussian envelope and is related to the FWHM pulse length  $\tau_p$  as:  $\sigma = \tau_p / (2\sqrt{2\ln(2)})$ .

As will be described in this chapter, optical pulses can suffer spectral and temporal distortions when propagating through different types of media affecting their peak power and thus their ability to generate nonlinear phenomena, which is necessary for some applications. An optical pulse at its shortest temporal duration is known as a transform-limited pulse, and its minimum pulse length is given by its spectral width. An example of a transform-limited pulse is shown in Figure 2:2.

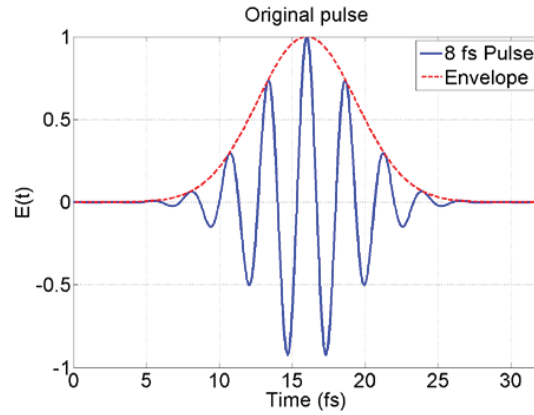


Figure 2:2 A transform-limited Gaussian pulse of 8 fs pulse length at a central wavelength of 800 nm.

The quantities that fully characterize an optical pulse are the repetition rate  $t_R$ , which sets the temporal spacing between the pulses and is given by the frequency spacing of the contiguous monochromatic components of the frequency comb; the pulse length  $\tau_p$ , which in a transform-limited pulse is given by the spectral width of the frequency components; the pulse shape, which is the shape of the pulse envelope and is commonly of the  $\text{sech}^2$  type; and the pulse energy  $E_p$ . Knowing all those quantities, additional values of interest such as the peak power, average power and pulse length of a “chirped” pulse can be derived. A chirped pulse is a pulse whose frequency changes over time. This can be produced when light travels through dispersive media as will be explained in the next section. This phenomenon is known as group velocity dispersion (GVD) or material dispersion.

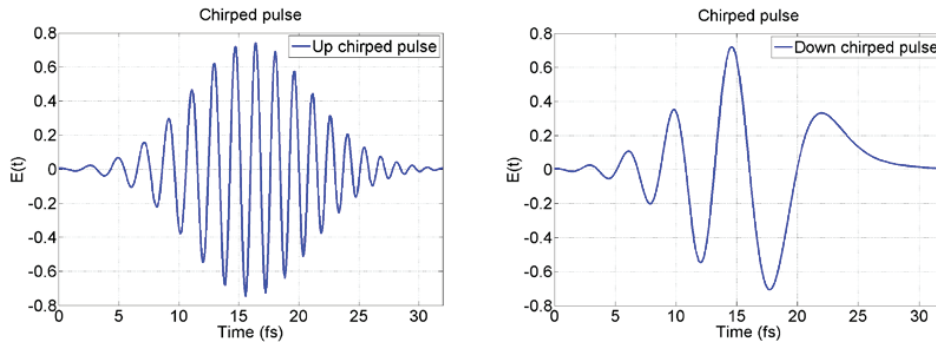


Figure 2:3 Linearly chirped optical pulses. (a) An 8 fs optical pulse after propagation in 0.7 mm of Silica at a central wavelength of 800 nm. (b) Same as a, but after propagation through a material with the opposite sign of dispersion.

### 2.2.2 Ray trace approach of light propagation in MMFs

The light guiding principle of optical waveguides is based on the phenomenon of total internal reflection. A multimode optical fiber is composed a cylindrical core surrounded by a cladding made of a material of a lower refractive index than that of the core. In step-index fibers the core-cladding interface possesses an abrupt change in refractive index as illustrated in Figure 1:1. In graded-index optical fibers the change of refractive index is gradual.

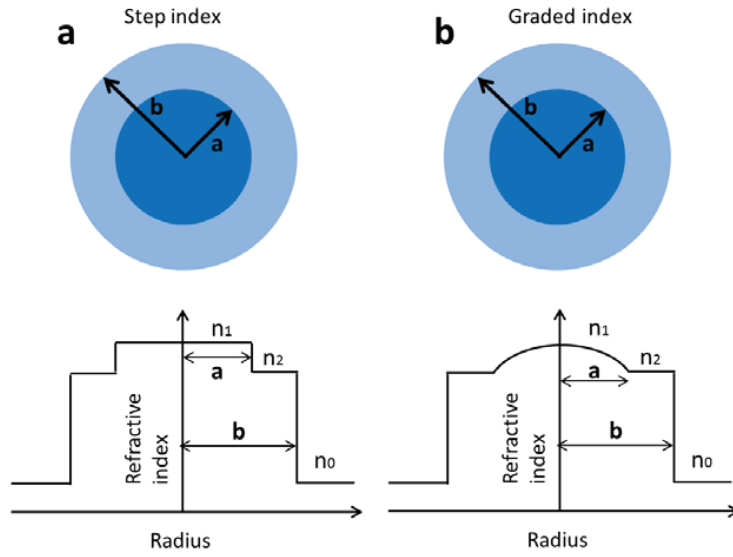


Figure 2:4 (a) Step index fiber. (b) Graded index fiber.

The first approximation to light propagation in an optical fiber is given by a light ray approach, which is valid when the core diameter is much larger than the wavelength  $\lambda$  [22]. At one end of the fiber, due to refraction at the fiber-air interface, only light rays incident within a certain angular range or cone can bounce and be guided into the fiber. Considering Snell's law, light entering the fiber at an angle  $\theta_i$  with respect to the optical axis are refracted to the core at an angle  $\theta_r$ :

$$n_0 \sin \theta_i = n_1 \sin \theta_r$$

Equation 2:3 – Snell's law at the air-core interface of an optical fiber.

Where  $n_0$  and  $n_1$  are the refractive indices of the medium surrounding the fiber and the core of the fiber, respectively. At the air-core interface light rays are refracted as illustrated in Figure 2:5. At the core cladding interface, light rays can be refracted or totally reflected. The condition for total internal reflection corresponds to a critical angle  $\theta_c$ :

$$n_1 \sin \theta_c = n_2$$

$$\sin \theta_c = n_2 / n_1$$

Equation 2:4 – Critical angle.

Where  $n_2$  is the refractive index of the cladding. All internal rays with angles larger than  $\theta_c$  propagate within the fiber core.

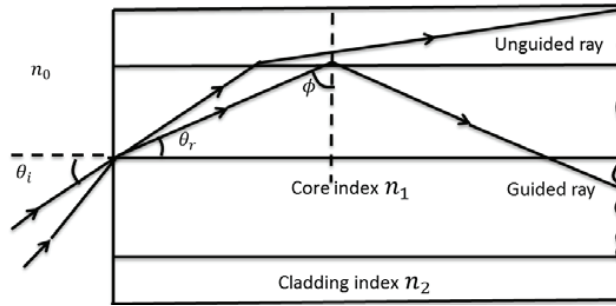


Figure 2:5 Ray tracing in a step index optical fiber.

Combining the equation of total internal reflection and refraction at the air-core interface, the following relation can be derived:

$$n_0 \sin \theta_i = n_1 \cos \phi_c = (n_1^2 - n_2^2)^{1/2}$$

Equation 2:5 – Numerical aperture in an optical fiber.

This quantity is known as the numerical aperture (NA) of the fiber and is related to the maximum incident angle in which the fiber can guide light:

$$\theta_{i\_max} = \text{asin}\left(\frac{NA}{n_0}\right)$$

Equation 2:6 – Acceptance angle in an optical fiber.

For fibers with similar core and cladding refractive indices, the numerical aperture can be approximated as:

$$NA \approx n_1 \sqrt{2\Delta}$$

Equation 2:7 – Approximation to the numerical aperture in an optical fiber.

Where  $\Delta = (n_1 - n_2)/n_1$ .

For a graded index fiber, the core refractive index decreases gradually towards the cladding, following the radial profile:

$$n(\rho) = \begin{cases} n_1 [1 - \Delta(\rho/a)^\alpha]; & \rho < a, \\ n_1 (1 - \Delta) = n_2; & \rho \geq a \end{cases}$$

Equation 2:8 – Radial dependence of the refractive index in a graded index optical fiber.

Where  $\rho$  is the radial position from the ray to the axis,  $a$  is the fiber core diameter and  $\alpha$  represents the index profile which is usually parabolic ( $\alpha = 2$ ).

The graded index profile dramatically reduces the multi-path dispersion because, as illustrated in Figure 2:6, oblique incident rays propagate in longer paths but in a faster medium (smaller refractive index) than straight rays that travels the shortest distance but in a slower path.

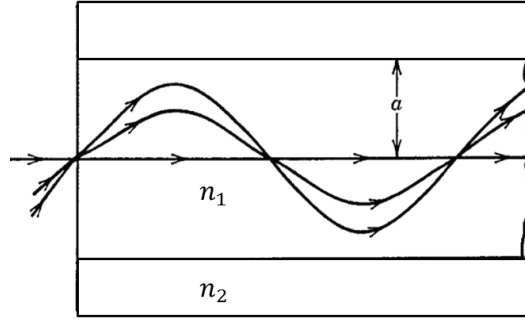


Figure 2:6 Ray tracing in a graded index optical fiber.

### 2.2.3 Electromagnetic wave approach for light propagation in MMFs

The phenomenon of light propagation in multimode optical fibers is governed by the wave equation, which can be derived from Maxwell's equations presented below in their differential form:

$$\nabla \cdot D = \rho_m$$

Equation 2:9 – Gauss' law for electric fields.

$$\nabla \cdot B = 0$$

Equation 2:10 – Gauss' law for magnetic fields.

$$\nabla \times E = -\frac{\partial B}{\partial t}$$

Equation 2:11 – Faraday's law.

$$\nabla \times H = \sigma E + \frac{\partial D}{\partial t}$$

Equation 2:12 – Ampere's law.

Where  $D = \epsilon E$  is the electric flux density,  $B = \mu H$  is the magnetic flux density,  $E$  is the electric field,  $H$  the magnetic field,  $\epsilon$  is the electric permittivity of the medium and  $\mu$  the magnetic permittivity.

Since optical fibers are passive elements and have low attenuation, we can assume a sourceless and lossless medium. Taking the curl of Equation 2:11, substituting Equation 2:12 in Equation 2:11, and using the vector identity  $\nabla \times \nabla \times E = \nabla(\nabla \cdot E) - \nabla^2 E$ , the fiber wave equation can be obtained:

$$\nabla^2 E + \mu\epsilon \frac{\partial^2 E}{\partial t^2} = 0$$

Equation 2:13 – Wave equation.

Rewriting Equation 2:13 in cylindrical coordinates, and solving it using the method of separation of variables enforcing the boundary conditions that the optical field is finite at the optical axis and decays to zeros at an infinite radius, the general solution for the electric field is:

$$E_z = \begin{cases} AJ_m(p\rho) \exp(im\phi) \exp(i\beta z); & \rho \leq a, \\ CK_m(q\rho) \exp(im\phi) \exp(i\beta z); & \rho > a. \end{cases}$$

Equation 2:14 – Longitudinal electric field.

And for the magnetic field is:

$$H_z = \begin{cases} BJ_m(p\rho) \exp(im\phi) \exp(i\beta z); & \rho \leq a, \\ DK_m(q\rho) \exp(im\phi) \exp(i\beta z); & \rho > a. \end{cases}$$

Equation 2:15 – Longitudinal magnetic field.

Where  $J_m$ ,  $Y$ ,  $K_m$ , and  $I_m$ , are Bessel functions and  $A$ ,  $C$ ,  $B$  and  $D$  are constants obtained when enforcing a continuity boundary condition between the core and the cladding. The other components of the electric and magnetic field can be obtained from the longitudinal ones using Maxwell's equations.

Since the difference in refractive index between the fiber core and cladding is usually very small, a weakly guiding approximation can be used, in which several modes are degenerative, which means they have the same propagation constant [20]. The solution then gets simplified as a set of linearly polarized LP modes dependent on the  $l, m$  indices, which are related to the radial and azimuthal variations in the intensity of the electric field. Example of the intensity of some fiber modes is shown in Figure 2:7 Intensity profile of some  $LP_{l,m}$  modes..

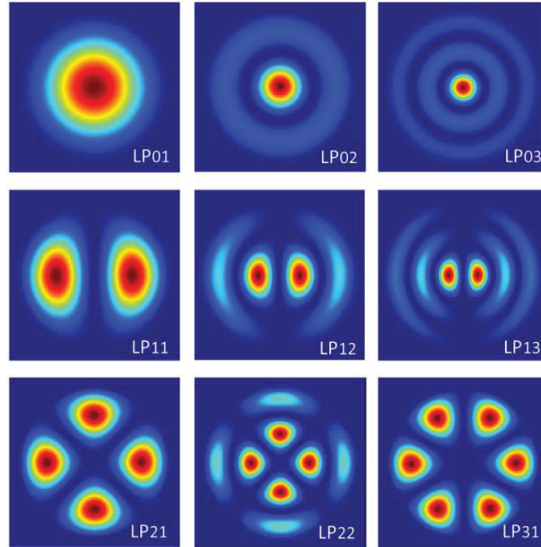


Figure 2:7 Intensity profile of some  $LP_{l,m}$  modes.

The fiber modes are traveling wave solutions to the fiber wave equation and represent the transport of energy or information from one end of the fiber to the other.

An important parameter that determines the number of modes that can propagate in a multimode fiber is the normalized frequency, also known as V parameter, which is given by:

$$V = 2\pi \frac{a}{\lambda_0} NA$$

Equation 2:16 – Normalized frequency.

Where  $\lambda_0$  is the central wavelength of the excitation.

In a fiber with a large V parameter, the number of modes can be approximated as [20]:

$$M = \frac{4}{\pi^2} V^2$$

Equation 2:17 – Number of modes in a multimode fiber.

When light is coupled into a multimode fiber with a very large number of supported fiber modes  $M$ , the intensity of the transmitted optical field instead of taking a well-defined modal shape that resembles to any of the mode intensities shown in Figure 2:7, they produce a speckle like pattern due to the interference of modes with different phases and propagation constants. This is shown in Figure 2:8 where light is focused with a 40X microscope objective into a 50 mm long graded index multimode optical fiber of 600  $\mu\text{m}$  core diameter and the intensity is measured on the other side.

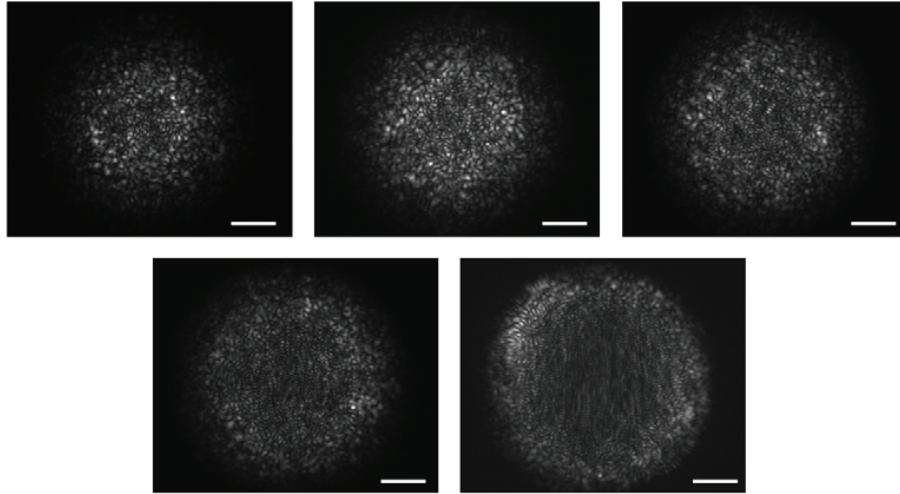


Figure 2:8 intensity scrambling in MMFs. Light is focused with a 40X microscope objective on one end producing the shown scrambled intensities. The fiber is 200  $\mu\text{m}$  fiber in core diameter. From top left to lower right the excitation is scanned in a 20  $\mu\text{m}$  step along the cross section at the optical axis of the fiber, starting 10  $\mu\text{m}$  off centered. Scale bar is 40  $\mu\text{m}$ .

In addition to the spatial distortions occurring in an optical fiber, material and modal dispersion introduce temporal alterations in the propagating pulse.

#### 2.2.4 Material dispersion

Let us consider a single mode propagation in a multimode optical fiber. The velocity of a specific spectral component, known as group velocity, is given by [20].

$$v_g = (d\beta/d\omega)^{-1}$$

Equation 2:18 – Group velocity.

Where  $\beta$  is the propagation constant.

The dependence of the group velocity on optical frequency results in a temporally broadened optical pulse because different spectral components arrive at different times on the other end of the fiber. This is known as material dispersion or group velocity dispersion (GVD.) For example, the 8 fs transform-limited optical pulse shown in Figure 2:2, upon propagation in 0.7 mm of fused silica, leads to the dispersed pulse shown in Figure 2:3 (a). This is known as up-chirping and can be seen as an increased frequency of the cosine carrier of the optical pulse as time increases. Figure 2:3 (b) shows the same optical pulse but traversing a media with the opposite same value of dispersion coefficient. This is called a down-chirped pulse, whose frequency decreases over time.

GVD constitute a limitation for the transmission of transform-limited pulses through a multi-mode fiber causing and undesired decrease in the peak power of the transmitted pulse, restricting the generation of nonlinear phenomena at the tip of the fiber. GVD can be compensated by adding a group delay using a prism pair or a grating pair, as will be described in the practical scenarios of chapter 3 and 4.

The temporal broadening produced by material dispersion is given by:

$$\sigma_{mat} \approx D_\lambda \Delta\lambda L$$

Equation 2:19 – Material dispersion in an optical fiber.

Where  $D_\lambda$  is the dispersion coefficient,  $\Delta\lambda$  is the source spectral width and L the length of the fiber.

### 2.2.5 Modal dispersion

Another phenomenon that alters the ultrashort temporal profile of an optical pulse is known as modal dispersion. As its name suggests, it is produced by the fact that different fiber modes travel at different group velocities. The group velocity of the modes of a step index fiber is given by:

$$v_{l,m} \approx c_1 \left[ 1 + \frac{(l+2m)^2}{M} \Delta \right]^{-1}$$

Equation 2:20 – Group velocity of the l,m mode.

Where  $M$  is the number of modes supported by the fiber,  $l = 0, 1, \dots, \sqrt{M}$ ,  $m = 1, 2, \dots, 0.5(\sqrt{M} - l)$  and  $\Delta$  is the fractional difference in refractive index between the core and cladding. The indices  $l$  and  $M$  are the azimuthal and radial indices that characterize the intensity distribution of any fiber mode [20].



Considering a single polarization and only positive  $l$  values, the group velocity of the modes of a 200  $\mu\text{m}$  multimode optical fiber at a 1550 nm excitation is represented graphically in Figure 2:9:

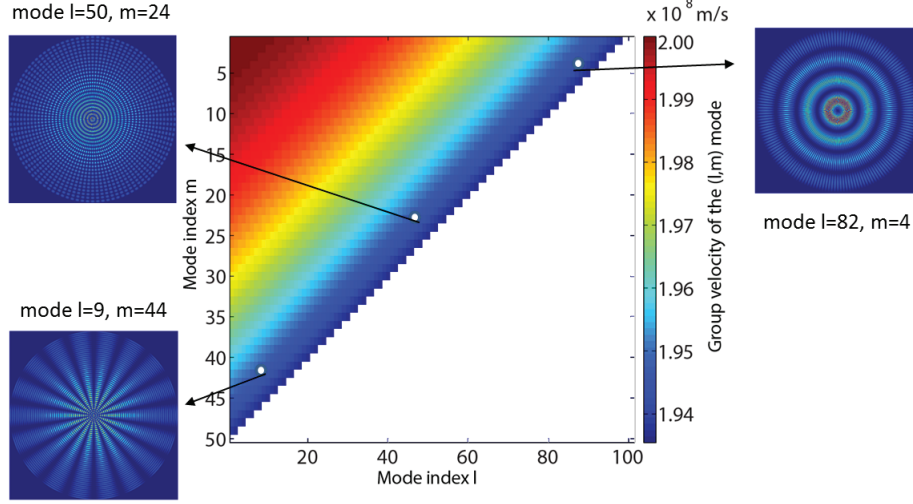


Figure 2:9 Plot of the mode velocity as a function of the  $l$  and  $M$  indices. There are group of modes that travel at the same speed. The control of such mods can lead to interference phenomena such as light focusing and projection of patterns.

In step index fibers, the temporal broadening produced by modal dispersion is given by:

$$\sigma_{\text{modal}} \approx \frac{L}{2c_0} n_1 \Delta$$

Equation 2:21 – Temporal broadening due to modal dispersion in step index multimode fibers.

While in graded index fibers, the temporal broadening is reduced due to the parabolic index profile:

$$\sigma_{\text{modal}} \approx \frac{L}{4c_0} n_1 \Delta^2$$

Equation 2:22 – Temporal broadening due to modal dispersion in graded index multimode fibers.

Interference phenomena can only occur when the temporal separation of the fiber modes lies within the coherence length of each individual mode, given by the source bandwidth. Therefore, for control of light propagation in multimode fibers, a graded index fiber results in better light focusing capabilities due to its reduced modal dispersion.

### 2.3 Focusing light using the transmission matrix

In this section the measurement of a transmission matrix of a multimode optical fiber at a fixed bending state is explained. The measurement of the transmission matrix is nothing more than a characterization of a scattering or opaque media achieved by measuring the input-output response of the medium, which can be, for example, a scattering medium or a multimode fiber. Specifically, a set of known inputs, intensities or phase modulations at the input

are launched into the medium and, at the output, the complex field is measured. This allows the construction of a matrix that, in the most complete implementations, relates complex fields at the input to complex fields at the output as illustrated in Figure 2:10.

There are many choices of basis functions for the measurement of a transmission matrix. The basis functions are usually modulated using a phase spatial light modulator or an amplitude modulator in the macropixel configuration to generate phase modulation based on, for example, Lee holography [23]. The selected set of basis functions can be a pixel-based basis, in which each function is a single pixel or macropixel with a modulated phase. Another example is the use of mathematically orthogonal functions, like the hadamard basis which will be explained in more detail, where each element of the basis is converted into a spatial representation of phases modulated at the input of the medium. It can also be a set of plane waves propagating each one in a unique direction within the acceptance angle of the fiber. Another alternative would be to calculate the propagating modes of the specific fiber whose transmission matrix has to be measured and use a modal basis function, in which each one of the basis functions is a propagating mode. In practical terms, this measurement is not straightforward with the strictly correct modal basis. To excite an specific theoretically calculated mode in an optical fiber with a very large number of nodes, amplitude, phase and polarization modulation would be required, which is not always straightforward to implement. Therefore, in such approaches, often the phase only modulation of the modes is usually employed.

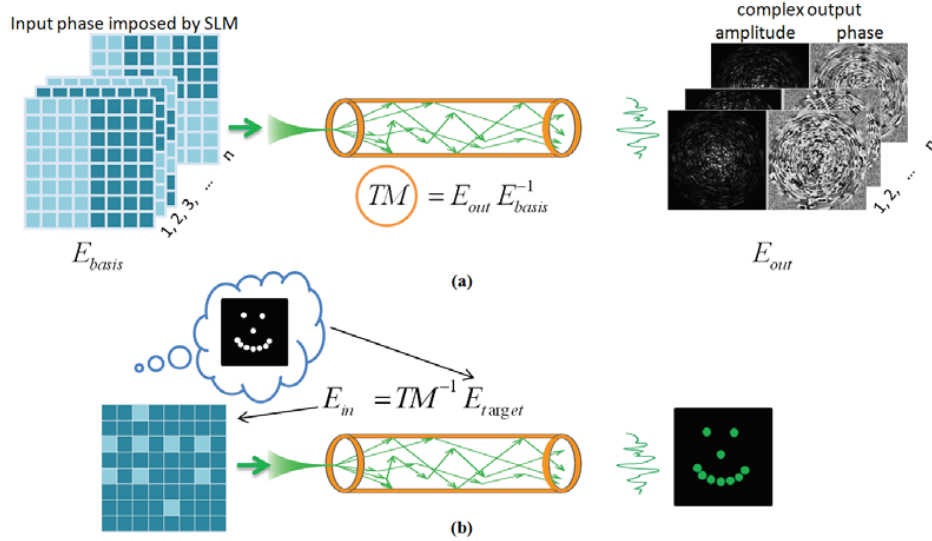


Figure 2:10 Measurement of a transmission matrix of a multimode optical fiber. (a) Transmission matrix measurement. (b) Inversion of the transmission matrix and modulation at the input to generate the target intensity distribution at the output of the fiber.

The purpose of each one of the basis functions is to excite fiber modes independently in an ideal way in an orthogonal way. A careful selection of the basis is recommended for an optimal implementation of the method. For example, in the case of the pixel by pixel basis, since only one element of the spatial light modulator is coupling light into the fiber this approach is slow because it would require many measurements to excite most of the modes and has a very low diffraction efficiency. The mathematical function and the propagating wave approaches are more adequate in terms of measurement time and diffraction efficiency at the spatial light

modulator, but still could result in decimation or oversampling. If not all the fiber modes are excited in the transmission matrix measurement, the ability to focus light will not be the optimal one and the intensity focus and light patterns results in a decreased signal to noise ration than in a fully measured transmission matrix. In the case of oversampling, it gives a complete “sampling” of the fiber modes and exploits the medium to give rise to the highest signal to noise ration available with the number of modes present in the fiber, but could result in very large acquisition times. We found that an optical approach is to use a modal based basis to measure the transmission matrix response, because it fully excites all the available fiber modes without resulting in oversampling.

The mathematical representation of the optical transmission matrix is given by:

$$E_m^{out} = \sum_n t_{m \times n} E_n^{in}$$

Equation 2:23 – Input-output field relation of a multimode fiber as a transmission matrix.

Where  $E_n^{in}$  is the complex input field,  $t_{m \times n}$  is the transmission matrix and  $E_m^{out}$  is the complex field produced at the output of the fiber by the  $E_n^{in}$ .

Once the transmission matrix is measured it can be used as an optical element to focus light or to generate intensity, holographic or phase patterns or even act as a diffractive optical element if the linear system is characterized at several wavelengths on the other end of the fiber [24]. By inversion of the matrix, the complex wavefront that has to be modulated at the input of the multimode fiber to generate the desired phase or intensity pattern on the other side is given by:

$$E^{in} = t_{m \times n}^{-1} E^{target}$$

Equation 2:24 – Calculation of the input field to produce a desired target field  $E^{target}$ .

### 2.3.1 Experimental setup for the measurement of the transmission matrix

In the case presented below, the transmission matrix was measured using a phase-modulating representation of the Hadamard basis. With an adequate selection of number of basis functions it can provide a good characterization of the multimode fiber.

As mentioned before, light propagation through a multimode fiber scrambles light and a phase and intensity pattern arises at the output of the fiber. If the wavefront of the beam before entering the scattering medium is modulated with a set of different phase masks and their individual respective complex output fields are measured, we can obtain a matrix that represents this linear input-output field relationship. The accuracy or similarity between the measured matrix and the occurring scrambling phenomenon will depend on the number of basis functions that we modulate when obtaining the matrix and the number fiber modes that can be excite in the fiber.

The phase and amplitude of the scrambled light at the distal end of the fiber can be measured using an off-axis holographic technique as shown in Figure 2:11 using the optical path shown with dashed lines in the figure. Alternatively, the phase and amplitude of the scrambled light

at the distal end of the fiber can also be measured using a common path method adopted from [25] in which the reference phase, modulated on the outer area of the SLM, propagates through the fiber as well. The advantage of the common path configuration is that it is less sensitive to phase instabilities during the TM measurement, produced for example by air flows or gradients of temperature produced by components in the optical table that dissipate heat such as the laser. Those perturbations, in off axis holographic arrangements, may introduce optical path changes in the reference, the object or both beams. In those cases, a phase drift tracking and correction algorithm can be implemented [12].

The setup that we used to measure the transmission matrix is shown in Figure 2:11. A collimated Gaussian beam from a continuous wave laser  $\lambda = 532 \text{ nm}$  is expanded and divided by a polarizing beam splitter (PBS) into a reference and an object beam in the case of the off-axis configuration. The phase of the object beam is spatially modulated using a set of  $N$  different orthogonal basis functions by using a phase-only liquid crystal spatial light modulator (Holoeye Pluto SLM). Walsh functions are used as basis functions as described in [25].

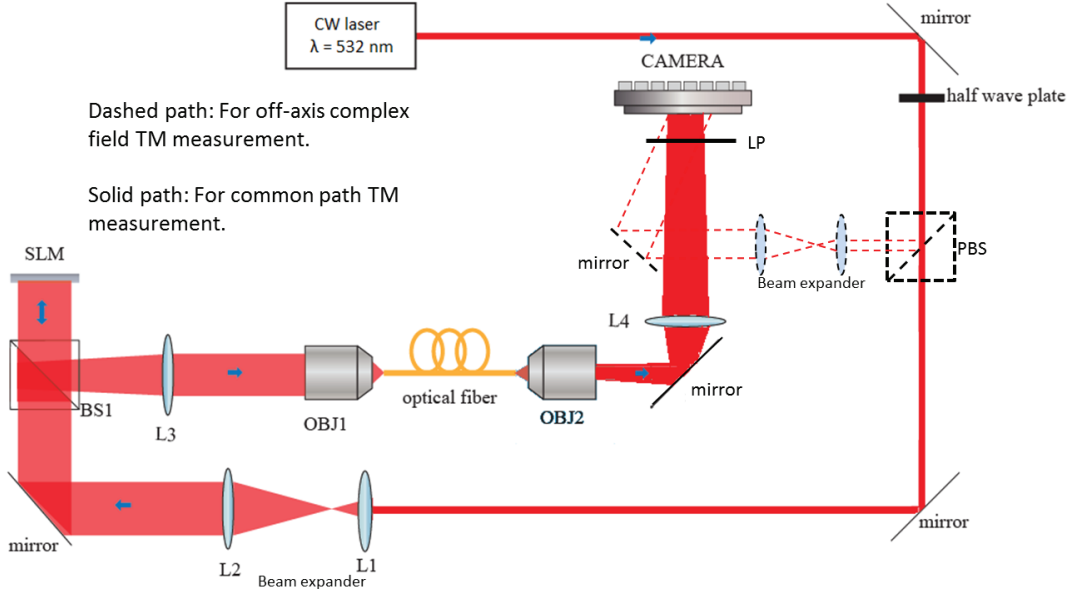


Figure 2:11 Experimental setup to perform a measurement of the transmission matrix of a multimode optical fiber.

Each element of a Walsh basis vector can only take two values, which is enforced as phases on the SLM. Using the Walsh basis functions the simultaneous use of all segments of the SLM instead of a pixel by pixel modulation increases the signal to noise ratio. The modulated light is coupled into a 2 m long multimode fiber (diameter =  $50 \mu\text{m}$ ,  $\text{NA} = .22$ ) by a 20X microscope objective OBJ1. The output of the fiber is imaged on the surface of CAMERA 2 where, in the off-axis configuration, it is interfered with the reference beam coming from PBS. The angle between the reference beam and the object beam is adjusted until achieving an adequate separation of the interference terms in the Fourier space. Taking the Fourier transform of the interference pattern a spatial band-pass filter is digitally applied to obtain only the desired interference term. To remove the  $k$  vector modulation, the filtered component is shifted to the origin

in the Fourier domain, its Fourier transform is taken and the resulting field is stored in the memory of the computer. This is shown in Figure 2:12.

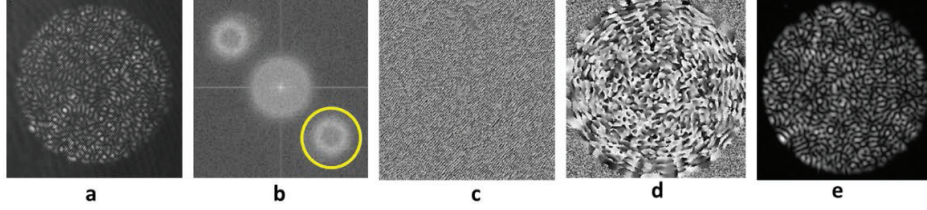


Figure 2:12 Off-axis holographic arrangement for the measurement of a complex field. (a) Digital hologram. (b) Fourier transform of the digital hologram. (c) Reconstructed phase from the first order of the digital hologram (Inverse Fourier transform of the filtered first order). (d) Reconstructed phase with shifted spectrum to the zero order ( $k$  vector removed) (e) Reconstructed amplitude.

The process is repeated for all of the  $N$  Walsh basis functions. Since phase drifts between the object and reference beams are present in the setup, a method for compensating such drifts is required, such as a phase tracking algorithm. Nevertheless, inspired from the work of [11] we adopted a different approach, in which phase can be calculated at the distal end of the fiber by only doing intensity measurements. In such case, the dashed path shown in Figure 2:11 is not used and the laser beam is expanded and directed to the SLM, which modulates both the basis function and, in the outer part, the reference beam as shown in Figure 2:13. . Both the reference and basis function are coupled and propagated through the fiber. Using only intensity measurements on the camera of Figure 2:11 [26], the complex field can be calculated using Equation 2:25. The drawback of this approach is that to measure the phase for a single basis input, four different measurements must be done, rather than one as in the off axis case. To calculate the complex field at the output of the fiber for each basis function  $n$ , we use the following expression [26]:

$$k_{mn} = \frac{(I_m^0 - I_m^\pi)}{4} + i \frac{(I_m^{\frac{3\pi}{2}} - I_m^{\frac{\pi}{2}})}{4}$$

Equation 2:25 – Calculation of a complex field from intensity measurements

Where  $k_{mn}$  is the complex field produced by the  $n$ th basis function, and  $I$  is the measured intensity for different reference phases from 0 to  $3\pi/2$ . An example of such measurement is represented in Figure 2:13.

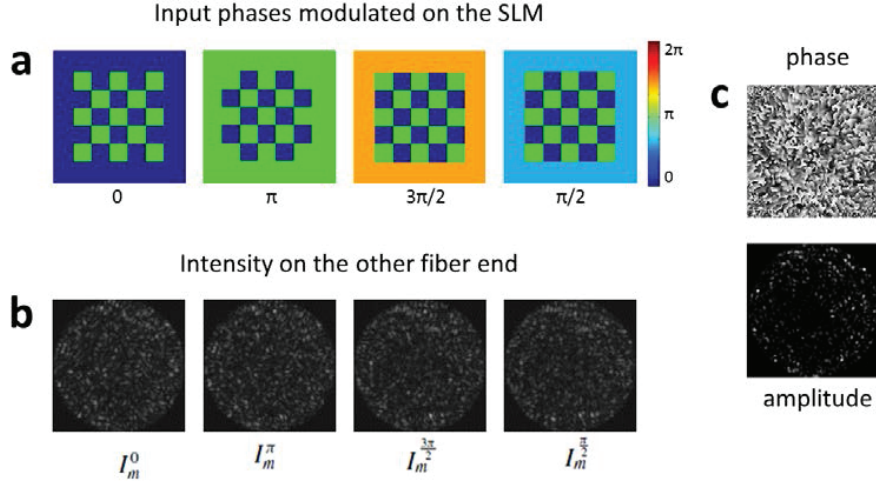


Figure 2:13 Common path principle for the measurement of a complex field. (a) A basis function is modulated on the SLM with together with four different reference phases in independent sequential measurements. (b) For each one of the referenced input functions the intensity on the other fiber end is measured. (c) Using Equation 2:25 phase and amplitude of the distal field is calculated.

Once the transmission matrix is obtained, it can be used to calculate the phase that modulated at the input can produce the desired output. As mentioned before, an inversion of the matrix is needed. The inverted complex matrix pre-multiplying the desired pattern gives the corresponding input field. In our particular implementation, only the phase is modulated.

The results of light focusing using this common path method are shown in Figure 2:14. Since ambient light or laser phase drifts introduce noise to the measured transmission matrix, using a method adopted from [11] noise can be reduced by decomposing the measured transmission matrix into its singular values form, discarding the low amplitude singular values susceptible to noise, and reconstructing the matrix. This improvement is achieved because in the measured transmission matrix, low amplitude matrix elements values are “amplified” when inverted, therefore the noise from those low amplitude elements is increase. With this correction, a two-fold improvement in the focused spot is achieved as shown in Figure 2:14. In specific, light focusing using the measured transmission matrix is done by first defining a target output field which in this case consists on an intensity equal to 1 at the point in which we want the phase conjugated spot, and zero everywhere else. Then we invert the matrix and calculate what must be the input to achieve such spot, and finally the computed phase is enforced by the SLM. This is depicted in Figure 2:10 (b). The process of decomposition of the transmission matrix  $H$  into its singular values is shown in the following equations:

$$M^+ = V \left[ \frac{1}{\lambda_i} \delta_{i,j} \right]_{i,j} U^* = V \begin{bmatrix} \frac{1}{\lambda_1} & 0 & \dots & 0 \\ 0 & \ddots & & \\ & & \frac{1}{\lambda_N} & \\ \vdots & & & 0 \\ 0 & \dots & 0 & 0 \end{bmatrix} U^* = V \Sigma^+ U^*$$

Equation 2:26 – Singular value decomposition of a matrix  $M$ .

Where  $M$  is the transmission matrix and  $+$  denotes inverse.

In the matrix  $M^+$ , small singular values, more susceptible to noise, become large numbers upon inversion. By discarding some of the largest inverted values of  $\Sigma^+$  and calculating  $M$ , an enhancement in the intensity focus is observed.

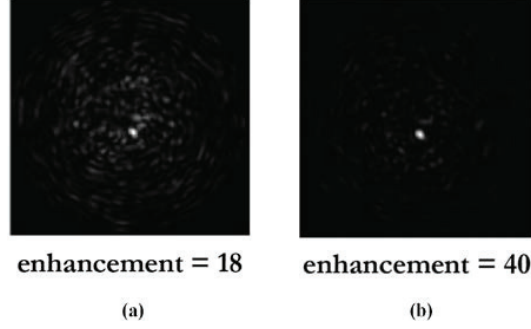


Figure 2:14. Light focusing using the transmission matrix method. Spot size is  $8.5\mu\text{m}$ . (a) Example of a phase conjugated intensity spot generated using a measured transmission matrix. (b) Similar to (a) but using singular value decomposition for noise reduction (20% of inverted singular values were discarded). Enhancement denotes the spot to background intensity ratio.

A quantity used to assess the quality of the reconstructed spot is the enhancement  $\eta$ , defined as the ratio of peak intensity over the average intensity detected at the distal end of the fiber.

$$\eta = \frac{I_{peak}}{\langle I \rangle}$$

Equation 2:27 – Intensity enhancement of a light focused spot.

In scattering media,  $\eta$  is related to the number  $N$  of modes controlled by the SLM as shown in the following expression [1]:

$$\eta \approx \frac{\pi}{4}(N - 1) + 1$$

Equation 2:28 – Intensity enhancement relation to the number of controlled modes.

For the case of multimode fibers, we can assume that  $N$  is proportional to the number of excited modes.

An alternative method to reduce the noise in a multimode fiber consists on using a modified matrix inversion given as follows, where  $W$  denotes the noise reduced inverted matrix [27]:

$$W = [M_{obs}^\dagger \cdot M_{obs} + \sigma I]^{-1} M_{obs}^\dagger$$

Equation 2:29 – Noise-reduced transmission matrix.

With this approach, a value of the scalar  $\sigma$  that maximizes the enhancement of a light focus can be found. Figure 2:15 shows the enhancement of a light focus for different values of sigma:



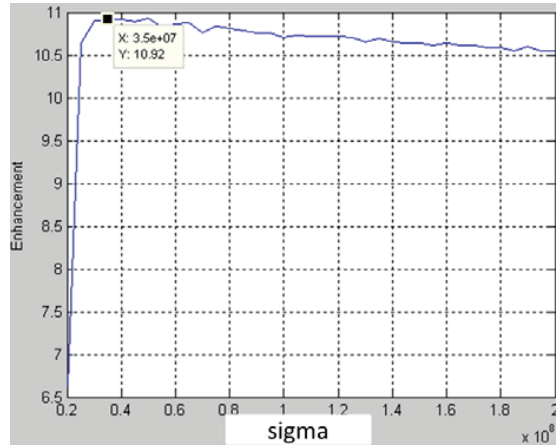


Figure 2.15. Enhancement of a focused spot using the noise reduced matrix inversion.

Using the transmission matrix approach, if no simultaneous phase, amplitude and polarization control is available, then generated pattern is just an approximation of the desired one. Usually only the phase of the calculated complex field to be enforced at the input of the fiber is actually modulated.

### 2.3.2 Advantages and limitations of the transmission matrix approach

The transmission matrix is a very powerful tool that allows the generation of intensity and phase patterns through scrambling media such as a multimode optical fiber. It not only allow the generation of phase patterns at the plane or working distance where the complex field on the other side of the medium is measured, but also, using numerical propagation, allow the generation of any spatial profile at different distances from the fiber facet. This is very powerful but simple to implement. To do so, the desired pattern is numerically propagated from the projection plane to the plane where the matrix was measured. This is pretty simple and can be easily achieved by a discrete computer implementation of light propagation in free space, such as the Fraunhofer or Fresnel propagator, depending on how far the pattern needs to be generated. Then, the calculated field is plugged as the target field to be generated with the transmission matrix and using Equation 2:24, the complex field that has to be enforced to generate the desired pattern is obtained.

The capability to generate intensity patterns or simultaneous light foci is advantageous in some applications, such as single-shot imaging, single photon fluorescent imaging, optical tweezers for micro-manipulations or one-photon polymerization. However, the main drawback of the transmission matrix approach is that it is very time consuming to characterize the entire input-output complex field response of a multimode fiber or scattering media, especially if the fiber core is larger than 200  $\mu\text{m}$ , and the numerical aperture larger than 0.22. The number of fiber modes, directly related to the number of basis functions required to completely measure the transmission matrix, is proportional to the square of the normalized frequency or V number of the fiber mentioned at the beginning of this chapter, which in turn is proportional to the fiber radius. Therefore, a doubling in the core diameter of the fiber results in a 4-fold of the measurement time and amount of memory required to measure and store the transmission matrix. In practical terms, in a 600 micrometer core diameter fiber with a



0.48 NA, an acquisition time of more than 10 hours and hundreds of gigabytes of RAM memory would be required (for this calculation, the number of fiber modes, and refresh rate of a phase only SLM, 20 Hz, were taken into account). For the applications of chapter 4 and 5, large field of views and large NAs are preferred. For two-photon endoscopy, two photon polymerization and material ablation, very high peak powers are required to produce nonlinear effects at the tip of the fiber. In those specific cases, the powerful capability of the transmission matrix for conforming light patterns cannot be fully exploited, because the generation of simultaneous spots or light patterns drops the power per spot, depending on the number of simultaneous diffraction-limited foci, reaching in some cases low intensities that can no longer trigger the two-photon effects. In those cases, other methods for light focusing result more convenient, such as time-gated digital phase conjugation which will be introduced in the next section of this chapter.

## 2.4 Control of pulsed light propagation using time-gated digital phase conjugation

As mentioned at the beginning of this chapter, another technique to achieve light focusing or pattern projection through scattering media is the so called optical phase conjugation. Consider the case shown in Figure 2:16. Light is focused on one end of a multimode fiber producing a speckle like intensity and phase pattern on the other side. If a phase conjugate mirror is placed on the other end of the fiber, light counter-propagates through the same medium interfering constructively at the location of the original focus or excitation pattern.

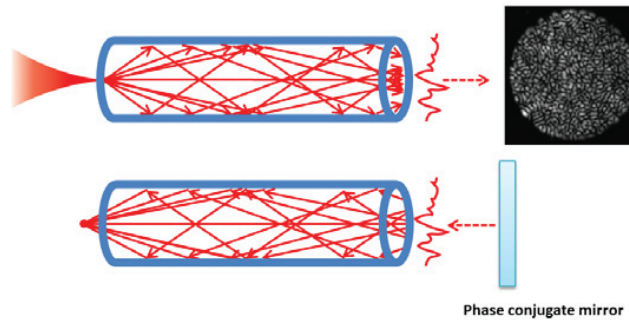


Figure 2:16. Optical phase conjugation in a multimode optical fiber. A light beam is focused in the facet of a multimode fiber generating a speckle pattern on the other side. With a Phase conjugate mirror, light counter propagates through the fiber converging at the location of the initial focus or intensity pattern.

A phase conjugate mirror can be implemented by a digital camera and a spatial light modulator as shown in Figure 2:17 and Figure 2:19. In the first step, the complex field at the output of the multimode fiber is characterized. This can be achieved using off axis holography, using a reference beam that is interfered with the fiber beam which in holographic terms would be the object beam. In the case the light source is a pulsed one, the reference beam also acts as a time-gating window, as will be explained in full detail in the next chapter. To record the digital hologram, the multimode fiber field and the reference beam both illuminate the digital camera. The interference pattern is the digital hologram. The complex amplitude of the fiber wave is given by:

$$O(x, y) = o(x, y) \exp(i\varphi_O(x, y))$$

Equation 2:30 – Object or fiber wave.

Where  $O$  is the real amplitude and  $\varphi_O$  is the phase, both dependent on the spatial coordinates  $x$  and  $y$ . The complex amplitude of the reference wave is described as:

$$R(x, y) = r(x, y) \exp(i\varphi_R(x, y))$$

Equation 2:31 – Reference wave.

Where  $a_R$  is the real amplitude and  $\varphi_R$  the phase of the reference wave. The two waves interfere at the surface of the digital camera as illustrated in Figure 2:17. The camera measures the intensity resulting from that interference which is given by [28]:

$$\begin{aligned} I(x, y) &= |O(x, y) + R(x, y)|^2 \\ &= (O(x, y) + R(x, y))(O(x, y) + R(x, y))^* \\ &= R(x, y)R^*(x, y) + O(x, y)O^*(x, y) \\ &\quad + O(x, y)R^*(x, y) + R(x, y)O^*(x, y) \end{aligned}$$

Equation 2:32 – Intensity recorded as a digital hologram.

Each one of the terms of the previous expression are shown in Figure 2:18.

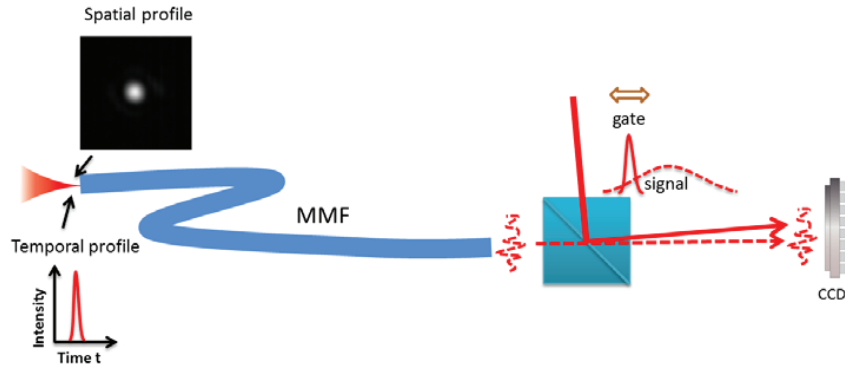


Figure 2:17. Characterization of the complex field at the multimode fiber output using off-axis digital holography. The figure describes the characterization in the general case in which the laser beam can be either monochromatic or a pulsed light source. In the pulsed case the reference not only interferes to acquire the hologram, but also acts as a time-gating window.

The camera measures the intensity that contains the phase and amplitude information of the object beam. By calculating the Fourier transform of the digital hologram, the first, minus one and zero order holographic terms can be identified. They are spatially separated in the Fourier domain as shown in Figure 2:18. Then, the first order term that contains the phase and amplitude information of the object beam or field coming from the fiber, is filtered using a digital band-pass filter. By calculating the inverse Fourier transform of the filtered term, the amplitude and phase information of the object field can be obtained. By taking the conjugate of this calculated phase, a reconstruction of the object beam can be reconstructed on the SLM as shown in Figure 2:19 and is given by the product of the reference wave multiplied by the transmittance of the hologram:

$$R(x, y)I(x, y) = R(x, y)r^2 + o^2R(x, y) + O(x, y)r^2 + r^2O^*(x, y)$$

Equation 2:33 – Reconstructed hologram.

Where the first and second term corresponds to the reference wave scaled by a factor. This term represents non-diffracted light and is known as the zero order that passes through the hologram. The third term corresponds to a virtual image of the reconstructed fiber field. The fourth term is the rea image, which is the wave that, upon phase conjugation, counter-propagates through the fiber.

The implementation of the phase conjugate mirror require a precise alignment of the SLM and the camera. Usually, the camera is chosen pixel match with the SLM, which means that the size and pitch of the SLM and camera pixels is the same. Micrometer accuracy alignment in position and tilt angles is required in order to achieve a correct phase conjugate implementation.

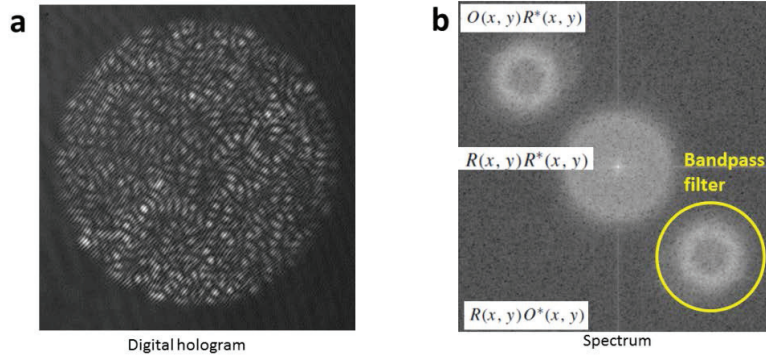


Figure 2:18. Off-axis digital holography. (a) Digital hologram. (b) Fourier transform of the digital hologram. All holographic terms are separated in the spectral domain. Fiber diameter is 200 micrometers.

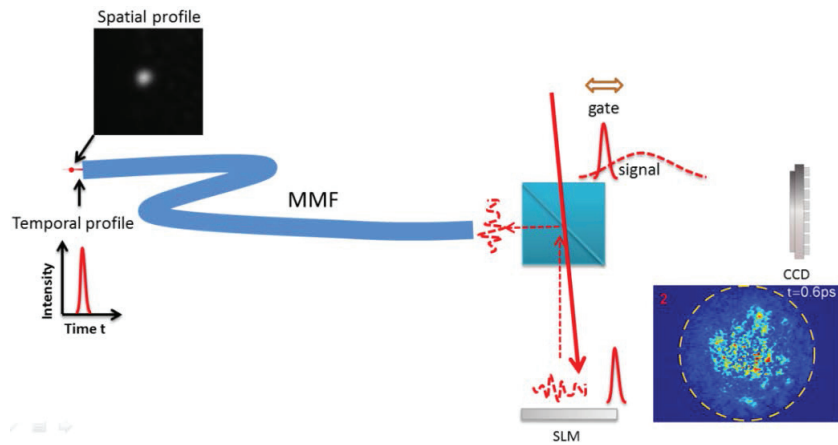


Figure 2:19. Reconstruction of the phase-conjugate replica of the characterized field. Light counter propagates through the fiber generating the original excitation.

The general case of optical phase conjugation is known as time reversal. This is pretty common and easy to implement in electronics, in which a microwave signal, for example, can be time

reversed by measuring and reproducing with an array of antennas the same signal but in reverse order. This is possible to modulate in electronics. However, in optics, a truly time reversal implementation capable of modulating phases within the temporal duration of an optical pulses of hundreds of femtoseconds in pulse length, has not been possible to implement. To achieve time reversal with optical pulses a time-varying SLM with refresh rate of femtoseconds would be required, which is not possible up to date. The closest to time reversal in non-monochromatic light sources is a pulse shaper, which can imprint any temporal profile on an optical pulse. However, it only acts on a single Gaussian light beam, and not on any complex intensity distribution such as a time-varying speckle patterns or the time-varying field produced in light propagation in multimode fibers.

To overcome this problem, we designed a time-gated version of digital phase conjugation to implement a phase conjugate mirror that acts on optical pulses. The basic principle is the same as in digital holographic approach described above, but the difference is that the reference beam acts as a sampling window as well. This allows the recording of holograms of a time-varying field at the time set by the reference. This phase conjugation alternative discards the light field arriving at different times other than the ones of the gating window, giving a poor light focusing result compared to the monochromatic case. However, by selecting the right medium this effects can be mitigated. Figure 2:20 and Figure 2:21 show the light focusing capability of time-gated digital phase conjugation. As can be seen in the figures, time-gated DPC reduces temporal broadening due to modal dispersion. The selection of a graded index multimode fiber allow the simultaneous characterization and control of a larger number of time-sampled modes, giving an intensity focus 100 times larger than in step index fibers, which can potentially produce nonlinear effects.

#### 2.4.1 Time-grated digital phase conjugation in step and graded index MMFs

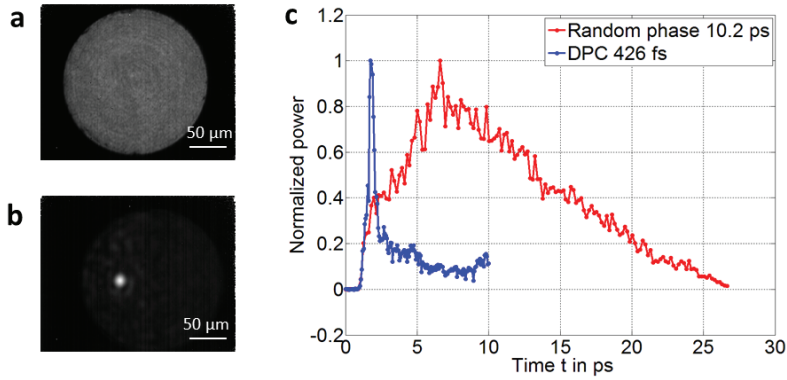


Figure 2:20. Time-gated digital phase conjugation in a step multimode optical fiber. (a) Intensity profile on the other side of the fiber when a large mode excitation is modulated on the SLM. (b) Intensity profile on the other side of the fiber when a phase-conjugate modulation is performed by the SLM. (c) Interferometric cross correlation between a reference beam and the fiber beam. Time gated DPC excites modes with the same modal speed giving a shorter temporal profile of coherence. (Not to confuse with pulse length). Fiber is step index multimode 200 μm core, NA=.39, length= 30 cm,  $\eta = 10$ , Spot size 13.8 μm.

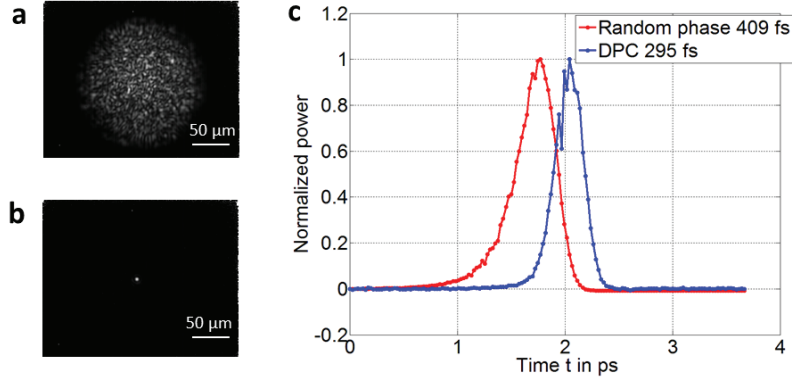


Figure 2:21. Time-gated digital phase conjugation in a graded-index multimode optical fiber. (a) Intensity profile on the other side of the fiber when a large mode excitation is modulated on the SLM. (b) Intensity profile on the other side of the fiber when a phase-conjugate modulation is performed by the SLM. (c) Interferometric cross correlation between a reference beam and the fiber beam. Time gated DPC excites modes with the same modal speed giving a shorter temporal profile of coherence. (Not to confuse with pulse length). The temporal profile of the random phase is shorter than in the step index case due to the reduced modal dispersion of graded index fibers. Fiber is graded index, multimode, core diameter 200  $\mu\text{m}$ , NA = 0.27, length = 30 cm,  $\eta = 1'100$ , 5  $\mu\text{m}$  spot size.

Specific details about time-gated digital phase conjugation and many experimental results and characterization of the light foci in terms of spot size and pulse length are presented in the next chapter, which treats exclusively about this method.

## 2.5 Applications

Differently to focusing of monochromatic light through multimode fibers, the delivery of femtosecond optical pulses could enable all sorts of non-linear phenomena at the tip of an ultra-thin needle. Some of the possible applications are: fluorescent endoscopy in the multiphoton modality, micro-manipulation in the form of optical tweezers, spatial division multiplexing for information transmission, material processing in places of difficult access such as laser cutting, two-photon polymerization or material ablation among other applications where femtosecond pulses intervene. In the present thesis we apply the light focusing principles presented in the next chapter in two novel applications that were not demonstrated in multimode fibers before: two-photon imaging and two-photon polymerization.

## 2.6 Limits of controlled light propagation in multimode fibers

### 2.6.1 Fiber bending

Fiber bending introduces changes in the propagation of the fiber modes. Therefore, for light focusing and pattern projection through multimode optical fibers, recalibration is required if the fiber is bent. However, this can be solved by incorporating a bending-compensation method via geometric characterization of fiber bending [29] or by measurement of the proximal speckle of a fiber with a distal reflective coating [30].

### 2.6.2 Spatial light modulators

The applications mentioned in the previous section require a fast refresh rate of the spatial light modulator in order to be viable. For example, for in-vivo two-photon endoscopy, the scanning must be performed over the field of view at a rate faster than the natural micro-movements of the specimen. For prototyping and in the research presented in this thesis we employed phase-only spatial light modulators for providing the highest diffraction efficiency though a slow refresh rate (commonly from 20Hz to 200Hz). The resolution of this kind of modulators is high ( $\sim 2\text{Mpixels}$ ). Another light modulator is the digital micromirror device (DMD). These modulators can reach high refresh rates in the order of 20KHz but are binary amplitude modulators. They do not produce direct phase modulation. To modulate phase a Lee holography approach, for example, can be used but at the cost of a very low diffraction efficiency ( $\sim 5\%$ ), making them unsuitable for high power applications such as those required for two-photon phenomena. Another light modulator consists of deformable mirrors, which have speeds of tens of kilohertz but have a low resolution and are usually used for aberration corrections. A promising implementation of a fast phase modulator is the piston based modulator. It consists of a micromirror array where the pistons can move back and forth with a sub-wavelength resolution allowing a direct spatial phase modulation. This kind of devices can reach refresh rates in the order of tens of Kilohertz. Unfortunately its development was halted and are not commercially available. All these types of light modulators are shown in Figure 2:22.

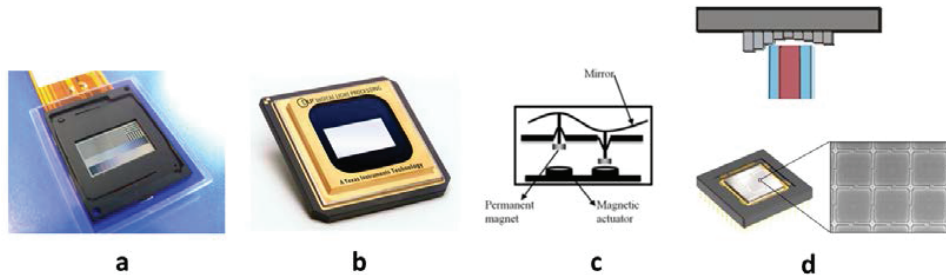


Figure 2:22. Types of spatial light modulators. (a) Phase only SLM (Holoeye AG). (b) DMD (Texas Instruments). (c) Deformable mirror (Adaptive Optics and Astronomy Pierre-Yves Madec). (d) Piston based phase modulator (Fraunhofer Institute).

## 2.7 References

1. P. Sheng, Introduction to Wave Scattering, Localization, and Mesoscopic Phenomena (Academic Press, 1995).
2. I. N. Papadopoulos, S. Farahi, C. Moser, and D. Psaltis, "Focusing and scanning light through a multimode optical fiber using digital phase conjugation," *Opt Express* **20**, 10583-10590 (2012).
3. T. Cizmar and K. Dholakia, "Shaping the light transmission through a multimode optical fibre: complex transformation analysis and applications in biophotonics," *Opt Express* **19**, 18871-18884 (2011).
4. T. Cizmar and K. Dholakia, "Exploiting multimode waveguides for pure fibre-based imaging," *Nat Commun* **3**(2012).

5. R. Di Leonardo and S. Bianchi, "Hologram transmission through multi-mode optical fibers," *Opt Express* **19**, 247-254 (2011).
6. M. Kim, Y. Choi, C. Yoon, W. Choi, J. Kim, Q. H. Park, and W. Choi, "Maximal energy transport through disordered media with the implementation of transmission eigenchannels," *Nat Photonics* **6**, 581-585 (2012).
7. I. M. Vellekoop and A. P. Mosk, "Focusing coherent light through opaque strongly scattering media," *Opt Lett* **32**, 2309-2311 (2007).
8. D. B. Conkey, A. M. Caravaca-Aguirre, and R. Piestun, "High-speed scattering medium characterization with application to focusing light through turbid media," *Opt Express* **20**, 1733-1740 (2012).
9. J. Aulbach, B. Gjonaj, P. M. Johnson, A. P. Mosk, and A. Lagendijk, "Control of Light Transmission through Opaque Scattering Media in Space and Time," *Phys Rev Lett* **106**(2011).
10. O. Katz, E. Small, Y. Bromberg, and Y. Silberberg, "Focusing and compression of ultra-short pulses through scattering media," *Nat Photonics* **5**, 372-377 (2011).
11. S. M. Popoff, G. Lerosey, R. Carminati, M. Fink, A. C. Boccarda, and S. Gigan, "Measuring the Transmission Matrix in Optics: An Approach to the Study and Control of Light Propagation in Disordered Media," *Phys Rev Lett* **104**(2010).
12. D. Loterie, S. Farahi, I. Papadopoulos, A. Goy, D. Psaltis, and C. Moser, "Digital confocal microscopy through a multimode fiber," *Opt Express* **23**, 23845-23858 (2015).
13. D. Kim, J. Moon, M. Kim, T. D. Yang, J. Kim, E. Chung, and W. Choi, "Toward a miniature endomicroscope: pixelation-free and diffraction-limited imaging through a fiber bundle," *Opt Lett* **39**, 1921-1924 (2014).
14. I. N. Papadopoulos, S. Farahi, C. Moser, and D. Psaltis, "High-resolution, lensless endoscope based on digital scanning through a multimode optical fiber," *Biomed Opt Express* **4**, 260-270 (2013).
15. Y. Choi, C. Yoon, M. Kim, T. D. Yang, C. Fang-Yen, R. R. Dasari, K. J. Lee, and W. Choi, "Scanner-Free and Wide-Field Endoscopic Imaging by Using a Single Multimode Optical Fiber," *Phys Rev Lett* **109**(2012).
16. T. Cizmar and K. Dholakia, "Exploiting multimode waveguides for pure fibre based fluorescence imaging," *Proc Spie* **8572**(2013).
17. E. R. Andresen, G. Bouwmans, S. Monneret, and H. Rigneault, "Two-photon lensless endoscope," *Opt Express* **21**, 20713-20721 (2013).
18. E. E. Morales-Delgado, D. Psaltis, and C. Moser, "Two-photon imaging through a multimode fiber," *Opt Express* **23**, 32158-32170 (2015).
19. D. B. Conkey, N. Stasio, E. E. Morales-Delgado, M. Romito, C. Moser, and D. Psaltis, "Lensless two-photon imaging through a multicore fiber with coherence-gated digital phase conjugation," *J Biomed Opt* **21**(2016).
20. B. E. A. S. a. M. C. Teich, *Fundamentals of Photonics*, 2nd Edition ed. (Wiley).
21. J.-C. D. a. W. Rudolph, *Ultrashort Laser Pulse Phenomena (Second Edition)*, *Fundamentals, Techniques, and Applications on a Femtosecond Time Scale* (Elsevier 2006 ).
22. G. P. Agrawal, *Fiber optic communication systems*, Third Edition ed. (Wiley Interscience).
23. W.-H. Lee, "Binary computer-generated holograms," *Appl Optics* **18**, 3661-3669 (1979).



- 24. S. M. Popoff, G. Lerosey, R. Carminati, M. Fink, A. C. Boccarda, and S. Gigan, "Measuring the Transmission Matrix in Optics: An Approach to the Study and Control of Light Propagation in Disordered Media," *Phys Rev Lett* **104**, 100601 (2010).
- 25. S. M. Popoff, G. Lerosey, M. Fink, A. C. Boccarda, and S. Gigan, "Controlling light through optical disordered media: transmission matrix approach," *New J Phys* **13**(2011).
- 26. A. Dubois, L. Vabre, A.-C. Boccarda, and E. Beaurepaire, "High-resolution full-field optical coherence tomography with a Linnik microscope," *Appl Optics* **41**, 805-812 (2002).
- 27. S. Popoff, G. Lerosey, M. Fink, A. C. Boccarda, and S. Gigan, "Image transmission through an opaque material," *Nat Commun* **1**(2010).
- 28. W. J. U. Schnars, *Digital holography, Digital hologram recording, numerical reconstruction and related techniques* (springer).
- 29. M. Ploschner, T. Tyc, and T. Cizmar, "Seeing through chaos in multimode fibres," *Nat Photonics* **9**, 529-+ (2015).
- 30. R. Y. Gu, R. N. Mahalati, and J. M. Kahn, "Design of flexible multi-mode fiber endoscope," *Opt Express* **23**, 26905-26918 (2015).





# Chapter 3   Focusing   optical   pulses through multimode fibers

The previous chapter described how light propagation through multimode fibers suffers from spatial distortions that lead to a scrambled intensity profile. Techniques for the correction of such distortions using various wavefront control methods have been discussed in the continuous wave case. However, in the ultra-fast pulse regime, modal dispersion temporally broadens a pulse after propagation.. This chapter deals with the extension of such methods to the transmission of optical pulses that form a spatial focus on the other side of the fiber.

In this chapter a technique to generate ultrashort focused pulses through multimode fibers based on digital phase conjugation DPC is presented. Spatial and temporal distortions due to modal dispersion occurring in the fiber are compensated by a selective phase conjugation process, where modes of similar propagation constants are spatially excited to form an intensity focus. The results of this work set the basis for multi-photon imaging, two-photon polymerization and material ablation through ultrathin light guiding probes.

Some results of the work presented in this chapter were published in the Optics Express journal as:

E. E. Morales-Delgado, S. Farahi, I. N. Papadopoulos, D. Psaltis, and C. Moser, ***"Delivery of focused short pulses through a multimode fiber,"*** Opt Express 23, 9109-9120 (2015).

## 3.1   Introduction

The large information capacity of multimode optical fibers, given by their number of supported propagation modes, has allowed new miniaturized devices for image transmission through multimode fibers [1-4] and represent potential high throughput channels for optical communications [5,6].

The transmission of an ultrashort pulse through a multimode fiber mainly suffers from modal dispersion that leads to a scrambled spatial intensity and a temporal broadening. This prevents the conservation of the ultrashort temporal profile and of the spatial distribution as light goes through the fiber. Although the emerged pattern looks like a random field, its origin is linear and deterministic when nonlinear effects are not present. Therefore, it is a reversible phenomenon.

Current optical communications mainly rely on single mode fibers, which allow a single traveling mode with a well-defined spatial profile. However, pulse duration is affected by chromatic dispersion and optical non-linear effects. Several methods have been developed to counteract temporal spreading to recover a pulse of similar duration as the original. For example, temporal pulse shaping methods and phase conjugation has been used successfully [7-9].

When a multimode fiber is used, additional temporal broadening takes place due to modal dispersion, i.e., the different modes propagating in the fiber have different group velocities. Contrary to the case of single mode fibers where the spatial profile is maintained during propagation, the pattern emerging from a multimode fiber does not resemble the pattern launched at the input as explained before. Adaptive methods have been proposed to compensate for modal dispersion in telecommunications in order to deliver femtosecond pulses through multimode fibers but no simultaneous spatial control has been achieved [10,11].

Regarding the spatial domain, in the monochromatic case, optical phase conjugation was first suggested [12,13,14] and demonstrated as a way to undo the modal scrambling and transmit images through multimode fibers. More recently, the field was revisited in the digital domain, where several methods such as iterative algorithms [15,16], transmission matrix measurement [2,3,17] or digital phase conjugation [18] have been successfully used to spatially focus light and even to image through multimode optical fibers [1-4]. However, the control of both the spatial profile and the temporal duration of pulses through multimode fibers have not yet been demonstrated.

Interestingly, spatial wavefront shaping techniques have been proposed for focusing through a scattering medium in space and time [19,20]. These methods rely on iterative algorithms that optimize a signal, such as a two-photon signal, that strongly depends on the simultaneous spatial and temporal focusing of a light pulse. They are based on the fact that light propagating through such scattering media is re-radiated at every scattering event, creating different light paths. Each path is associated with a respective time delay. This spatio-temporal relationship allows the correction of both temporal and spatial distortions using only spatial degrees of wavefront control.

For information transmission, delivery of an arbitrary spatial distribution of ultrashort light pulses could enable an efficient spatial division multiplexing of orthogonal communication channels with limited dispersion [6]. In the field of imaging, the ability to deliver and digitally scan focused ultrashort pulses would allow multiphoton lensless imaging, which have only been accomplished using fiber bundles [21].

This chapter demonstrates the delivery of spatially focused optical pulses of 500 fs pulse length through a multimode optical fiber. The proposed method minimizes pulse broadening due to modal dispersion in the multimode fiber by selectively counter-propagating only a group of modes of similar group velocities. Specifically, as an initial step, light is coupled into the distal side of an optical fiber. Time-gated interferometry [22] and digital holography are used to characterize the optical field at the proximal side. Then, using digital phase conjugation (DPC), a reconstruction of a time-gated field is performed with a spatial light modulator. The reconstructed field counter-propagates through the fiber generating an ultrashort focused

pulse at the distal end of the fiber. Since the power of the counter-propagated field is spatially spread on the various excited modes, this approach does not introduce nonlinear effects on the delivered focused pulse. Considering a nonlinear threshold  $P_{th}$  of  $2 \text{ GW/cm}^2$  in silica fibers and using a standard Titanium Sapphire laser source of 100 fs in pulse length  $P_{length}$  with 800 mW of average power  $P_{ave}$  and a repetition rate  $R_{rep}$  of 76 MHz, the threshold diameter  $D_{th}$  in a multimode fiber for nonlinear effects to occur would be  $81 \text{ }\mu\text{m}$  ( $D_{th} = \sqrt{(P_{ave}/(R_{rep}P_{length}P_{th}))}$ ). The experiments demonstrated in this thesis deal with fiber cores larger than  $200 \text{ }\mu\text{m}$  and couple into the fiber less than 20 % of the available laser power due to the use of a spatial light modulator. Therefore, nonlinear effects are not introduced in the optical pulse propagating in the fiber. Moreover, two-photon absorption produced by the delivered spot on the other side of the fiber is demonstrated. Additionally, transmission of temporally separated focused pulses is demonstrated.

## 3.2 Experimental setup for selective modal excitation

### 3.2.1 Chirped pulse amplification

The beam from a pulsed laser source (ORIGAMI-15 from OneFive;  $\lambda=1550 \text{ nm}$ ; spectral width  $\sigma\lambda=15.4 \text{ nm}$ ; pulse energy = 2 nJ) is amplified by a custom built chirped pulse amplification unit (CPA) shown in Figure 3:1. This CPA stage stretches the optical pulse from 170 fs to 100 ps,. This long pulse is used as a seed for a fiber amplifier which is then recompressed at the amplified output. Stretching is necessary to amplify optical pulses, otherwise the high peak powers introduce nonlinearities to the amplified pulse and could reach the damage threshold of the fiber amplifier producing damage. The output of the amplifier has a temporal duration of 440 fs, with a repetition rate of 40 MHz and a maximum average power of 1.2 W, yielding a pulse energy of 20 nJ. This is the pulse used for all the experiments described next. The specific design of the stretcher and compressor are shown in Figure 3:2 and Figure 3:3.

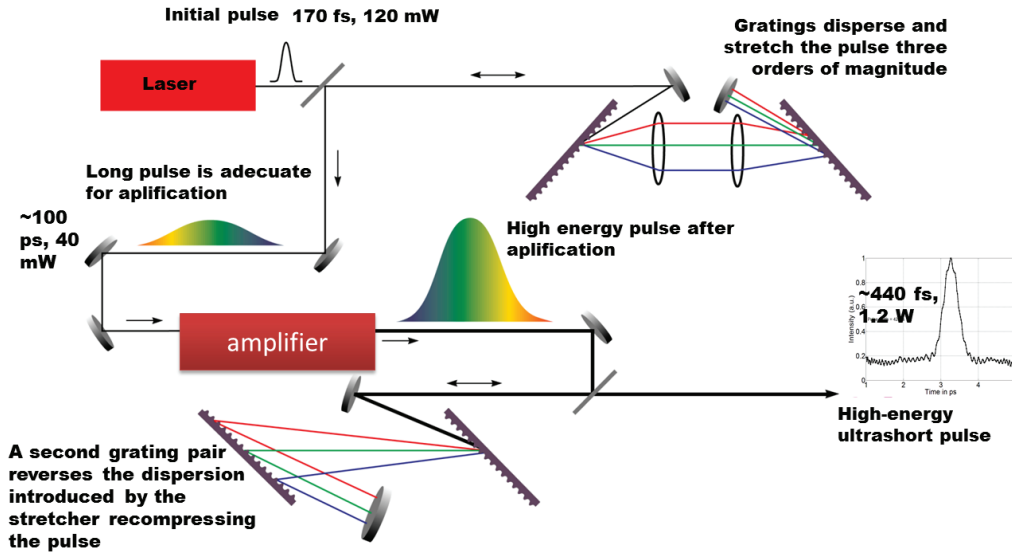


Figure 3:1 Chirped pulse amplification.

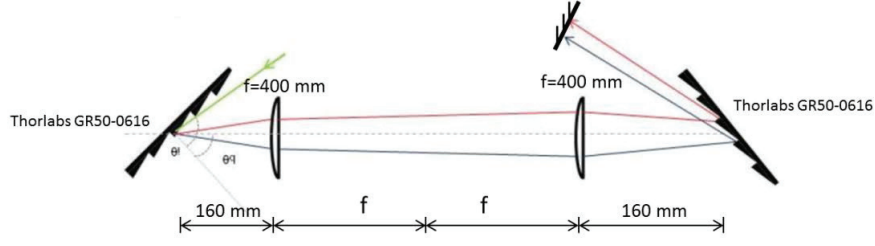


Figure 3:2 Pulse stretcher.

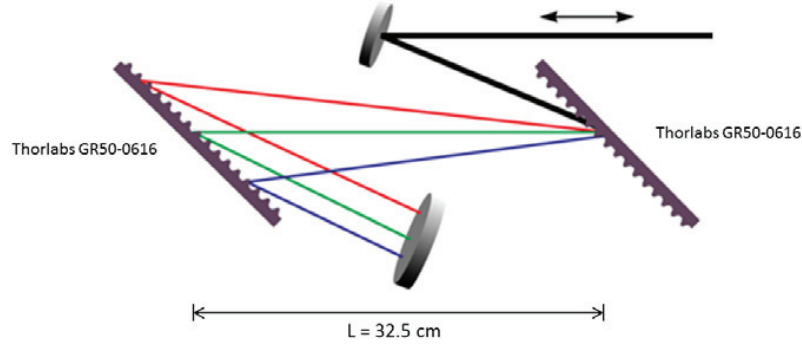


Figure 3:3 Pulse compressor.

### 3.2.2 Calibration – mode selection

The selective DPC technique consists of two separate steps: a calibration step for mode selection and a reconstruction step. Initially the output of the CPA is focused, at the distal side, close to the facet of a multimode fiber (core diameter = 200  $\mu\text{m}$ , NA = 0.39, length = 0.3 m, number of supported modes  $M \approx 103$ ) as illustrated in Figure 3:4. The  $M$  excited modes propagate with different propagation constants and acquire different phase shifts, leading to a scrambled amplitude and phase field at the proximal side of the fiber. This field can be expressed as a linear combination of the supported modes of the fiber (one polarization) with different scaling coefficients and phase factors around a carrier frequency:

$$E_{\text{out}}(x, y, t) = \sum_{m=1}^M a_m(t) \psi_m(x, y) e^{j\phi_m(x, y, t)} e^{-j\omega_0 t}$$

Equation 3:1

where  $a_m(t)$  is the time dependent scaling coefficient of mode  $m$ ,  $\psi_m(x, y)$  is the amplitude of the wave function of mode  $m$ ,  $\phi_m(x, y, t)$  is the corresponding modal phase, and  $\omega_0$  is the carrier frequency. In this form, propagation losses, material dispersion and the phase shift introduced during propagation are included in the terms  $a_m(t)$  and  $\phi_m(x, y, t)$ . Figure 3:5 (a) shows the intensity of the field  $E_{\text{out}}(x, y, t)$  as measured by Camera 1.

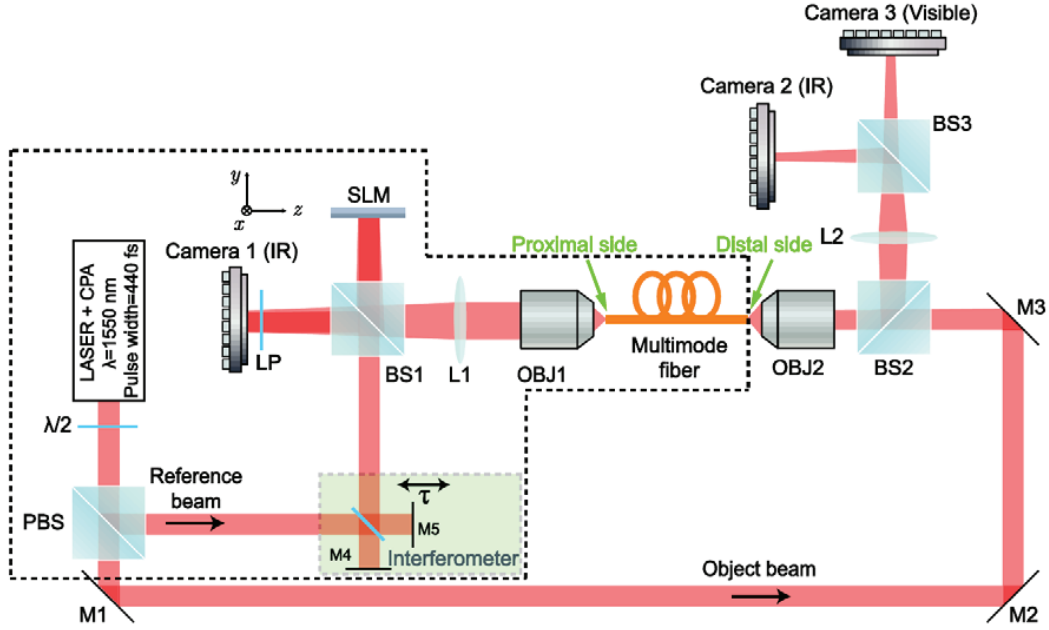


Figure 3:4 Experimental Setup. Calibration step. The beam from the CPA unit is divided by a polarizing beam splitter PBS into a reference and an object beam. The object beam is coupled into the multimode fiber by a 20X microscope objective OBJ2. The output of the fiber is imaged on the infrared Camera 1 by a 20X microscope objective (OBJ1) and the lens (L1),  $f=150$  mm, where it is interfered with the reference beam obtained by reflection from the beam splitter BS1. For each delay  $\tau$ , a digital hologram is recorded. Reconstruction step. The time-sampled field is reconstructed by the reference and phase conjugated using a spatial light modulator SLM. The reconstruction is imaged on the fiber by the lens L1 and the 20X microscope objective OBJ1. The reconstructed field counter-propagates generating the short focused spot on the distal side of the fiber. This spot is imaged on Camera 2 using a 4f system (OBJ2 and lens L2,  $f=300$  mm). Moreover, the spatio-temporal duration of the phase conjugated spot and its surrounding background is measured on each pixel of a silicon-based detector (Camera 3) using second order (interferometric) autocorrelation, by introducing on the reference the collinear time-delayed replicas required for this measurement, using the Michelson interferometer. The non-linearity in the second order autocorrelation is a two-photon process occurring in the silicon camera. The dashed polygon encloses a possible embodiment of an imaging device based on our method.

To characterize the field  $E_{out}(x, y, t)$  we interfere it off-axis with a reference pulse at the plane of Camera 1. The reference pulse can be described as,

$$E_{ref}(x, y, t - \tau) = a_{ref}(x, y, t - \tau) e^{-j a_0(t - \tau)}$$

Equation 3:2

where  $a_{ref}(x, y, t - \tau)$  is the complex amplitude envelope of the reference. Because the duration of the reference pulse is much shorter than the duration of the pulse at the output of the fiber,  $E_{out}(x, y, t)$ , it can be written that  $a_{ref}(x, y, t) \approx \tilde{a}_{ref}(x, y) \cdot \delta(t)$ . Hence, the reference pulse acts as a sampling window in time. By moving the mirror M5 (see Figure 3:4) the reference pulse can be translated in time by a factor  $\tau$ . The accuracy of our positioning stage leads to a temporal resolution of 0.33 fs. For each delay  $\tau$ , the reference beam samples a different time slice of the output field by capturing a digital hologram, which is recorded on the Camera 1, in an off-axis configuration. For the remainder of the paper, a time-sampled part of the output field at a given delay time will be identified with the time variable  $\tau_1$ , while all other time dependencies will be represented by  $t$ .

The intensity of the recorded digital hologram can be expressed as a superposition of three terms: One DC term and two terms containing the phase information of the field  $E_{out}(x, y, t)$  [23]. The angle between the reference beam and the object beam is adjusted to obtain an adequate separation of the interference terms in the Fourier space. The spatial Fourier transform of the digital hologram is calculated and the interference term, containing the phase information, is spatially filtered. The field power as a function of time is measured by integrating over the whole computed filtered term for each delay  $\tau_1$ , which gives a measure of the time duration of the pulse at the proximal side of the fiber (Figure 3:5 (b)). Then, the inverse Fourier transform of the filtered term is calculated for each delay  $\tau_1$ , leading to a digital reconstruction of the phase and amplitude of the field. Therefore, the time sampled version of the field  $E_{sampled}(x, y, \tau_1)$ , at the plane of Camera 1 is given by,

$$E_{sampled}(x, y, \tau_1) = \sum_{m=M_a}^{m=M_b} a_m(\tau_1) \psi_m(x, y) e^{j\phi_m(x, y, \tau_1)} e^{-j\omega_0 \tau_1}$$

Equation 3:3

where  $M_a$  and  $M_b$  are the first and last sampled modes of the set of modes that arrive within the temporal duration of the reference envelope.

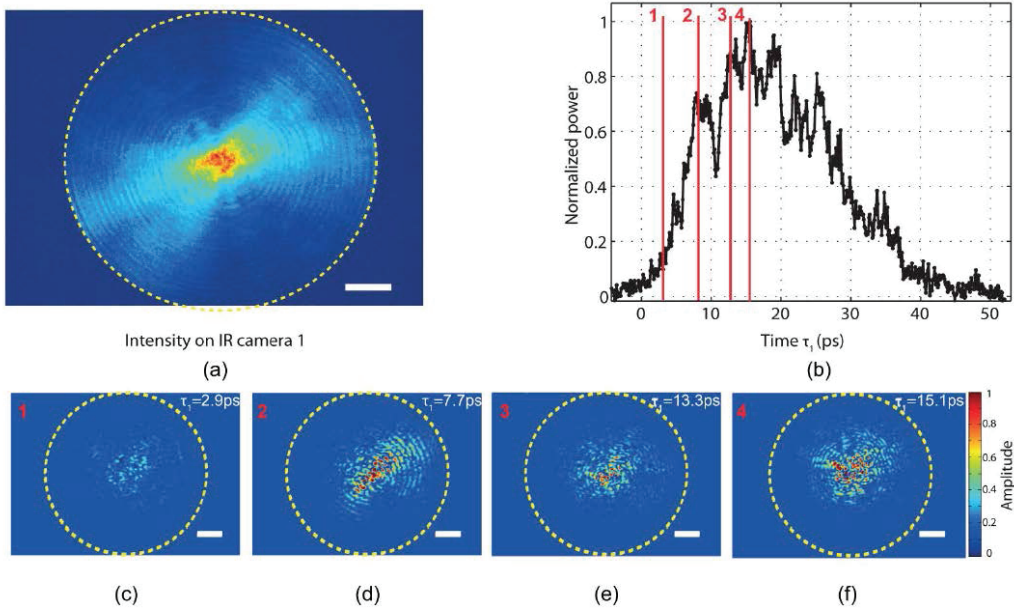


Figure 3:5 Propagation and characterization of an ultrashort pulse through a multimode fiber. (a) Optical intensity as seen on the proximal end (Camera 1) containing the superposition of the excited modes arriving at all times. (b) Normalized optical power of (a) over the whole area of the Camera 1 as a function of time. (c)-(f) Time-gated snapshots of the sampled field (Eq. (3)) taken at times  $\tau_1 = 2.9$  ps,  $\tau_1 = 7.7$  ps,  $\tau_1 = 13.3$  ps, and  $\tau_1 = 15.1$  ps respectively. Scale bars are  $25 \mu\text{m}$ . Dashed circles indicate the edge of the multimode fiber core.

With a reference beam of temporal duration of 440 fs, the number of modes sampled by the reference is  $M_b - M_a = 42$  (one polarization). This value is obtained by taking into account the mode velocity of the M modes that propagate through the multimode fiber [24]. From this mode velocity, we calculated the arrival time as a function of mode index, which follows a linear behavior. Hence, the modes are uniformly distributed in time. For an arrival time interval

corresponding to the duration of the reference pulse, the number of sampled modes is always the same even if the reference is shifted to smaller or larger arrival times. Figure 3:5 (c)-(f) shows the time-gated amplitude of the field  $E_{\text{sampled}}(x, y, \tau_1)$  at time delays  $\tau_1=2.9$  ps,  $\tau_1=7.7$  ps,  $\tau_1=13.3$  ps, and  $\tau_1=15.1$  ps respectively.

### 3.2.3 Delivery of focused pulses (reconstruction)

The recorded digital holograms of each one of the sampled versions of the fields shown in Figure 3:5 (c-f) can be reconstructed in an off-axis holographic arrangement as explained in Chapter 2. The reconstructed field counterpropagates through the fiber generating a reconstruction of the excitation spot at the distal side. Experimentally, the computed phase of each sampled field is conjugated and loaded sequentially onto a Spatial Light Modulator (Holoeye PLUTO-TELCO-013-C, phase only SLM, 1920x1080 pixels, phase range from 0 to  $2\pi$ , pixel pitch 8  $\mu\text{m}$ ). The reference beam (see Figure 3:4) illuminates the SLM. The back-propagating field retraces its way through the multimode fiber to the distal end. Note that in this reconstruction step, the object beam is blocked.

The spatial amplitudes of the phase conjugated spots, measured with the infrared Camera 2, are shown in Fig. 3(a)-(d), and their temporal profiles in Fig. 3(e) for different phase conjugated fields corresponding to digital holograms recorded at time delays  $\tau_1$  equal to 2.9 ps, 7.7 ps, 13.3 ps, and 15.1 ps. The temporal profiles were obtained by second order interferometric autocorrelation averaged within the spatial FWHM of the light spot. The measured pulse widths are 0.50 ps, 0.80 ps, 1.11 ps and 0.54 ps respectively. The spot sizes, measured as the FWHM of the intensity line profile passing through the center of the intensity focus, are 10.5  $\mu\text{m}$ , 6.3  $\mu\text{m}$ , 5.7  $\mu\text{m}$  and 6  $\mu\text{m}$  respectively.

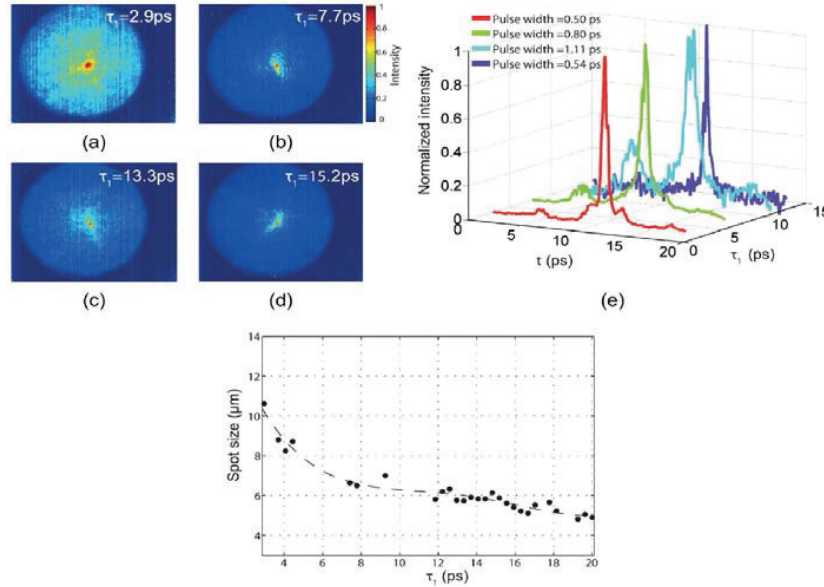


Figure 3:6 Spatio-temporal characterization of the reconstructed phase conjugated spot. (a)-(d) intensity of the spatial profile measured with Camera 2 and (e) temporal profile of the phase conjugated spots generated from the reconstructed holograms of Fig. 2(c)-(f) taken at time delays  $\tau_1$  equal to 2.9 ps, 7.7 ps, 13.3 ps, and 15.1 ps respectively.  $\tau_1$  demotes the time at which the hologram was recorded and  $t$  is the time dependence of the intensity autocorrelation trace of the phase conjugated spot. (f) Size of the phase conjugated spot as a function of  $\tau_1$ . Points represent experimental data and the solid curve a polynomial fit.



The evolution of the spot size of the phase conjugated spots as a function of the time at which the hologram was recorded  $\tau_1$  is shown in Figure 3:6(f). During the selective DPC process, the original field is reconstructed with only 42 time-sampled modes (out of the 10'000 modes supported by the fiber). Hence, the original spot cannot be reconstructed with high fidelity. We observe that phase conjugation of higher order modes, corresponding to a larger delay  $\tau_1$ , produces a smaller phase conjugated spot due to the fact that each mode group of a certain velocity is associated, in a guided-ray approach, to a respective bouncing angle in the fiber. Hence, each group of modes is linked to an effective numerical aperture which is inversely proportional to the lateral and axial spot size that can be generated with that group of modes. The highest peak intensity measured in our experiment was 125 MW/cm<sup>2</sup> realized with a spot waist of 5.1  $\mu\text{m}$  corresponding to the excitation of high order modes sampled at a delay  $\tau_1=20$  ps.

The change in the spot size of the focused spot as a function of the time delay when the hologram was recorded can also be noticed in the Fourier transform of the digital hologram. Figure 3:7 clearly shows this. For this experiment a fiber bundle of 17'000 thousand cores was used. At the wavelength of the source, 1550 nm, the fiber bundle acts as a multimode fiber rather than as a fiber bundle. This gives rise to intensity distributions larger than the size of the cores rather than an exclusive illumination of the cores of the bundle as can be seen in Figure 3:7. The time-gated speckle corresponding to a larger numerical aperture (smaller speckle grains) covers a larger disc in the diffractive orders than the disc corresponding to a lower numerical aperture. In terms of group velocities, low order modes, associated with a lower numerical aperture travel close to the center of the fiber, in a light ray tracing approximation, at lower angles, traversing a smaller distance in the fiber because they are not bouncing as much as higher order modes. Therefore, they arrive faster to the other side of the fiber and produce larger speckle spots.

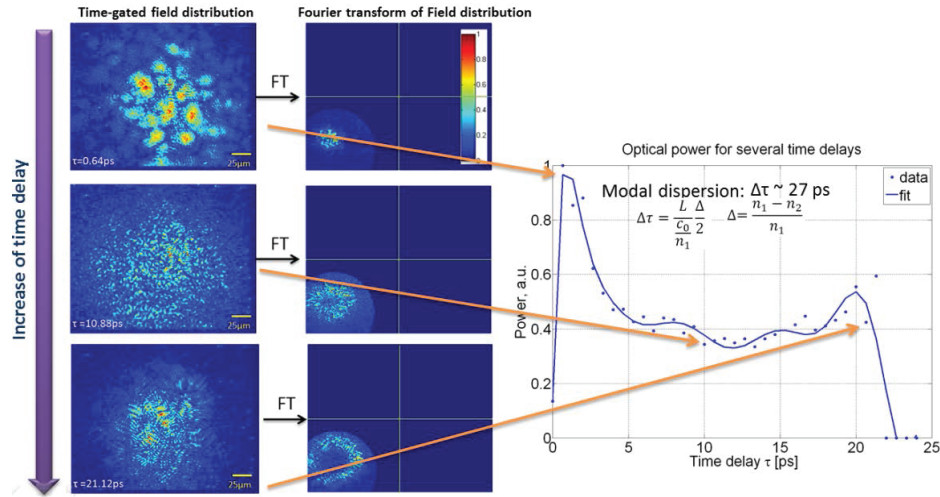


Figure 3:7 Reconstructed amplitude and spectrum of the time gated fields. Gating occurs at time delays equal to 0.64, 10.88, and 21.12 ps. (Left) Reconstructed amplitude of the time-gated field. (Center) Fourier transform of the digital hologram (only the first order term is shown). (Right) Optical power at different time delays.

Each mode of the counterpropagated field also suffers from material dispersion as it propagates in the fiber. This means that individual spectral components of each mode travels at different velocities, causing an additional broadening albeit smaller than caused by modal dispersion. Material dispersion could be compensated by pre-chirping the pulse with an adequate amount of positive dispersion. However, this was not implemented in these experiments in this chapter. In the next chapter, in which the method of light focusing through the MMF is employed to acquire two-photon images, group velocity dispersion i.e material dispersion, arising due to the natural wavelength dependence of the refractive index in the material, is compensated using a pair of prisms.

There are three main parameters of the phase conjugated spot that vary depending on the counterpropagated set of modes. These parameters are 1. Spatial enhancement, defined as the ratio of the maximum intensity of the phase conjugated field to the average background intensity integrated over all times and 2. Spot area, which is the area of the spatial full width at half maximum FWHM of the phase conjugated spot, 3. Temporal duration, defined as the temporal FWHM of the phase conjugated spot.

For efficient non-linear imaging such as two-photon imaging through a multimode optical fiber, the spot with the highest peak intensity is required. We define the peak intensity of the phase-conjugated spot as:

$$I_{peak} = \frac{P_{ave} \left(\frac{w_s}{2}\right)^2 \eta}{R_r \Delta t}$$

Equation 3:4

Where  $P_{ave}$  is the average measured power of the phase conjugated field (both spot plus background field) at the distal end,  $R_r$  is the repetition rate of the pulsed laser source (40MHz),  $w_s$  is the waist of the phase conjugated spot,  $a$  is the radius of the fiber core,  $\eta$  is the intensity enhancement and  $\Delta t$  is the pulse length.

The spatial profile and temporal duration of the phase-conjugated spot depend strongly on the set of modes reconstructed to generate it. Higher order modes (slow modes) have a smaller propagation constant  $\beta$  than low order modes (fast modes). High order modes in an optical fiber are associated with a higher numerical aperture than lower order modes. Thus, the spot size of the phase conjugated spot is expected to decrease with higher mode selection, as experimentally demonstrated in Figure 3:6 (ac). Therefore there exist an optimal set of modes for which the peak intensity can be maximized.

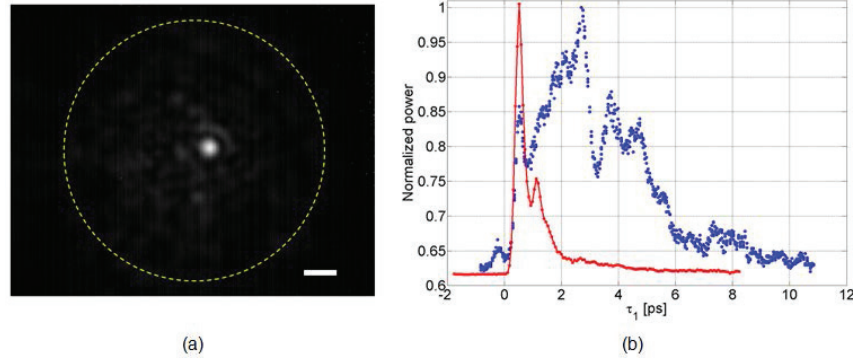


Figure 3:8 Example of a phase conjugated spot using the proposed selective mode launching process. (a) Intensity of the phase conjugated spot generated at the distal end as seen on camera 2. (b) Temporal profile (coherence length) comparison with (red curve) and without (blue curve) using selective mode launching. The temporal coherence of the phase conjugated spot is 515fs. The temporal coherence of the pulse without using wavefront control is 5ps. Scale bars are 30 $\mu$ m. Dashed circles indicate the edge of the core of the multimode fiber.

### 3.3 Temporal characterization of the delivered focused pulses

In order to obtain insights into the spatial distribution of the pulse duration around the phase conjugated spot at the distal end of the fiber, we use a silicon-based camera (Camera 3) sensitive to half the excitation wavelength to spatially resolve a second order interferometric autocorrelation. This is performed by introducing, on the reference arm, two time-delayed replicas with the Michelson interferometer shown in Figure 3:4. The two paths are aligned by ensuring that the speckle pattern on Camera 2 does not change when the delay is varied. The nonlinearity required for the measurement is given by the two-photon absorption of silicon of the 1550 nm intensity. The intensity of the interferometric autocorrelation trace is measured for each camera pixel and for each position  $\tau$  of the interferometer. This means that for each pixel, the intensity of Equation 3:5 is calculated in the experiment. The temporal duration of the phase conjugated field imaged on the Camera 3 is calculated at each pixel assuming a Gaussian pulse shape.

$$I(\tau) = \int_{-\infty}^{+\infty} |[\mathbf{E}(t) + \mathbf{E}(t - \tau)]|^2 dt$$

Equation 3:5

Figure 3:9 provides a comparison of the 2D intensity and pulse duration for the case when 1. The excitation comprises a large number of fiber modes (Figure 3:9 (a), (c)) and 2. The excitation comprises a selected number of modes (Figure 3:9 (b), (d)) using the DPC method proposed. Figure 3:9 (a) shows the intensity (measured with infrared camera 2) at the distal side of the multimode fiber generated by presenting on the SLM a set of plane waves propagating in all directions within the acceptance angle of the multimode fiber, hence exciting a large number of fiber modes.

Figure 3:9 (b) shows the intensity (measured with infrared camera 2) on the distal side when a group of modes is counter-propagated using the proposed DPC method. The ratio of the peak intensity to the average background is 16. This implies that the number of phase conjugated

modes is enough to generate a focused spot 16 times more intense than the background intensity. The size of the phase conjugated spot is  $7\ \mu\text{m}$ .

Figure 3:9 (c) and (d) show the map of temporal duration corresponding to Figure 3:9 (a) and (b) respectively. The average temporal duration when all fiber modes are excited is 15.2 ps (Figure 3:9 (c)), which is large because modal dispersion is present. For the DPC case (Figure 3:9 (d)), temporal broadening by modal dispersion is highly suppressed, and there is a short temporal duration of 500 fs only at the location of the DPC focus. Around the focus, the temporal duration is broad (on average 10 ps) due to undesired excitation of other modes, which are subject to modal dispersion. However, these modes carry much less power (only 6% of the power of the focus) and are less intense than the spatial focus. Figure 3:9 (e) shows the comparison between the average temporal duration obtained when many fiber modes are excited (black curve) and when DPC is used (blue curve). The DPC method significantly reduces the temporal distortions of modal dispersion. The broadening from the original pulse (440 fs) to the delivered pulse using DPC (500 fs) is due to material dispersion. Both pulses shown in Figure 3:9 (e) contain the same energy, but the one with reduced modal dispersion has a larger intensity, which is enough to produce two-photon phenomena as shown Figure 3:10.

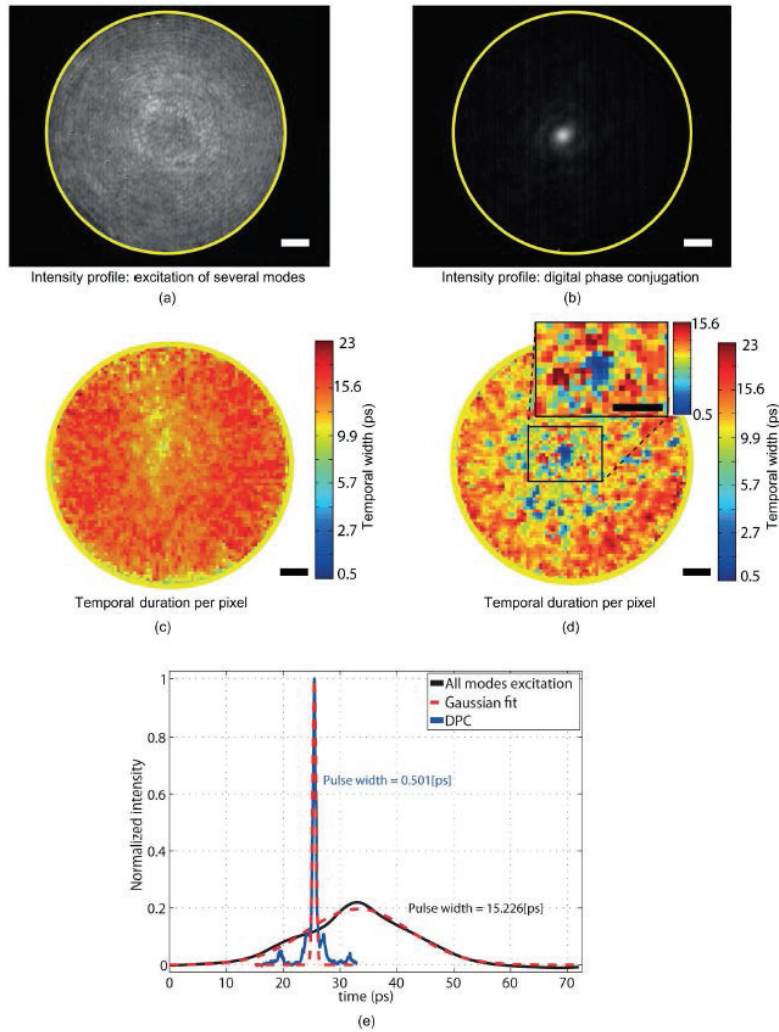


Figure 3:9 Comparison between the excitation of a large number of modes and the selective DPC method. (a) Intensity when many fiber modes are excited. (b) Intensity of a phase conjugated spot generated using DPC. The size of the spot is  $7\ \mu\text{m}$  and is 16 times more intense than the background. (c) and (d) are the spatio-temporal maps of pulse duration when many fiber modes are excited and when DPC is performed respectively. (e) Envelope of the second order autocorrelation trace of the delivered pulse for the excitation of many fiber modes (black curve, averaged over the camera area) and for the DPC case (blue curve, averaged over the FWHM of the spot size). Dashed red lines are their respective Gaussian fit. The broad pulse (black curve) was scaled to enhance its visibility on the graph. Both pulses possess the same energy. Scale bars are  $25\ \mu\text{m}$ . Yellow circles on (a), (b), (c), and (d) indicate the edge of the core of the multimode fiber.

Figure 3:10(a) shows the two-photon signal as a function of optical intensity of the phase conjugated spot of Figure 3:9(b). The non-linear element is a silicon camera which exhibits two-photon absorption at half the wavelength ( $775\ \text{nm}$ ) of the  $1550\ \text{nm}$  excitation. The signal exhibits a quadratic dependence as expected from a two-photon process. In this measurement, the absolute average power of the DPC spot was increased from  $.04\ \text{mW}$  to  $4\ \text{mW}$ . Figure 3:10 (b) shows the two-photon phase conjugated spot measured with the visible camera. Two-photon absorption suppresses the background intensity, leading to an effective two-photon spot 270 times more intense than its surrounding background. The size of the spot is  $5\ \mu\text{m}$ , which is smaller than the  $7\ \mu\text{m}$  of the infrared spot shown Figure 3:9(b) because two-photon absorption occurs in a smaller lateral and axial volume than single photon absorption. To be precise, the spot size of the area where two-photon absorption occurs is  $\sqrt{2}$  times smaller than the area of the original excitation.

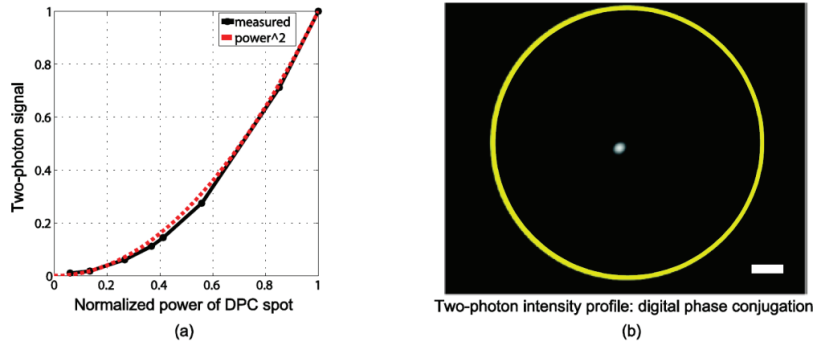


Figure 3:10 Two-photon measurement of the phase conjugated spot. (a) Two-photon signal versus normalized power produced by the phase conjugated spot measured on a silicon-based detector (Camera 3 in the setup). Measured (black curve) and theoretical curve (dashed red curve). (b) Two-photon phase conjugated spot. The spot size is  $5\ \mu\text{m}$ . The contrast ratio between the maximum intensity to the average background is 270.

### 3.4 Spatial scanning and temporal multiplexing of the focused pulses

#### 3.4.1 Light scanning through the multimode fiber

Following the steps of mode selection explained above, the procedure can be repeated to record a digital hologram, at a fixed chosen position of the sampling reference, for each one of the targeted locations of the excitation spot at the distal end of the fiber. After this first calibration step we can sequentially generate by DPC a focused pulse at each one of the respective locations of the original excitation. The second part of this process can be considered as a digital scan of the phase conjugated spot. The result is shown in Figure 3:11, which presents three spot scanning locations captured on Camera 3. The lateral distance between two con-

secutive spots is  $50\text{ }\mu\text{m}$ . The waists of the generated two-photon spots are  $5.6\text{ }\mu\text{m}$ ,  $5.4\text{ }\mu\text{m}$  and  $5.9\text{ }\mu\text{m}$  respectively. The intensity of the spot is 48, 135 and 45 times more intense than the background, respectively.

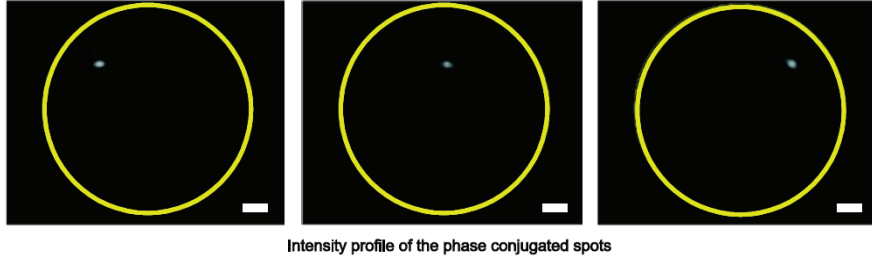


Figure 3:11 Scanning of the phase conjugated focus. The pulsed intensity focused can be generated at different locations. Scale bars are  $25\text{ }\mu\text{m}$ .

The calibration step can be efficiently automated using a scanning galvanometer mirror system. Hence, the time limitation of the calibration is only restricted by the frame rate of the camera used to record the digital holograms. The scanning step is limited by the frame rate of the SLM ( $20\text{ Hz}$  in our case).

### 3.4.2 Temporal multiplexing through the multimode fiber

In addition to the generation of a single phase conjugated spot, this method allows the generation of a pair (or more) time delayed spots. This is achieved by reconstructing the superposition of two different groups of modes. The phase pattern on the SLM is simply the phase of the sum of the waves each one of them with a phase equal to the respective phase required to reconstruct each one of the sampled group of modes individually. Each group of modes counter-propagates at its own group velocity, arriving to the distal side at two different times, generating two consecutive pulses as shown in Figure 3:12. This is possible due to the linearity and time invariance of the propagation of light through a multimode fiber. The pulse duration of each individual pulse is measured by second order autocorrelation. The envelopes of these traces are shown as first pulse and second pulse in Figure 3:12. The temporal separation between the pulses is  $3.7\text{ ps}$ . Their pulse durations are  $500\text{ fs}$  and  $800\text{ fs}$  respectively. This experiment demonstrates that it is possible to generate two consecutive high intensity focused pulses at the output of a multimode fiber from a single input pulse.

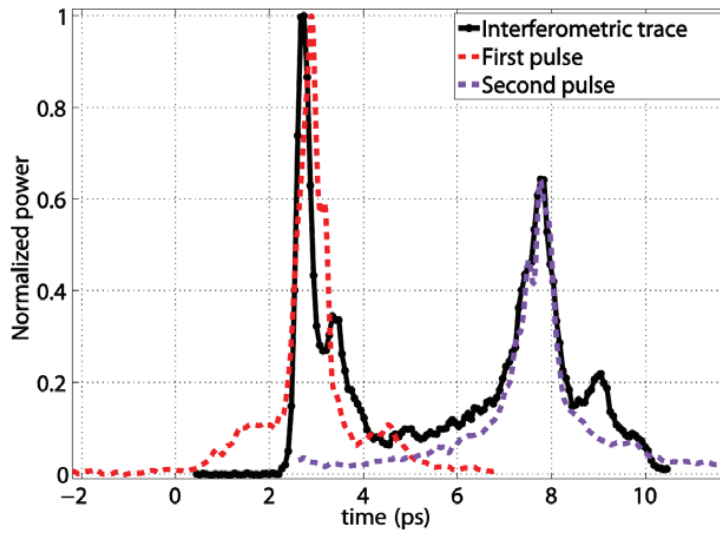


Figure 3:12 Generation of two time multiplexed phase conjugated spots. The time envelope is measured by time-gated interferometry (solid curve). The phase conjugated pulses are centered at  $t=2.9$  ps and  $t=7.7$  ps respectively. Dashed curves: second order autocorrelation envelopes of phase conjugated pulses 1 and 2. Their pulse widths are 500 fs and 800 fs respectively.

### 3.4.3 Spatial multiplexing through the multimode waveguide

Similarly to the previous case, the simultaneous reconstruction of the phase of a wave that results from the addition of two plane waves, each one of them corresponding to the phase conjugated version of the field that generates a single spot through the fiber, gives rise to two and in principle any number of simultaneous optical pulses through the fiber. The results are presented in Figure 3:13 Generation of two simultaneous spots through fiber bundles. through fiber bundles. (a) 6'000 cores fiber. FWHM spot size= $4.3\mu\text{m}$ .  $\eta=139$ . (b) 17'000 cores fiber. FWHM spot size= $4.3\mu\text{m}$ ,  $\eta=102$ . c) 6'000 cores fiber.  $\eta=135$ , 119. d) 17'000 cores fiber.  $\eta=73$ ..

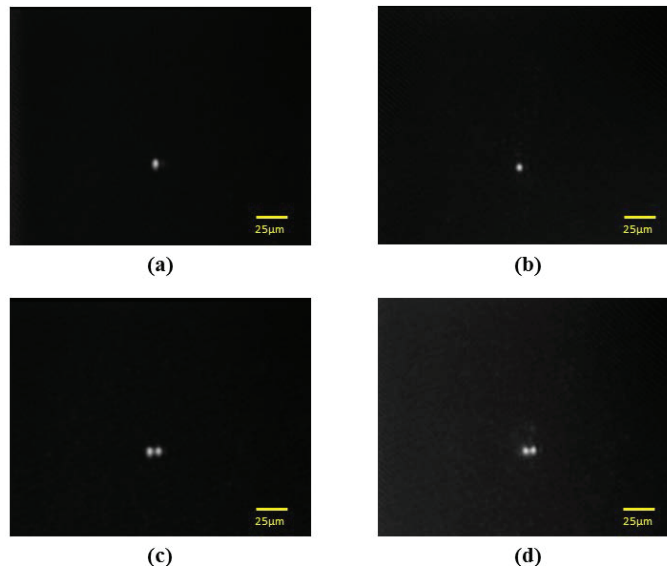




Figure 3:13 Generation of two simultaneous spots through fiber bundles. through fiber bundles. (a) 6'000 cores fiber. FWHM spot size=4.3 $\mu$ m.  $\eta$ =139. (b) 17'000 cores fiber. FWHM spot size=4.3 $\mu$ m,  $\eta$ =102. c) 6'000 cores fiber.  $\eta$ =135, 119. d) 17'000 cores fiber.  $\eta$ =73.

### 3.5 Discussion and conclusions

This chapter presented the first experimental demonstration of simultaneous spatial and temporal focusing of ultrashort pulses through a multimode fiber using time-gated interferometry followed by digital phase conjugation. The focused pulse can be generated at different locations on the distal side of the fiber. Since the power of the phase-conjugated field is spatially spread on various excited modes, our approach does not introduce nonlinear effects.

We demonstrated how phase conjugation of modes with the same propagation constant reduces temporal broadening due to modal dispersion in the fiber by a factor of 30. Thus, the pulse preserves its short temporal profile as it propagates. The limited observed temporal spreading (from the initial 440 fs to the distal 500 fs) arises due to material dispersion. In our experiments no pre-chirp was applied to the beam used for the reconstruction of the time-sampled modes. However, if the pulse is pre-chirped with the right chirp parameter, this temporal spreading could be suppressed.

The ability to focus light through multimode fibers is directly linked to the number of phase conjugated modes. Therefore, the sharpness of the phase conjugated spot could be enhanced by using a multimode fiber with reduced modal dispersion such as a graded-index fiber or by using a shorter fiber. We estimate that using a graded index fiber and pre-chirping to correct for material dispersion, the peak intensity of the phase conjugated pulse could be increased two orders of magnitude compared to the step-index multimode fiber case presented here. In fact, by using a graded-index multimode fiber of diameter equal to 200  $\mu$ m, we would be able to sample and phase conjugate a total of 2200 modes instead of the 42 we have shown, which would significantly increase the contrast of the phase conjugated spot by a factor of 50.

We also demonstrated how the intrinsic modal dispersion of the multimode fiber can be used to generate two temporally separated pulses from a single pulse. This was accomplished by simultaneous phase conjugation of two set of modes with different group velocities. Each set of modes leads to a single pulse centered at a desired time. In principle this can be extended to a larger number of contiguous pulses.

We have shown that the intensity of the phase conjugated spot is enough to produce two-photon absorption in a silicon-based detector. Therefore, our technique opens the possibility of acquiring two-photon images through commercial multimode optical fibers. Once the system is calibrated, a two-photon fluorescence image of a sample placed in the distal side of the fiber can be obtained by scanning the DPC spot over the sample and collecting the fluorescent signal through the same fiber.

### 3.6 References

1. S Bianchi and R. Di Leonardo, "A multimode fiber probe for holographic micromanipulation and microscopy," *Lab Chip* 12, 635–639 (2012).



2. T Čižmár. & K. Dholakia, "Exploiting multimode waveguides for pure fibre-based imaging," *Nat. Commun.* 3, 1027 (2012).
3. Y. Choi, C. Yoon, M. Kim, T. D. Yang, C. Fang-Yen, R. R. Dasari, K. J. Lee, W. Choi, "Scanner-free and wide-field endoscopic imaging by using a single multimode optical fiber," *Phys. Rev. Lett.* 109(20), 203901 (2012).
4. Papadopoulos, I. N., Farahi, S., Moser, C. & Psaltis, D. "High-resolution, lensless endoscope based on digital scanning through a multimode optical fiber," *Biomed. Opt. Express* 4, 260–270 (2013).
5. N. Bozinovic, Y. Yue, Y. Ren, M. Tur, P. Kristensen, H. Huang, A. E. Willner, and S. Ramachandran, "Terabit-Scale Orbital Angular Momentum Mode Division Multiplexing in Fibers," *Science* 340, 1545–1548 (2013).
6. D. J. Richardson, J. M. Fini, and L. E. Nelson, "Space-division multiplexing in optical fibers," *Nature Photon.* 7, 354–362 (2013).
7. A. Yariv, D. Fekete, and D. M. Pepper, "Compensation for channel dispersion by nonlinear optical phase conjugation," *Opt. Lett.* 4, 52 (1979).
8. M. Tsang, D. Psaltis, F. Omenetto, "Reverse propagation of femtosecond pulses in optical fibers," *Opt. Lett.* 28, 1873-1875 (2003).
9. F. Omenetto, B. Luce, and A. Taylor, "Genetic algorithm pulse shaping for optimum femtosecond propagation in optical fibers," *J. Opt. Soc. Am. B* 16, 2005-2009 (1999).
10. X. Shen, J. M. Kahn and M. A. Horowitz, "Compensation for multimode fiber dispersion by adaptive optics," *Opt. Lett.* 30, 2985–2987 (2005).
11. H. Itoh, T. Urakami, S. Aoshima and Y. Tsuchiya, "Femtosecond pulse delivery through long multimode fiber using adaptive pulse synthesis," *Japanese Journal of Applied Physics* 45, 5761–5763 (2006).
12. A. A. Yariv, "Three-dimensional pictorial transmission in optical fibers," *Appl. Phys. Lett.* 28, 88–89 (1976).
13. P. Forman, F. Jahoda, and B. Mason, "Multimode fiber interferometry with and without phase conjugation," *Appl. Opt.* 30, 1629-1632 (1991).
14. I. McMichael, P. Yeh, and P. Beckwith, "Correction of polarization and modal scrambling in multimode fibers by phase conjugation," *Opt. Lett.* 12, 507-509 (1987).
15. R. Di Leonardo and S. Bianchi, "Hologram transmission through multi-mode optical fibers," *Opt. Express* 19, 247-254 (2011).
16. T. Čižmár and K. Dholakia, "Shaping the light transmission through a multimode optical fibre: complex transformation analysis and applications in biophotonics," *Opt. Express* 19, 18871-18884 (2011).
17. J. Carpenter, B. Eggleton, and J. Schröder, "110x110 optical mode transfer matrix inversion," *Opt. Express* 22, 96-101 (2014).
18. I. Papadopoulos, S. Farahi, C. Moser, and D. Psaltis, "Focusing and scanning light through a multimode optical fiber using digital phase conjugation," *Opt. Express* 20, 10583-10590 (2012).
19. J. Aulbach, B. Gjonaj, P. M. Johnson, A. P. Mosk, and A. Lagendijk, "Control of Light Transmission through Opaque Scattering Media in Space and Time," *Phys. Rev. Lett.* 106, 103901 (2011).
20. O. Katz, E. Small, Y. Bromberg, & Y Silberberg, "Focusing and compression of ultra-short pulses through scattering media," *Nature Photon.* 5, 372–377 (2011).

21. E. Andresen, G. Bouwmans, S. Monneret, and H. Rigneault, "Two-photon lensless endoscope," *Opt. Express* 21, 20713-20721 (2013).
22. R. Rokitski and S. Fainman, "Propagation of ultrashort pulses in multimode fiber in space and time," *Opt. Express* 11, 1497-1502 (2003).
23. J. Pomarico, U. Schnars, H. J. Hartmann and W. Jüptner, "Digital recording and numerical reconstruction of holograms: a new method for displaying light in flight," *Appl. Opt.* 34, 8095–8099 (1995).
24. B. E. A. Saleh and M. C. Teich, *Fundamentals of Photonics*, 2nd ed. (Wiley, 2007).

## Chapter 4 The multimode fiber two-photon endoscope

This chapter describes how a multimode optical fiber can be used as an ultra-thin two-photon endoscope. The theory, a working prototype and results are presented. To our knowledge, this is the first demonstration of high-resolution three-dimensional imaging using two-photon fluorescence through a multimode fiber.

The vast number of propagating solutions to the wave equation in multimode optical fibers represents a larger information capacity than that available in a group of single mode fibers or in fiber bundles. Therefore, in the field of imaging, multimode fibers potentially permits the transmission of images with higher resolution. However, image transmission through multimode fibers is not direct as in the fiber bundle case, in which each of the fiber cores can relay a portion of the distal image. In multimode fibers, a distribution of intensity is scrambled by the propagating modes, leading on the other side to a speckle-like pattern that doesn't resembles the initial distribution.

This chapter presents two-photon excitation imaging of fluorescent beads and ex-vivo biological samples through a multimode optical fiber. We show that our method maintains the advantages of two-photon excitation microscopy compared to single-photon excitation such as reduced photo-bleaching, deeper penetration depth and sectioning capability. Our method is based on time-gated digital phase conjugation, which allows the generation of focused pulses on the other side of a multimode fiber. To acquire an image, the focused femtosecond pulse is scanned in a three-dimensional mesh, producing two-photon excitation on each spatial location of the sample. By collecting the fluorescence through the fiber, a 3D two-photon image is reconstructed.

The endoscopic system presented in this article is capable of acquiring 3D images using two-photon excitation through a 20 cm long multimode optical fiber (MMF) of 350  $\mu\text{m}$  diameter. We demonstrate depth sectioning by scanning the focused pulse in a 3D volume over a sample made of fluorescent beads suspended in a transparent polymer. The achieved lateral resolution is 1  $\mu\text{m}$  and the axial resolution is 15  $\mu\text{m}$ . Scanning and imaging is demonstrated over an 80x80  $\mu\text{m}$  field of view. Additionally, in the end of this chapter, two-photon imaging of ex-vivo tissue is also shown.

Some of the results shown in this chapter were published in the Optics Express journal as:

E. E. Morales-Delgado, D. Psaltis, and C. Moser, "*Two-photon imaging through a multimode fiber*," Opt Express 23, 32158-32170 (2015).

#### 4.1 Introduction to optical fiber-based endoscopy

Multiphoton microscopy is an imaging technique that allows optical sectioning deep within thick samples. It presents an enhanced image contrast and reduced photo-damage to the sample in comparison to single photon microscopy. For some applications such as in-vivo imaging of individual cells inside hollow cavities in a minimally invasive way, an ultra-thin multiphoton endoscope is necessary.

An endoscope is a device that allows the visualization of the interior of organs or cavities inside of the body. Conventionally, multiphoton endoscopy has been accomplished using graded index probes, double clad fibers or fiber bundles. In graded index probes, which consist on an objective lens attached to a relay lens, total internal reflection occurs gradually provoking a travelling of light rays in a sinusoidal profile [1]. A complete cycle of the sinusoidal pattern is called a pitch length. However, light rays present optical aberrations at a pitch longer than 0.5. [1], limiting the usability to short rigid probes ( $\sim 30$  mm length). Additionally, at off-axis locations, resolution decreases due to the graded index profile. In the double clad fiber endoscopes, the illumination is delivered through the single mode core. To focus light over the sample, a lens is attached to the distal tip of the fiber. A mechanism is required at the distal tip of the endoscope to scan the illumination over the field of view. The presence of such mechanism limits the miniaturization of the probe. The produced two-photon fluorescence is collected through the multimodal cladding [1]. A very commonly used endoscopic system for clinical applications is based on multi-core fibers (MCFs). Their main advantage are the following: MCFs are thin (0.3 mm for 6,000 cores), and the section entering the body is passive, i.e. does not contain active electronic components. However, MCF transmits pixelated images due to the space between the cores (3-5  $\mu\text{m}$ ), which limits the resolution of the system to the core to core spacing distance, which is several micrometers [1-8]. A graphical representation of such devices is shown in Figure 4:1.

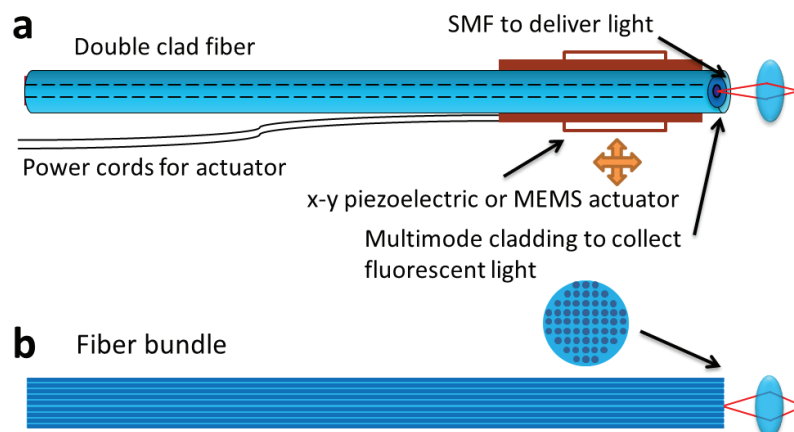


Figure 4:1 Conventional fiber endoscopes. (a) Double clad fiber endoscope. (b) Multi-core or fiber bundle endoscope.

Wavefront shaping methods using MCFs and multimode fibers (MMFs) have been able to effectively “de-pixelate” images to obtain diffraction limited resolution. This has been demonstrated in experiments similar to those to focusing light through scattering media [9-13]. Wavefront shaping methods include phase conjugation in the digital or analog version [14-19], the measurement of the transmission matrix to provide wide field imaging [20-23] and iterative algorithms that optimize for the brightest intensity at a given location [24-30]. However, these imaging approaches have been demonstrated using monochromatic light sources. Thus, for fluorescence imaging, only one-photon excitation was shown.

Two-photon excited fluorescence (TPEF) requires high peak power light sources, which is typically achieved with pulsed light sources with pulse lengths in the order of hundreds of femtoseconds. Regarding two-photon endoscopy, Andersen et al have demonstrated two-photon imaging through a custom MCF with 169 cores [31] using wavefront shaping. In chapter 3 we have shown scanning and focusing of pulses in a step index MMF while maintaining a pulse duration of 500 fs through 30 cm fiber propagation [32]. In graded index fibers, spatial focusing of optical pulses has been shown [33]. However, in these previous studies, TPEF imaging through multimode fibers was not demonstrated.

In this chapter we demonstrate high resolution two-photon excitation imaging through a graded-index multimode optical fiber. We use time-gated digital phase conjugation to focus and scan high intensity femtosecond pulses through the fiber [32]. Using a prism pair, the group velocity dispersion (GVD) occurring in the fiber is compensating, allowing the transmission of near Fourier-limited optical pulses of 120 fs pulse length. Sectioned images of fluorescent beads suspended in a PDMS polymer volume are imaged. The high resolution (1 $\mu$ m), small probe diameter (350  $\mu$ m), large collection efficiency, sectioning capability and ultrashort focused pulse delivery of our system opens the possibility for in-vivo minimally invasive multiphoton endoscopy in areas such as the brain, the ear or the eye.

## 4.2 Focusing pulses through the multimode fiber

The experiments were conducted using a Ti:sapphire oscillator shown in Figure 4:2 (Coherent Mira 900; central wavelength  $\lambda_c=800$  nm; spectral width  $\sigma\lambda=10$  nm; pulse width=100 fs; repetition rate 76 MHz). The capability of our method to form a sharp focused pulse through the fiber depends on the number of modes than can be controlled simultaneously [32]. In step-index fibers, the temporal pulse spreading is given by:  $\sigma_\tau \approx L\Delta/(2c_1)$  while in graded-index fibers:  $\sigma_\tau \approx L\Delta^2/(4c_1)$  [34]. Due to their smaller modal temporal-spreading, we selected a graded-index fiber for our experiments. The fiber has a 200  $\mu$ m core diameter, 280  $\mu$ m cladding diameter, 20 cm length, 0.29 NA and supports 26,000 modes at a 800 nm wavelength. The SLM used for time-gated phase conjugation is a Holoeye Pluto, 1920x1080 pixels, phase only.

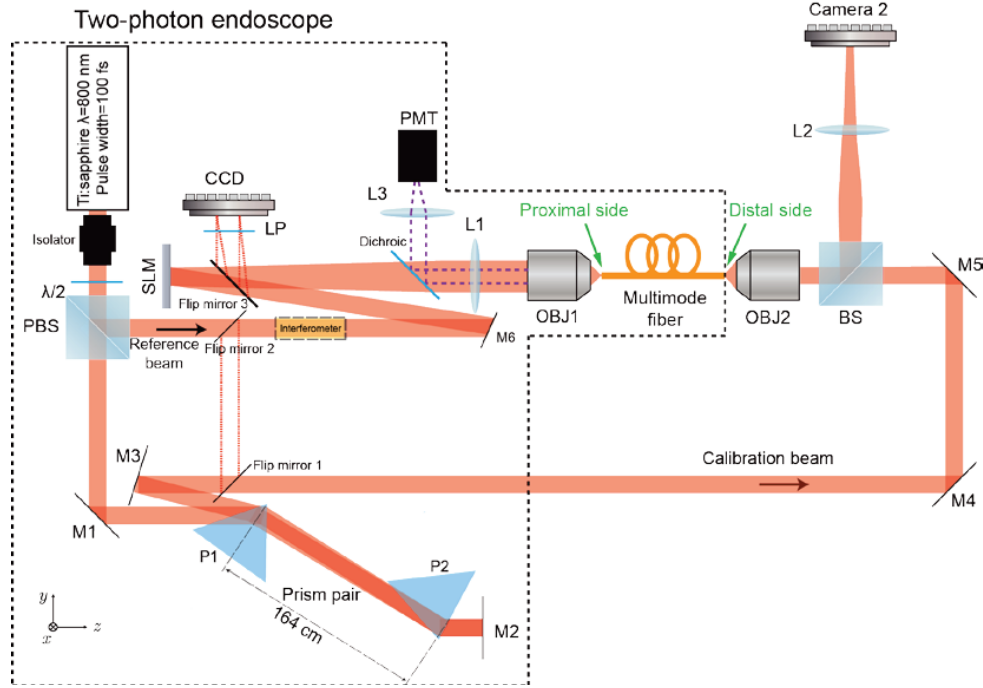


Figure 4:2 Experimental setup for multimode fiber endoscopy.

#### 4.2.1 Calibration

To generate spatially focused pulses through the multimode fiber, we use the method described in the previous chapter, which is time-gated digital phase conjugation. This method requires the following calibration step, which can be followed in Figure 4:2. The 100 fs pulses from a Ti:sapphire laser are stretched out in time by a prism pair separated by 164 cm. This compensates for the group velocity dispersion (GVD) that the pulses suffer as they travel through the fiber. The GVD compensated beam (calibration beam) is then focused in front of the 20 cm length graded index fiber by a 40x microscope objective. We call this the “calibration spot”. As light from the calibration spot enters the MMF it is decomposed into multiple fiber modes, which generate, after propagation to the proximal side of the fiber, a temporally dispersed and spatially scrambled light field. In an off-axis holographic arrangement, a digital hologram of the time-gated light field is recorded on the CCD at the other end of the fiber. The process is repeated at different locations of the calibration spot in a three-dimensional grid. The digital holograms are stored.

In specific, flip mirror 1 and 2 are removed to let the calibration beam pass through the prism pair and couple into the fiber by a 40x microscope objective (OBJ2). The field emerging from the fiber on the proximal side is imaged by a 20x objective (OBJ1) and a 150 mm lens (L1) onto the CCD, where it is interfered by the pulsed reference beam. The pulsed reference can be delayed and is set at the time in which the visibility of the fringes is maximum [32].

#### 4.2.2 Reconstruction

At the reconstruction step, flip mirror 3 is removed allowing the reference to reach the SLM and reconstruct the phase conjugate version of the recorded field. Light counter propagated

through the fiber and is focused on the distal side imaged on Camera 2 by a 200 mm lens (L2). The hologram can be reconstructed with GVD compensation (flip mirrors 1 and 2 in place) and without GVD compensation (flip mirrors 1 and 2 removed).

At the imaging step, the 2PF is collected through the fiber, reflected by a 650 nm short-reflected dichroic mirror, and focused on the PMT by a 35 mm lens (L3). This ensures the collection of most of the spectral emission of the sample, whose maximum fluorescence is centered at 575 nm.

To measure the pulse width of the generated pulses through the fiber we use second order interferometric autocorrelation by introducing two replicas of the pulses on the reference arm using the interferometer shown in Figure 4:2 and Figure 4:3. As a nonlinear element for the second order interferometer, we place a homogeneous sample of PDMS with Rhodamine 6G [35, 36]. The fluorescence is collected through the fiber and measured by the PMT. The background to maximum ratio of the measured second order interferometric traces is 1/8. A *sech*<sup>2</sup> pulse is assumed to calculate the pulse lengths (0.64 times the width of the envelope of the autocorrelation trace). For the pulse width measurement in which wavefront control is not employed, we used an intensity autocorrelator (Carpe APE).

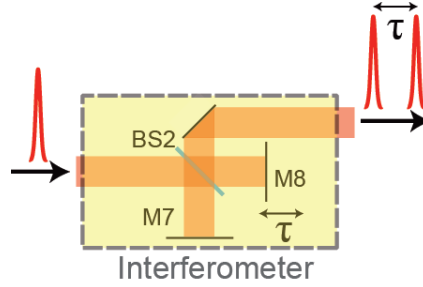


Figure 4:3 Interferometer for pulse width measurement.

To compensate the GVD of the fiber, we use a prism pair in a reflection configuration shown in Figure 4:2. For their high angular dispersion and low loss, we selected prisms made of SF10 of 50x50x50 mm. The separation between the prisms was calculated using the following group delay dispersion (GDD) equation for a prism pair [37]:

$$GDD_{prism\ pair} = \frac{\lambda^3}{2\pi c^2} \left[ 4l \left\{ \left[ \frac{d^2 n}{d\lambda^2} + \left( 2n - \frac{1}{n^3} \right) \left( \frac{dn}{d\lambda} \right)^2 \right] \sin\beta - 2 \left( \frac{dn}{d\lambda} \right)^2 \cos\beta \right\} + 8D \left( \frac{d^2 n}{d\lambda^2} \right) \right]$$

Equation 4:1 – Calculation of the group delay introduced by a prism pair.

Where  $n$  is the refractive index of SF10,  $D$  is the beam diameter and  $\beta = -2 \frac{dn}{d\lambda} \Delta\lambda$ .

The prisms themselves introduce a GDD of the same sign as the GVD introduced by the fiber. To compensate that, the separation between the prisms is larger than that of a prism pair made of infinitesimally small prisms. For GDD adjustment, the second prism was mounted in a 2D stage that moves parallel and perpendicular to the beam connecting prism 1 (P1) and prism 2 (P2). This wave, movement of the stage, or movement of prism 2 in any of the two directions, does not introduce misalignment in the beam exiting the prism pair.

The speed at which the spots can be reconstructed in this approach is limited by the refresh rate of the SLM. Recently, a rotational memory effect of multimode fibers has been reported, which can reduce the calibration and reconstruction time [38]. Fiber bending introduces changes in the propagation of the fiber modes. In our set-up, recalibration is required if the fiber is bent. However, this can be solved by incorporating a bending-compensation method via geometric characterization of fiber bending [20] or by measurement of the proximal speckle of a fiber with a distal reflective coating [39].

## 4.3 Scanning focused pulses through the multimode fiber

### 4.3.1 Spatial characterization

Once the calibration process is completed, the phase conjugated field of each recorded hologram is sequentially reconstructed (the flip mirror is removed) with a spatial light modulator (SLM). The reconstructed field counter propagates through the fiber generating a temporally and spatially sharp focused spot at the distal end. We define the enhancement of the focused pulse as the maximum intensity value in the focused spot divided by the average intensity in the background. As in scattering media, a larger number of controlled modes yields a better focusing capability; hence, greater enhancement [9]. Modes in graded index fibers are confined closer to the core and suffer less modal dispersion than in step-index fibers, which was the case described in chapter 2. However, this results in a drop of the enhancement value when the focus is away from the center of the fiber also called the optical axis. Figure 4:4 shows the experimental results of intensity, enhancement, and spot size of a 40x40 grid of focused pulses generated sequentially 100  $\mu\text{m}$  away from the facet of the fiber. The spots are spaced 2  $\mu\text{m}$  apart. For illustration purposes, Fig. 2(a) shows half of the generated spots (every 4  $\mu\text{m}$ ).

The FWHM spot size of the focused pulses is inversely proportional to the numerical aperture of the fiber. For an observer located on the distal side, the effective numerical aperture of the fiber depends on the position of observation, being maximum at the center [15]. Therefore, the spot size is minimum at focusing locations near the optical axis as shown in Figure 4:4 (c) and Figure 4:4 (e). Simulation shows that the spot size across the fiber diameter in Figure 4:4 (e) is limited by the numerical aperture of the fiber.



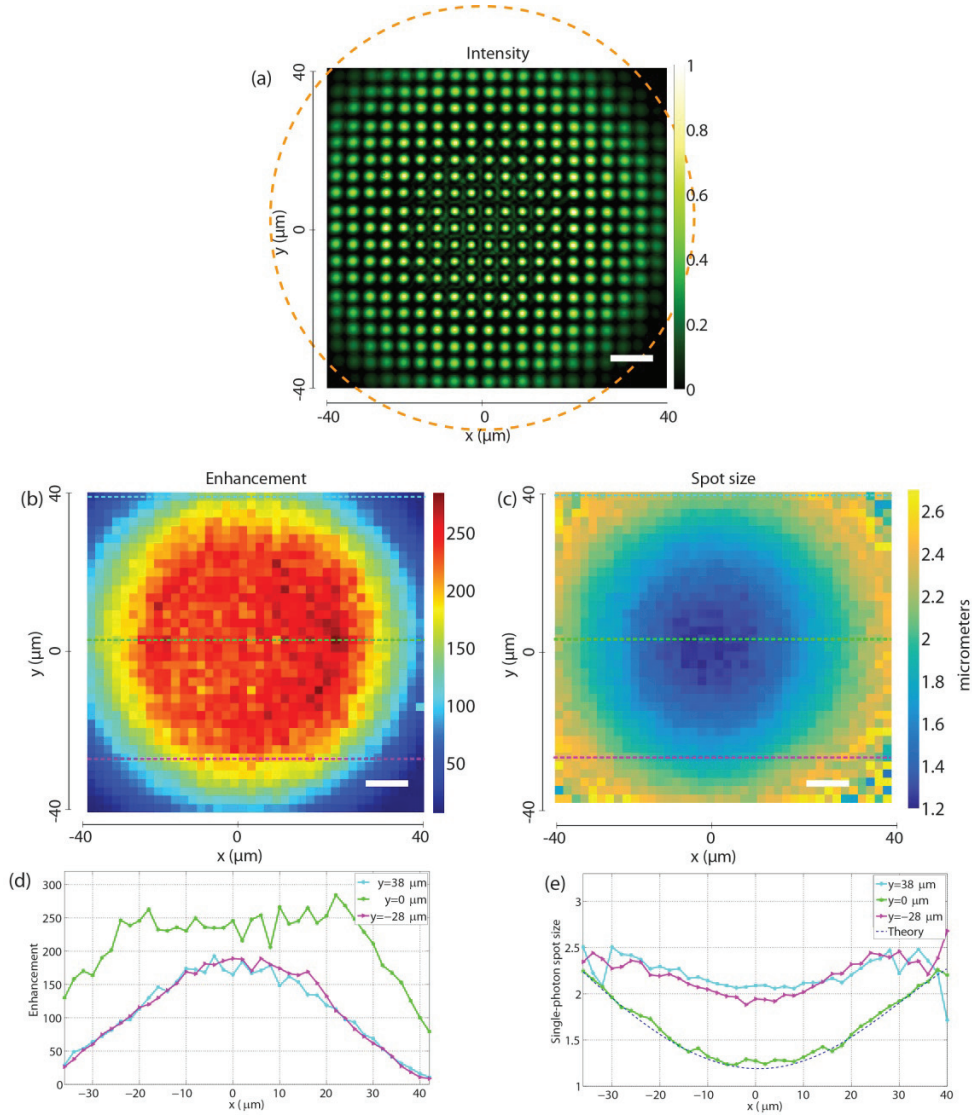


Figure 4:4 Scanning of the focused spot at the fundamental wavelength of 800 nm. (a) Sequential superposition of a focused pulse scanned in a 80x80 μm field of view. Scanning step is 4 μm. (b) Intensity enhancement of the focused pulse as a function of scanning position. (c) FWHM size of the focused pulses as a function of scanning position. (d) Line profile of (b) at the location of the dashed lines. (e) Line profile of (c) at the location of the dashed lines. Scale bars are 10 μm. The dashed orange circle represents the core of the multimode fiber.

#### 4.3.2 Temporal characterization

As demonstrated in [32], the counter-propagation of a time-sampled set of modes excites only fiber modes that travel at approximately the same speed (group velocity). These modes generate a focused pulse which does not suffer from modal dispersion. However, group velocity dispersion GVD still occurs. GVD is a phenomenon by which the spectral components of light travel through a material at different speeds ( $dn/d\lambda \neq 0$ ) which results in broadening of the propagating pulse in time [34].

In our experiments, we compensate for the GVD occurring in the 20 cm length of the fiber by passing the beam through a prism pair (shown in Figure 4:2) separated by 164 cm, which introduces a total group delay of  $-7200 \text{ fs}^2$ . Dispersion compensation enhances the visibility of the fringes at the calibration step, and allows the reconstruction of a 120 fs pulse when used at the reconstruction step, close to the initial 100 fs. In our experimental setup, the compensation of GVD is optional at the reconstruction step.

Figure 4:5 compares the intensity and the pulse length of a line of pulses focused through the fiber when the hologram is reconstructed without GVD compensation and with GVD compensation on the reference. In the absence of GVD compensation, the pulse length is longer, on average 222 fs, due to the temporal broadening produced by GVD in the fiber as shown in Figure 4:5 (b). In contrast, when the pulse is GVD compensated before reconstruction, the spectral dispersion of the excited modes is canceled after propagation through the fiber. All spectral components arrive simultaneously at the distal side of the fiber and produce a short focused pulse, on average 117 fs. A small temporal broadening is observed, from 100 fs to 117 fs which is attributed to the GVD set-up (prism pair in Figure 4:2) where some spectral components angularly dispersed by the first prism are not collected by the second prism. The slight variations in pulse width (a standard deviation of 15 fs for no GVD compensation and 17 fs in the other case) are produced by slightly different propagation paths in the fiber, depending on the location of the generated spot and the specific excited modes. Figures Figure 4:5 (b) and Figure 4:5 (c) show the second order interferometric autocorrelation trace and envelope of pulses focused at the center of the fiber. For the case of no GVD compensation [Figure 4:5 (b)], we can notice an increased non-oscillating intensity at the tails of the pulse, which indicates that the delivered pulse is chirped. For the case of GVD compensation [Figure 4:5 (c)], the effect is less evident because material dispersion in the fiber is compensated. Figure 4:5 (a) shows the intensity autocorrelation trace of a pulse transmitted through the fiber when wavefront control is not being used (light is focused in the optical axis on the proximal side of the fiber and the pulse length is measured at the distal side). In this case, the pulse is broadened due to GVD and modal dispersion, reaching a pulse length of 745 fs from the initial 100 fs.

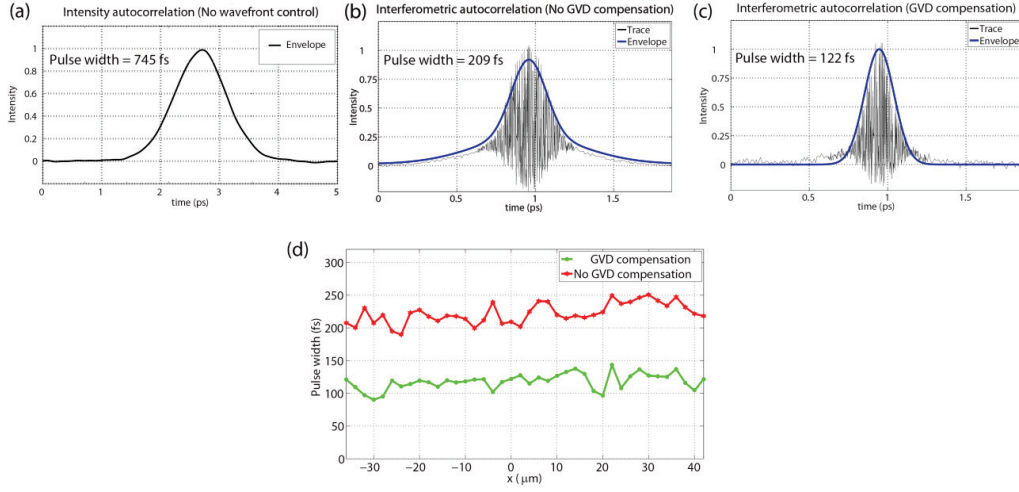


Figure 4:5 Pulse width characterizations. (a) Intensity autocorrelation of the delivered pulse when no wavefront control is used. (b), (c) Sample interferometric autocorrelation traces of the central focused pulses with and without GVD compensation respectively. (d) Pulse width vs position.

Regarding the intensity enhancement, it depends on the position of the focused pulse as shown in Figure 4:6 (b). The enhancement of the generated focused spots shown in Figure 4:6 (a) and is on average 252 and 220 within a  $20\ \mu\text{m}$  radius from the optical axis, for the case of GVD and no GVD compensation, respectively. Hence, the spectral correction achieved by GVD compensation not only reduces pulse broadening, but also enhances the intensity of the focused spot. Since the cross section of the optical fiber is azimuthally symmetric, for the described results, we can characterize the spots scanned only along a line passing through the optical axis at the center of the core without loss of generality. Taking into account a transmittance of 75% through the GVD compensation set-up (prism pair), in our experiments, the signal to noise ratio of the focused spot is enhanced by a factor of 1.6, equivalent to a factor of 2.56 when the spot produces fluorescence on a suitable sample, when GVD is compensated.

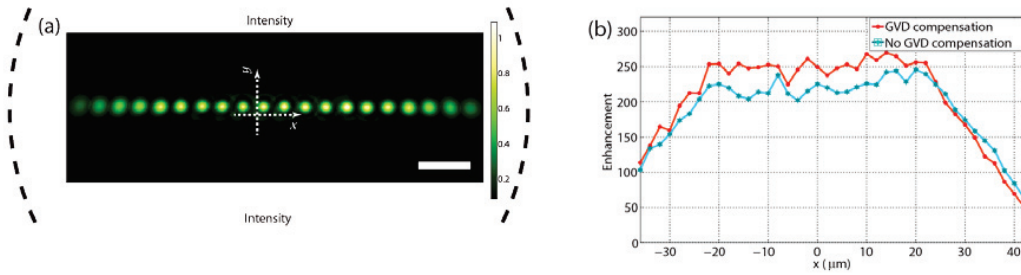


Figure 4:6. Intensity characterization of light focus through the fiber. (a) Line of focused spots. (b) Intensity enhancement of the focused spots shown in (a). Scale bar is  $10\ \mu\text{m}$ .

## 4.4 Imaging through the multimode fiber

### 4.4.1 Two-photon imaging

Two-photon microscopy is an enhanced imaging technique compared to single photon microscopy, which intrinsically allows sectioning in bulk tissue because of the natural suppression of

out-of-focus fluorescence in the two-photon absorption process, resulting in enhanced image contrast and reduced photo-damage to the sample. Additionally, the large spectral separation (close to half) from the excitation central wavelength to the center of the fluorescent emission simplifies the detection of the fluorescent signal and also allows staining with various fluorophores that can target specific structures in the cell. This way, just by changing the detection filter, or changing the excitation wavelength, different cellular structures in tissue can be identified. In single-photon fluorescent this spectral separation is harder to achieve due to the spectral proximity between the excitation and the fluorescent emission. All the advantages of two-photon imaging are available in commercial microscopes. However, multiphoton imaging through multimode optical fibers has not been demonstrated until this work.

#### 4.4.2 First demonstration of two-photon imaging through a multimode fiber

Once we are able to generate and scan a grid of focused pulses at different planes through the multimode fiber, the next step is to use the system as a two-photon endoscope. In two photon fluorescent emission (2PFE), two photons of long excitation wavelength are simultaneously absorbed by a fluorophore. When the fluorophore returns from the excited to the ground state, a photon of higher energy than any of the two absorbed photons is emitted [40].

To acquire an image, optical pulses focused through the fiber are scanned over a volume composed of a fluorescent material or biological sample. The fluorescence is collected through the same fiber and “picked up” by a dichroic mirror as shown in Figure 4:2 and then detected and amplified by a photo-multiplier tube (PMT). To increase the signal to noise ratio (SNR) of the fluorescent signal, two short pass filters with cutoff wavelength of 650 nm and 700 nm, not shown in Figure 4:2, are placed in front of the PMT. On the proximal side, the microscope objective and optical lenses placed between the dichroic mirror and the fiber produced undesired reflections that add background intensity to the fluorescent signal detected at the PMT. With the combination of the dichroic mirror and two short-pass filters the background intensity from the excitation beam is significantly suppressed, allowing the detection of the two-photon fluorescent signal detected through the fibers.

For the first imaging demonstration a thick fluorescent sample is prepared and placed on the distal side of the fiber. The fluorescent signal is collected through the same fiber and measured on the proximal side with a PMT. The first sample consists of no-fluorescent 20 micrometer diameter beads suspended in a fluorescent homogeneous medium of PDMS stained with Rhodamine 6G. The recorded image is shown in Figure 4:7. Here the fluorescence comes from the medium around the beads, but the contrast between the beads and the medium makes possible the acquisition of the image.

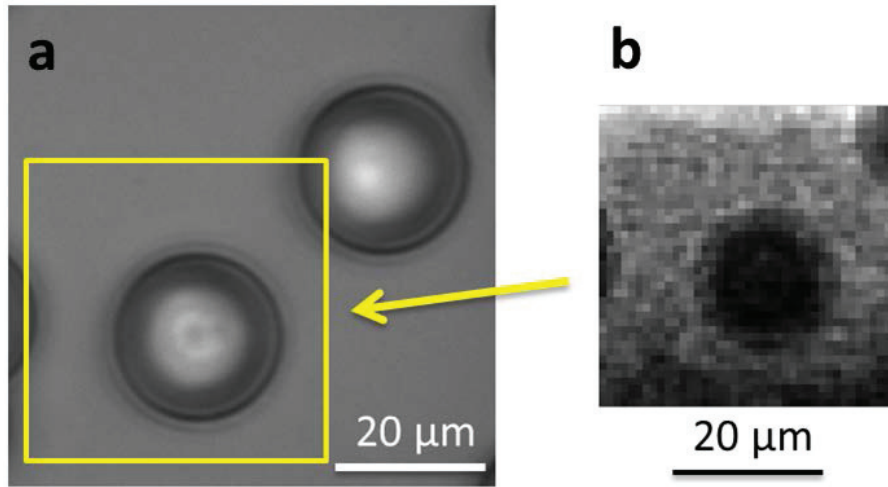


Figure 4:7 The first two-photon image acquired through a multimode optical fiber. (a) Bright-field transmission image using a 40x objective. (b) Two-photon excitation image through a 200 micrometer core multimode fiber. The bead looks dark because, in this case, the surrounding medium is fluorescent and the bead is not. The yellow circle represents the scanning window used for the acquisition of the two-photon image.

#### 4.4.3 Imaging of fluorescent beads through the multimode fiber

The next sample consists of 1-5  $\mu\text{m}$  fluorescent beads (Cospheric FMR – Red Fluorescent Microspheres) suspended in a transparent PDMS volume. The spectral emission of the beads is centered at 575 nm. The fluorescent beads were mixed with PDMS in a concentration of 1 mg of beads per 100 mg of PDMS with 10 mg of curing agent. A drop of the mixture was placed on a 100  $\mu\text{m}$  thick glass slide and spin coated 60 seconds at 1000 rpm to achieve a flat 55  $\mu\text{m}$  PDMS thickness. Finally, the sample was cured in a hot plate at 80° C for 60 minutes. This solidifies the PDMS and fixes the beads in the volume. The sample is illustrated in Figure 4:8.

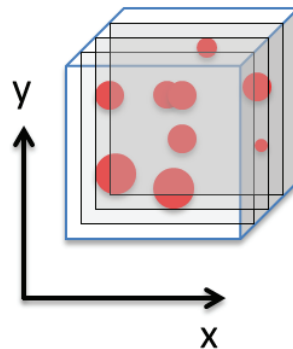


Figure 4:8 3D volume of fluorescent beads suspended in non-fluorescent PDMS.

An excitation wavelength of 800 nm is used. The spectral emission of the beads is centered at 575 nm. We scan the focused pulse digitally by changing the phases on the SLM every 700 nm in a grid of 40x70 points (28x49  $\mu\text{m}$  FOV). We scan the planes from 0 to 50  $\mu\text{m}$  inside the sample. Figure 4:9 shows the sectioned images. A Gaussian filter of 0.5 variance is applied on the image to reduce noise. Both set of images, with and without filtering are shown below.

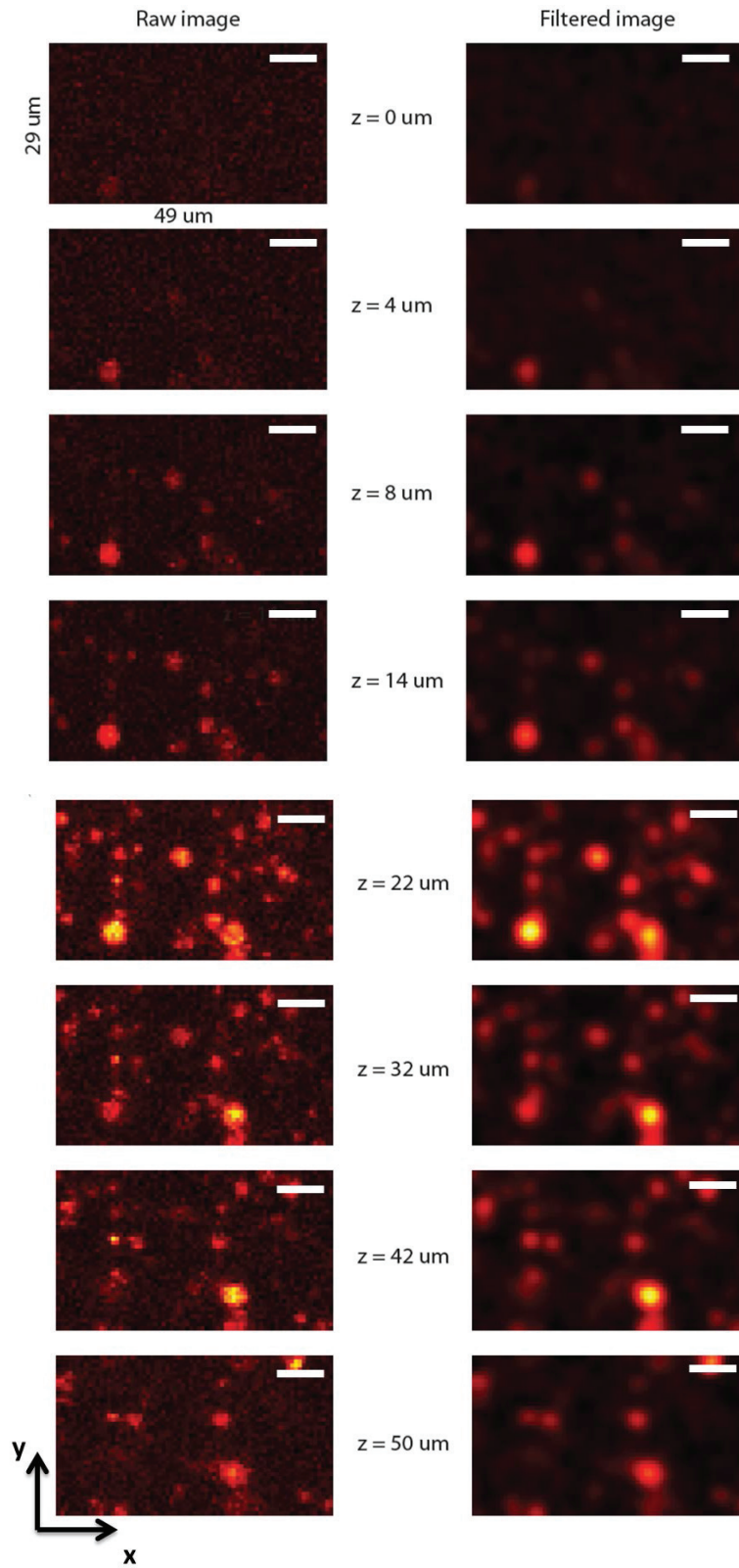


Figure 4:9 Two-photon images of fluorescent beads. Scanning volume is  $28 \times 49 \times 50 \text{ } \mu\text{m}$ . Scale bars are  $10 \text{ } \mu\text{m}$ .



The following images show two examples samples of the planes perpendicular to the plane shown in Figure 4:9.

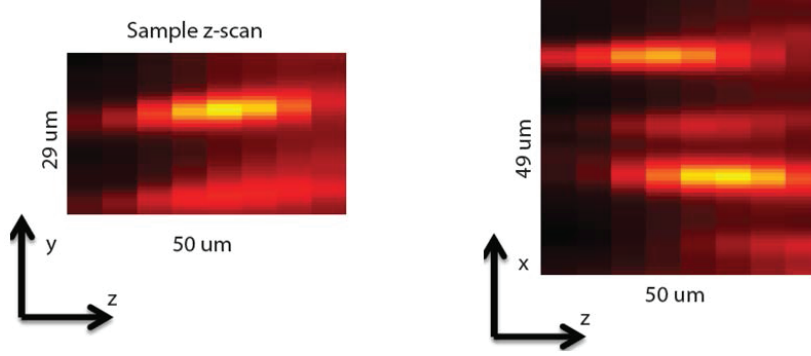


Figure 4:10 Two-photon images of fluorescent beads. (Left) y-z plane, (right) x-z.

In multi-photon absorption, the number of fluorescent photons produced in two-photon emission is given by [40]:

$$n_a \approx \frac{p_0^2 \delta}{\tau_p f_p^2} \left( \frac{NA^2}{2hc\lambda} \right)^2$$

Equation 4:2 – Fluorescent photons.

Where  $n_a$  is the number of fluorescent photons,  $p_0$  is the average power,  $\tau_p$  is the pulse length,  $f_p$  is the repetition rate of the source,  $\delta$  is the two-photon absorption cross section and NA is the numerical aperture of the fiber.

#### 4.4.4 Characterization and compensation of the non-uniform resolution over the field of view

As described before, the intensity enhancement and spot size is a function of the scanning position at the distal end of the fiber. Hence, we calculate a quantity proportional to  $n_a$  called the normalized two-photon fluorescence (2PF normalized), which is shown in Figure 4:11. In a homogeneous fluorescent medium, focused pulses generated through the fiber near the center of the optical axis produce a larger number of fluorescent photons. Therefore, to reconstruct correctly the original image, we require a compensation of the over-measured intensity in the central area, which can be performed as a post-acquisition process.

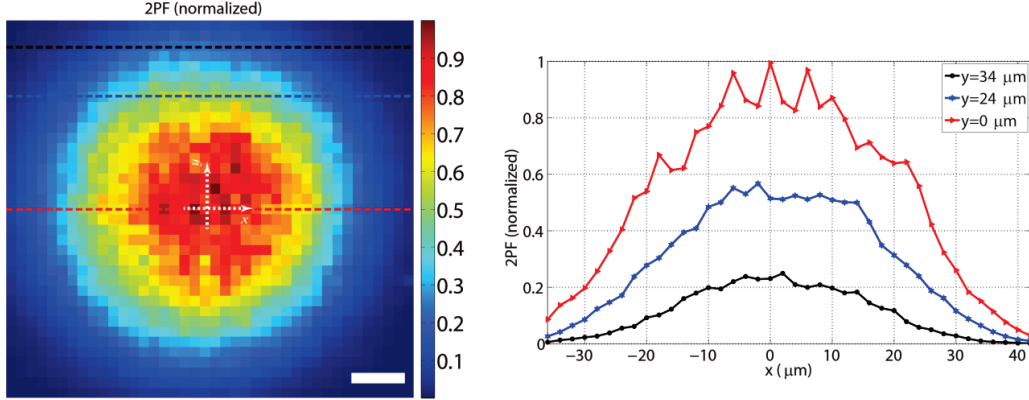


Figure 4:11 Normalized fluorescent photons as a function of position. Scale bar is 10  $\mu\text{m}$ .

Two-photon fluorescence occurs in a smaller volume than single photon absorption. Hence, the point spread function (PSF) of the two-photon imaging fiber device is  $\sqrt{2}$  times smaller than the linear PSF. Additionally, 2PF suppresses the out of focus excitation. This is illustrated in Figure 4:12, which shows the linear and 2PF PSF of the fiber imaging system. The intensity after the first zero of the airy disk is significantly reduced by the two-photon process as seen in Figure 4:12. In summary, the 2PF images acquired with the proposed system have a lateral resolution smaller than 1.05  $\mu\text{m}$  within a 40  $\mu\text{m}$  diameter circle centered at the optical axis with a two-photon equivalent enhancement larger than 57,000. Resolution is smaller than 1.4  $\mu\text{m}$  in a 60  $\mu\text{m}$  diameter FOV. The axial resolution, which is associated to the depth of field, is given by:  $d_z = 2.22\lambda/NA^2$ . Near the optical axis, the theoretical single photon axial resolution is 15  $\mu\text{m}$  and the two-photon axial resolution 10  $\mu\text{m}$  (a factor of  $\sqrt{2}$  smaller). This calculated value matches the experimental data. From the line profile, we obtain a Gaussian fit. Then, we numerically de-convolve the fitted data with a simulated 4  $\mu\text{m}$  size fluorescent bead. The de-convolution results in a two-photon PSF of 10  $\mu\text{m}$  resolution, which matches the theoretical value. The maximum average power delivered to the sample is 22 mW, which corresponds to a spot energy of 0.27  $\text{mJ}/\text{cm}^2$ .



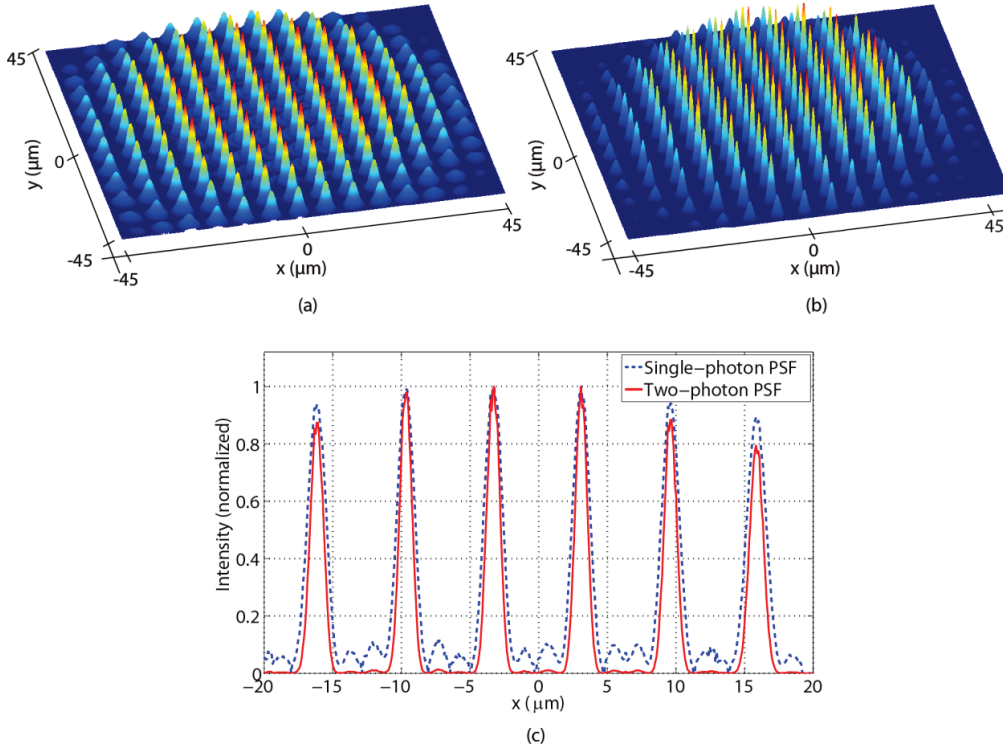


Figure 4:12 Experimental PSF of the multimode fiber imaging system. (a) Single-photon fluorescence. (b) Two-photon fluorescence. (c) Normalized PSF of (a) and (b) at  $y = 0$ .

#### 4.4.5 Imaging of biological samples with the two-photon multimode fiber endoscope

As mentioned before, both set of images shown in section 4.4.2 and 4.4.3 were acquired through a 200  $\mu\text{m}$  core diameter, 20 cm long graded index multimode fiber. However, to increase the resolution of the two-photon imaging system a graded index (grin) lens (0.5 mm length, 70° view angle, 250  $\mu\text{m}$  diameter) is attached to the distal end of the multimode fiber as shown in Figure 4:13 Multimode fiber probe. The white horizontal lines are the reflection of the lamp of the microscope. The images shown in section 4.4.2 and 4.4.3 were taken with the lensed fiber. The lens increases the numerical aperture of the fiber from 0.29 to 0.34 (resolution changed from 1.2  $\mu\text{m}$  to 1  $\mu\text{m}$ ) but reduces the circular field of view (FOV) of the fiber from 200  $\mu\text{m}$  diameter to 106  $\mu\text{m}$ . The increase of the NA is not so significant because the lens diameter is larger than the core diameter of the fiber, otherwise the NA can be increase to above 0.5 as will be shown in the next sections. There is a tradeoff between resolution, FOV and probe diameter. For example, using a fiber with a core diameter equal to 600  $\mu\text{m}$  and a lens of same magnification as the one used in our experiments, the maximum FOV of the system would be 318  $\mu\text{m}$ . The multiphoton imaging principle demonstrated in this work can be extended to lensless and thinner or thicker graded index fibers without loss of generality.

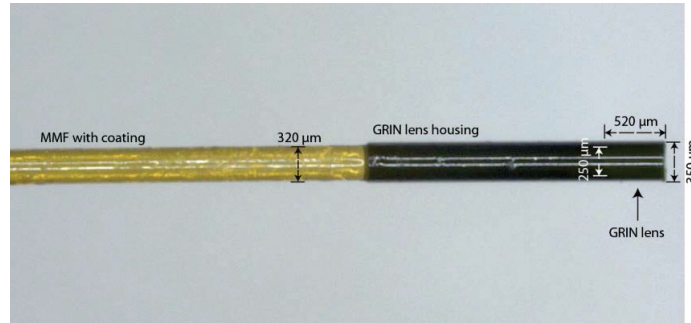


Figure 4:13 Multimode fiber probe. The white horizontal lines are the reflection of the lamp of the microscope. The fiber is 20 cm length (only the lensed side of the fiber is shown)

Using the multimode fiber endoscope based on the optical fiber shown in Figure 4:13, but of 10 cm length instead of 20 cm, two-photon fluorescent images of biological tissue were acquired. The fiber was shortened for the following reason. As explained in Chapter 3, the ability to focus light through multimode fibers is directly linked to the number of phase conjugated modes, which depends on the temporal separation of the time-sampled modes when they reach the other end of the fiber in the calibration step. Since each mode travels at a constant speed, in a very long fiber, sampling of only one mode is possible. However, the ability to focus light depends on the degrees of freedom or number of modes phase-conjugated. Therefore, spatial focus could not be achieved upon phase conjugation, only a transmission of the mode spatial intensity profile. On the contrary, if a shorter fiber is used, more modes per temporal window can be sampled, counter propagate and constructively interfere, allowing a sharper and brighter phase conjugated spot. A brighter spot produces a larger number of fluorescent photons as shown in Equation 4:2. Therefore, we select a shorter fiber, 5 cm long. In the experiments shown in the rest of the chapter, no GVD compensation is used because the fiber is so short that the gain in peak power is equivalent to the losses introduced by the GVD compensation prism pair. Therefore it is not necessary to make the compensation at this shorter fiber length.

The chosen sample is an ex-vivo organ of corti, which is a structure that contains the hearing cells. It is located inside the cochlea of humans and many animals. In mammals, the cochlea has a spiral structure inside the inner ear.

In all the following images of biological tissue acquired through the fiber, an ex-vivo mouse organ of corti is used as the specimen. On average, the thickness of the tissue conforming the organ of corti is 50  $\mu\text{m}$ . The organ of corti is extracted from a mouse cochlea and stained with Rhodamine 6G, which is a common fluorophore used in two-photon imaging at excitation wavelengths centered at 800 nm, as in this multimode fiber endoscopic system.

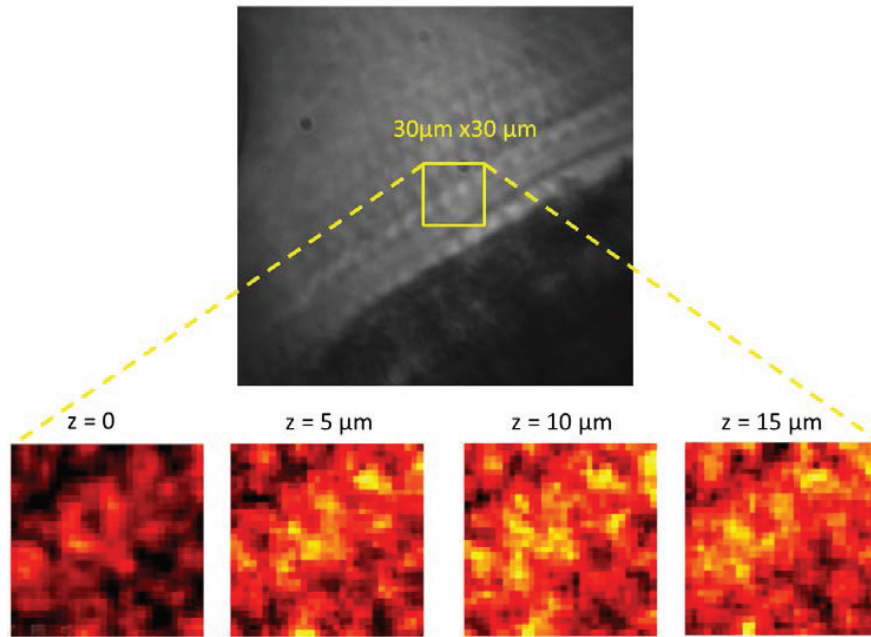


Figure 4:14 Imaging of biological tissue through the multimode fiber. (Above) Bright field transmission image of the sample. (Below) Sectioned images acquired through the multimode fiber.

The upper part of Figure 4:14 shows the white light transmission image of the organ of Corti acquired with a control camera (Camera 2 in Figure 4:2). The lower part shows a sequence of two-photon images at different depths within the sample taken through the multimode fiber endoscope. For this type of sample, the resolution ( $1.4 \mu\text{m}$ ) is not enough to visualize the spacing between the contiguous cells. In the mouse cochlea, the diameter of the hearing cells range from  $5$  to  $7 \mu\text{m}$ .

#### 4.4.6 Increasing the resolution of the multimode fiber endoscope

The lensed fiber design shown in Figure 4:13 only increases the NA of the fiber from  $0.29$  to  $0.34$  due to the fact that the lens diameter ( $250 \mu\text{m}$ ) is larger than the fiber core diameter ( $200 \mu\text{m}$ ). This lens was the smallest diameter lens found commercially available. Therefore, light traveling from the fiber towards the lens does not cover the entire radius of the lens, which means that does not take all the advantage of the NA that could be achieved if the light emerging from the fiber covers the entire lens. To overcome such limitation, in the following lensed fiber, larger fiber core diameters are used.

The next imaging probe is a graded index multimode fiber with  $600 \mu\text{m}$  core diameter of  $5 \text{ cm}$  length. A semi-spherical lens is attached to one fiber ends to increase its numerical aperture and the resolution of the imaging device. The fiber embodiment is shown in Figure 4:15. The semi-sphere provides the fiber with a maximum NA at a working distance of  $180 \mu\text{m}$  as shown in Figure 4:17. We selected this fiber-semi-sphere configuration because the working distance is a necessary feature in two-photon to access deep within the tissue. With a  $0$  working distance, as in the case of the fiber-lens arrangement of Figure 4:13, the zero working distance of the GRIN lens implies that any spot generated far from the proximal tip will have a resolution degraded as explained in chapter 3. Therefore, the half sphere is more convenient in this case

to be able to image deep within the sample. The position of the semi-sphere shown in Figure 4:15 was the only one easy to integrate. However, the preferred design shown in Figure 4:16, which could not be attached by conventional methods ensuring sealing and isolation of the air space between the fiber and the lens, would have been more convenient for imaging in biological tissue which is usually surrounded by blood or water in living cavities. In such embodiment, the increased NA is produced by the light bending capability of the half sphere occurring at the sapphire-air interface. If the fiber shown in Figure 4:15 is dip into a liquid cavity, the increase NA capability is significantly reduced, whereas in the preferred embodiment shown on Figure 4:16, the sapphire-air interface is between the lens and the fiber, providing a final tip that can be dip into a high NA medium without a significant decrease in the resolution.

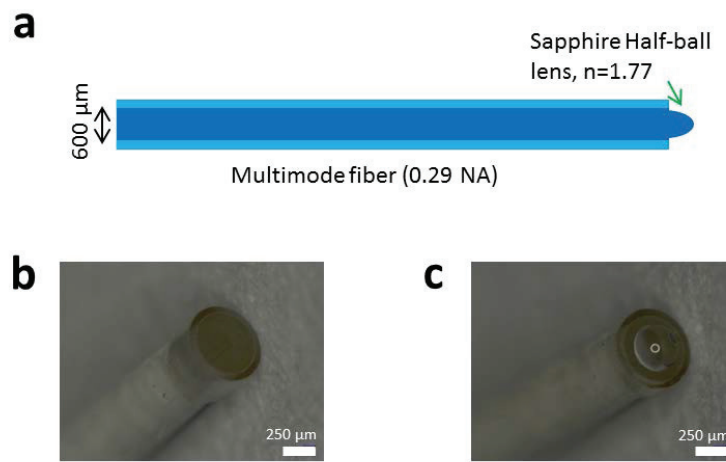


Figure 4:15 Multimode fiber lensed with a half-ball lens. (a) Graded index multimode fiber with a half sphere attached to one end. Fiber length is 5 cm. (b) Proximal side of the fiber endoscope. (c) Distal side of the fiber endoscope. The white circle in the center of the half sphere is the reflection of the lamp of the microscope used to acquire the image.

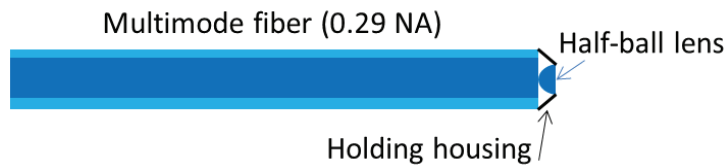


Figure 4:16 Preferred embodiment of the fiber lensed with a half-ball or semi-sphere lens. In terms of optical performance this arrangement is equivalent to the one shown in Figure 4:15 (a). This embodiment could not be attached with conventional methods.

Although the working distance can be kept fixed and z scanning can be accomplished by moving vertically the sample, the main drawback of the resolution in the semi-sphere approach lies on its strong dependence on lateral position as shown in Figure 4:17. The rapid drop in the lateral and axial resolution or NA as a spot is generated farther from the optical axis significantly limits the resolution of the imaging device, as shown in Figure 4:18 and Figure 4:19. A better implementation would be to use a custom built multi-element imaging system, which can be 3D printed directly on the tip of the fiber such as the one shown in [41, 42]. However, for the demonstration of two-photon imaging through multimode fibers, although with a reduced field of view, the half-sphere lens approach is enough.

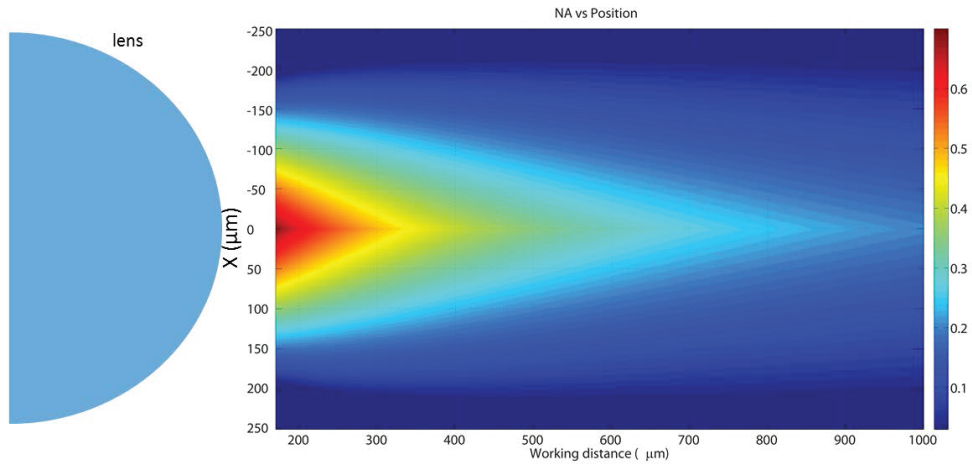


Figure 4:17 Calculated NA versus lateral x position for the MMF lensed with a half-sphere sapphire lens shown in Figure 4:15. The calculation starts at the working distance with the highest resolution ( $wd = 180 \mu\text{m}$ ).

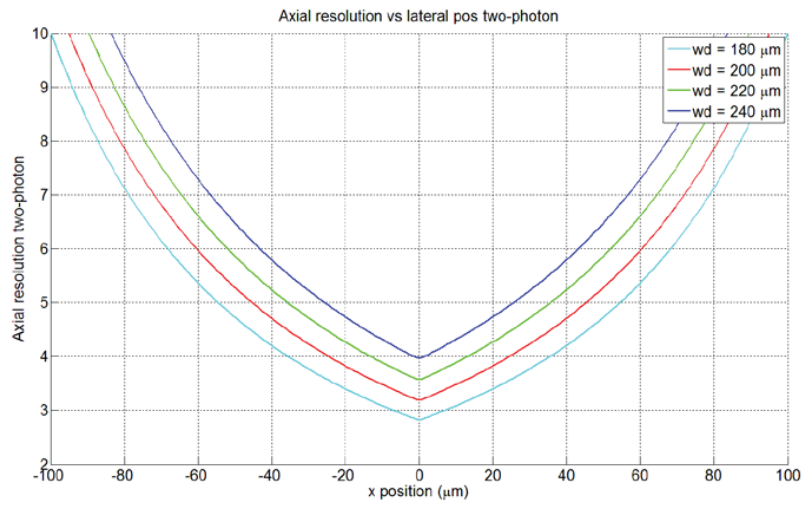


Figure 4:18 Calculated axial resolution versus lateral x position of the multimode fiber endoscope shown in Figure 4:15.

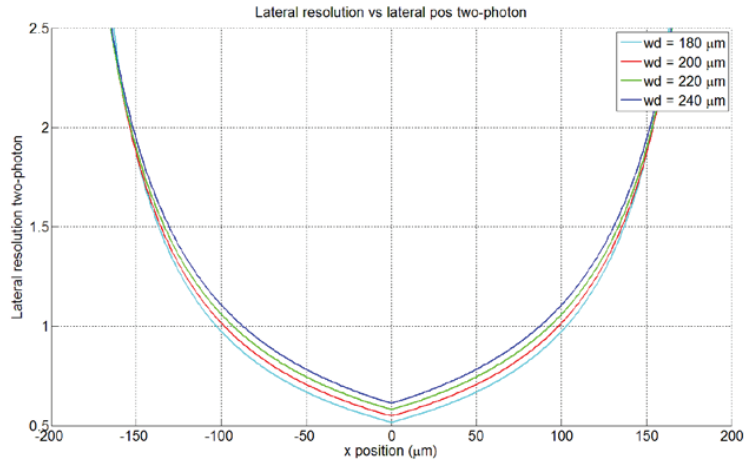


Figure 4:19 Calculated lateral resolution versus lateral x position of the multimode fiber endoscope shown in Figure 4:15.

#### 4.4.7 Two-photon imaging of biological samples with the multimode fiber endoscope

The extracted stained organ of corti is fixed on a coverglass as shown in Figure 4:20. The lensed tip of the fiber is placed at 180  $\mu\text{m}$  from the tissue. The shaped wavefront is reconstructed and the lateral scan of the focused pulses on the sample is accomplished by changing the reconstructed phases on the SLM. The sample is moved away from the fiber by a motorized stage with a step of 4  $\mu\text{m}$ . At each position, the spots are digitally scanned in an entire plane with a 0.5  $\mu\text{m}$  lateral separation. For each generated spot, a two photon signal is measured and the image for each plane is acquired.

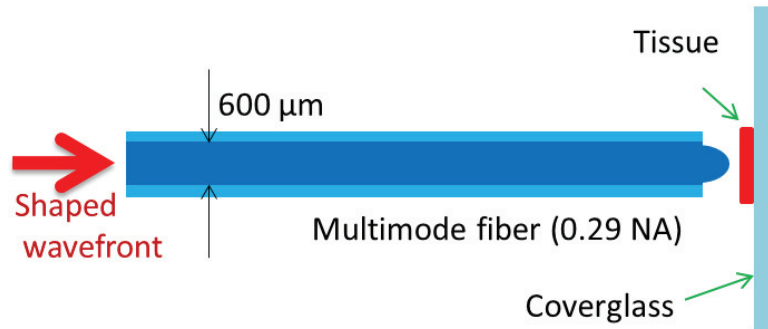


Figure 4:20 Two-photon imaging configuration.

Figure 4:21 shows the white light transmission image of the sample. Figure 4:22 shows the respective sections of the acquired two-photon images. These images were not post processed neither enhanced after acquisition. They clearly show the sectioning capability of two-photon emission. The hearing cells can be evidently identified.



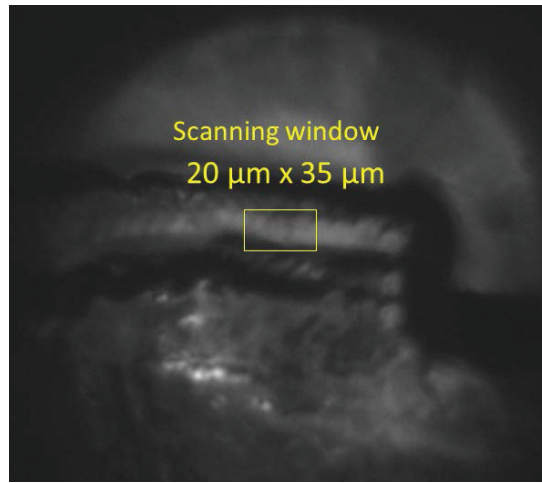


Figure 4:21 White light transmission image of the mouse cochlea.

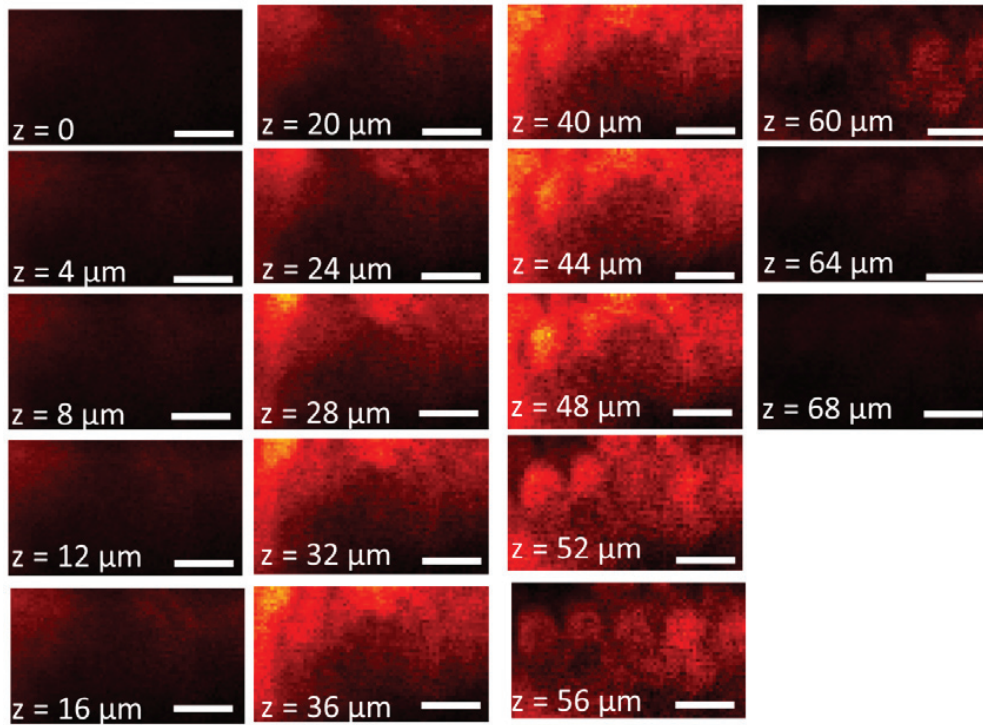


Figure 4:22 Two-photon images of the stained mouse cochlea acquired with the multimode fiber endoscope. The circle structures are the hearing cells. These are the raw images, no image processing or noise reduction filter has been applied. Scale bars are 9 μm.

The experiment was repeated using an extended field of view in order to visualize a larger number of hearing cells. The wide field image of the sample and the two-photon sections are shown in Figure 4:23. The two-photon sections are displayed in Figure 4:24. The lateral scanning step is 0.5 μm.

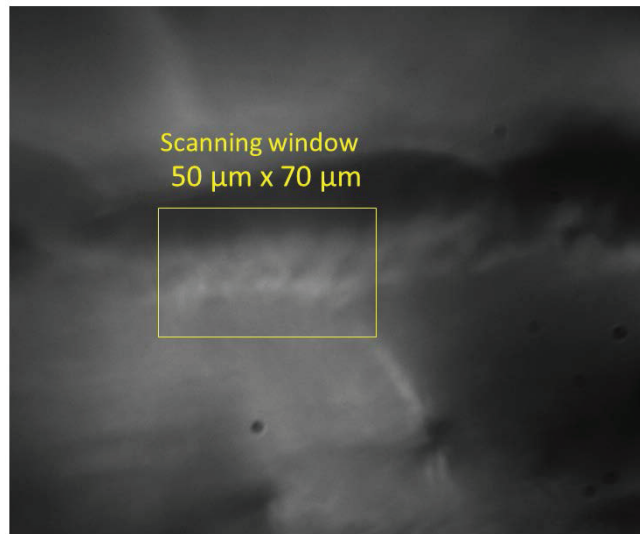


Figure 4:23 White light transmission image of the mouse cochlea.

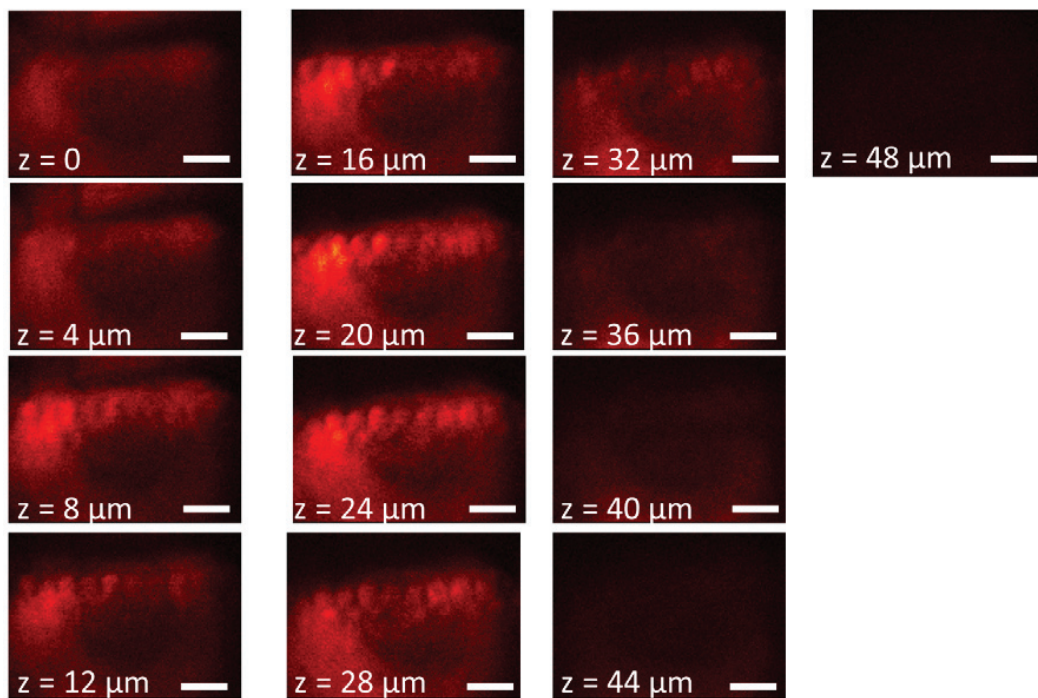


Figure 4:24 Two-photon images of the stained mouse cochlea over an extended field of view acquired with the multimode fiber endoscope. The circle structures are the hearing cells. These are the raw images, no image processing or noise reduction filter has been applied. Scale bars are  $14 \mu\text{m}$ .

As a comparison, two photon images of a mouse cochlea were taken with a commercially available two photon microscope (Leica TSC SP5 multi-photon). The images are shown in Figure 4:25.

Comparing Figure 4:24 and Figure 4:25, both, the endoscope and the two-photon microscope provide images in which the hearing cells can be visualized, which is necessary for research in



biological and some clinical applications. The difference lies in the resolution, which in the proposed multimode fiber approach is given by a numerical aperture equal to 0.58 at the optical axis, whereas in the commercial two-photon, the numerical aperture of the objective is 1, which is higher. Regarding the acquisition time, on the MMF system, it is limited by the refresh rate of the SLM (20 Hz). At maximum SLM refresh rate, each section of Figure 4:24 takes 12 minutes to be acquired whereas in the two photon microscope a couple of seconds.

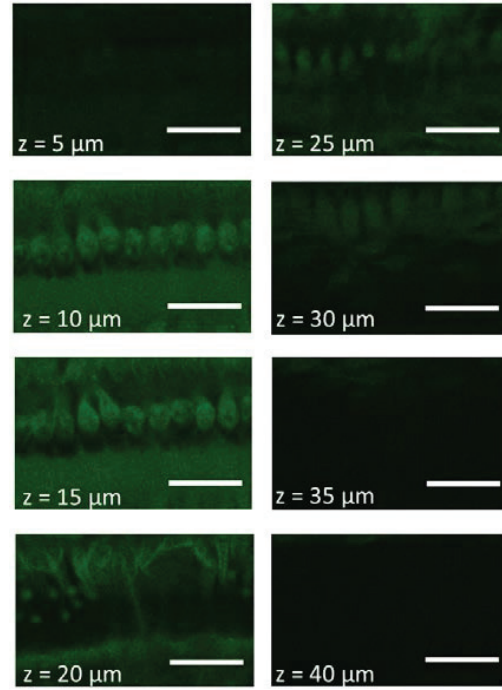


Figure 4:25 Two-photon images of the stained mouse cochlea acquired with a commercial two-photon microscope (Leica TSC SP5 multiphoton microscope). The rounded structures are the hearing cells. Scale bars are 25  $\mu\text{m}$ .

## 4.5 Conclusions

In this chapter, two-photon excitation imaging of fluorescent beads and biological tissue through various optical fibers has been demonstrated. Our method is based on time-gated digital phase conjugation, which allows the generation of focused pulses on the other side of a multimode fiber. To acquire an image, the focused femtosecond pulse is scanned in a three-dimensional mesh, producing two-photon excitation on each spatial location of the thick sample. Collecting the fluorescence through the fiber, a two-photon 3D image was acquired.

Our digital scanning method does not require distal mechanical elements, allowing an ultra-thin probe of 350  $\mu\text{m}$  diameter. The large area of the fiber and high numerical aperture (0.34 NA) allows large collection efficiency. The reduced modal dispersion of graded-index fibers allows the simultaneous control of a larger number of modes, generating a brighter focused pulse compared to the case of step-index fibers. Time-gated phase conjugation of a pre-GVD compensated beam prevents pulse broadening due to GVD of the pulse propagating through the fiber, generating an ultrashort pulse of 120 fs duration. The high intensity focused pulse is

generated outside of the fiber avoiding nonlinearities in the propagating pulse. Our work sets the basis for in-vivo ultra-thin two-photon endoscopy.

We made several attempts to increase the resolution of the imaging system by attaching various types of lenses to the multimode fiber. However, the best way to achieve, but not immediately available at the time in which we performed those experiments, is to micro-fabricate a custom objective on the tip of the fiber as in [41, 42].

The imaging probe provides an image quality comparable to those achieved with commercial two-photon microscopes. Therefore, it sets the basis for a next generation of minimally invasive endoscopes that in the future could be available in research labs and hospitals.

## 4.6 Acknowledgements

I would like to thank Marilisa Romito from the Laboratory of Optics (LO) at EPFL for extracting and staining the mouse cochleas used in the presented experiments.

## 4.7 References

1. B. A. Flusberg, E. D. Cocker, W. Piyawattanametha, J. C. Jung, E. L. M. Cheung, and M. J. Schnitzer, "Fiber-optic fluorescence imaging," *Nat Methods* 2, 941-950 (2005).
2. K. Carlson, M. Chidley, K.-B. Sung, M. Descour, A. Gillenwater, M. Follen, and R. Richards-Kortum, "In vivo fiber-optic confocal reflectance microscope with an injection-molded plastic miniature objective lens," *Appl Optics* 44, 1792-1797 (2005).
3. C. Liang, K.-B. Sung, R. R. Richards-Kortum, and M. R. Descour, "Design of a high-numerical-aperture miniature microscope objective for an endoscopic fiber confocal reflectance microscope," *Appl Optics* 41, 4603-4610 (2002).
4. A. R. Rouse, A. Kano, J. A. Udovich, S. M. Kroto, and A. F. Gmitro, "Design and demonstration of a miniature catheter for a confocal microendoscope," *Appl Optics* 43, 5763-5771 (2004).
5. W. Göbel, J. N. D. Kerr, A. Nimmerjahn, and F. Helmchen, "Miniaturized two-photon microscope based on a flexible coherent fiber bundle and a gradient-index lens objective," *Opt Lett* 29, 2521-2523 (2004).
6. P. M. Lane, A. L. P. Dlugan, R. Richards-Kortum, and C. E. MacAulay, "Fiber-optic confocal microscopy using a spatial light modulator," *Opt Lett* 25, 1780-1782 (2000).
7. A. F. Gmitro and D. Aziz, "Confocal microscopy through a fiber-optic imaging bundle," *Opt Lett* 18, 565-567 (1993).
8. A. R. Rouse and A. F. Gmitro, "Multispectral imaging with a confocal microendoscope," *Opt Lett* 25, 1708-1710 (2000).
9. I. M. Vellekoop and A. P. Mosk, "Focusing coherent light through opaque strongly scattering media," *Opt Lett* 32, 2309-2311 (2007).
10. M. Kim, Y. Choi, C. Yoon, W. Choi, J. Kim, Q. H. Park, and W. Choi, "Maximal energy transport through disordered media with the implementation of transmission eigenchannels," *Nat Photonics* 6, 581-585 (2012).

11. D. B. Conkey, A. M. Caravaca-Aguirre, and R. Piestun, "High-speed scattering medium characterization with application to focusing light through turbid media," *Opt Express* 20, 1733-1740 (2012).
12. S. M. Popoff, G. Lerosey, R. Carminati, M. Fink, A. C. Boccara, and S. Gigan, "Measuring the Transmission Matrix in Optics: An Approach to the Study and Control of Light Propagation in Disordered Media," *Phys Rev Lett* 104, 100601 (2010).
13. I. M. Vellekoop and A. P. Mosk, "Universal Optimal Transmission of Light Through Disordered Materials," *Phys Rev Lett* 101, 120601 (2008).
14. I. N. Papadopoulos, S. Farahi, C. Moser, and D. Psaltis, "Focusing and scanning light through a multimode optical fiber using digital phase conjugation," *Opt Express* 20, 10583-10590 (2012).
15. I. N. Papadopoulos, S. Farahi, C. Moser, and D. Psaltis, "High-resolution, lensless endoscope based on digital scanning through a multimode optical fiber," *Biomed Opt Express* 4, 260-270 (2013).
16. A. Yariv, "Three-dimensional pictorial transmission in optical fibers," *Appl Phys Lett* 28, 88-89 (1976).
17. P. R. Forman, F. C. Jahoda, and B. L. Mason, "Multimode Fiber Interferometry with and without Phase Conjugation," *Appl Optics* 30, 1629-1632 (1991).
18. I. McMichael, P. Yeh, and P. Beckwith, "Correction of Polarization and Modal Scrambling in Multimode Fibers by Phase Conjugation," *Opt Lett* 12, 507-509 (1987).
19. Y. Pu, X. Yang, I. Papadopoulos, S. Farahi, C.-L. Hsieh, C. A. Ong, C. Moser, D. Psaltis, and K. Stankovic, "Imaging of the Mouse Cochlea with Two-photon Microscopy and Multimode Fiber-based Microendoscopy," in *Biomedical Optics 2014*, OSA Technical Digest (online) (Optical Society of America, 2014), BT4A.3.
20. M. Ploschner, T. Tyc, and T. Cizmar, "Seeing through chaos in multimode fibres," *Nat Photonics* 9, 529-+ (2015).
21. Y. Choi, C. Yoon, M. Kim, T. D. Yang, C. Fang-Yen, R. R. Dasari, K. J. Lee, and W. Choi, "Scanner-Free and Wide-Field Endoscopic Imaging by Using a Single Multimode Optical Fiber," *Phys Rev Lett* 109(2012).
22. S. F. Damien Loterie, Ioannis Papadopoulos, Alexandre Goy, Demetri Psaltis, and Christophe Moser, "Digital confocal microscopy through a multimode fiber," *Opt Express* 23(2015).
23. D. Kim, J. Moon, M. Kim, T. D. Yang, J. Kim, E. Chung, and W. Choi, "Toward a miniature endomicroscope: pixelation-free and diffraction-limited imaging through a fiber bundle," *Opt Lett* 39, 1921-1924 (2014).
24. R. Di Leonardo and S. Bianchi, "Hologram transmission through multi-mode optical fibers," *Opt Express* 19, 247-254 (2011).
25. T. Cizmar and K. Dholakia, "Exploiting multimode waveguides for pure fibre-based imaging," *Nat Commun* 3(2012).
26. T. Cizmar and K. Dholakia, "Shaping the light transmission through a multimode optical fibre: complex transformation analysis and applications in biophotonics," *Opt Express* 19, 18871-18884 (2011).
27. S. Bianchi and R. Di Leonardo, "A multi-mode fiber probe for holographic micromanipulation and microscopy," *Lab Chip* 12, 635-639 (2012).

28. M. Ploschner, B. Straka, K. Dholakia, and T. Cizmar, "GPU accelerated toolbox for real-time beam-shaping in multimode fibres," *Opt Express* 22, 2933-2947 (2014).
29. A. M. Caravaca-Aguirre, E. Niv, and R. Piestun, "High-Speed Phase Modulation for Multimode Fiber Endoscope," in *Imaging and Applied Optics 2014*, OSA Technical Digest (online) (Optical Society of America, 2014), ITh3C.1.
30. R. Y. Gu, R. N. Mahalati, and J. M. Kahn, "Noise-reduction algorithms for optimization-based imaging through multi-mode fiber," *Opt Express* 22, 15118-15132 (2014).
31. E. R. Andresen, G. Bouwmans, S. Monneret, and H. Rigneault, "Two-photon lensless endoscope," *Opt Express* 21, 20713-20721 (2013).
32. E. E. Morales-Delgado, S. Farahi, I. N. Papadopoulos, D. Psaltis, and C. Moser, "Delivery of focused short pulses through a multimode fiber," *Opt Express* 23, 9109-9120 (2015).
33. D. G. Shamir Rosen, Ori Katz, Yaron Silberberg, "Focusing and Scanning through Flexible Multimode Fibers without Access to the Distal End," <http://arxiv.org/abs/1506.08586> (2015).
34. B. E. A. S. a. M. C. Teich, *Fundamentals of Photonics*, 2nd Edition ed. (Wiley).
35. M. Müller, J. Squier, and G. J. Brakenhoff, "Measurement of femtosecond pulses in the focal point of a high-numerical-aperture lens by two-photon absorption," *Opt Lett* 20, 1038-1040 (1995).
36. O. Lammel and A. Penzkofer, "Femtosecond pulse duration measurement by two-photon fluorescence detection," *Optical and Quantum Electronics* 32, 1147-1160 (2000).
37. R. L. Fork, O. E. Martinez, and J. P. Gordon, "Negative Dispersion Using Pairs of Prisms," *Opt Lett* 9, 150-152 (1984).
38. L. V. Amitonova, A. P. Mosk, and P. W. H. Pinkse, "Rotational memory effect of a multimode fiber," *Opt Express* 23, 20569-20575 (2015).
39. R. Y. Gu, R. N. Mahalati, and J. M. Kahn, "Design of flexible multi-mode fiber endoscope," *Opt Express* 23, 26905-26918 (2015).
40. J. S. W. Denk, W. W. Webb, "Two-photon laser scanning fluorescence microscopy," *Science* 248, 73-76 (1990).
41. T. Gissibl, M. Schmid, and H. Giessen, "Spatial beam intensity shaping using phase masks on single-mode optical fibers fabricated by femtosecond direct laser writing," *Optica* 3, 448-451 (2016).
42. T. Gissibl, S. Thiele, A. Herkommer, and H. Giessen, "Two-photon direct laser writing of ultracompact multi-lens objectives," *Nat Photon* 10, 554-560 (2016).

# Chapter 5 3D printing through a multimode fiber

In the previous chapter, the use of a multimode optical fiber as a two-photon endoscope has been presented. The working principle is based on the scanning of focused optical pulses through the multimode fiber. The small focusing area, short temporal duration (hundreds of femtoseconds) and high peak power of the delivered pulses can generate multi-photon absorption processes that are not limited to imaging as will be shown.

This chapter presents how the capability of producing multi-photon phenomena at the tip of an ultra-thin needle can be exploited in a completely different application: 3D printing. In this case, instead of producing two-photon fluorescence, the focused optical pulses are used to trigger photo-polymerization of a material that is absorbent at half of the excitation wavelength.

3D printing based on additive manufacturing is an advanced manufacturing technique that allows the fabrication of arbitrary macroscopic and microscopic objects. Many 3D printing systems require large optical elements or nozzles in proximity to the built structure. This prevents their use in applications in which there is no direct access to the area where the objects have to be printed. Here, we demonstrate three-dimensional microfabrication based on two-photon polymerization (TPP) through an ultra-thin printing nozzle of 560  $\mu\text{m}$  in diameter. Using wavefront shaping, femtosecond infrared pulses are focused and scanned through a multimode optical fiber (MMF) inside a photoresist that polymerizes via two-photon absorption. We show the construction of arbitrary 3D structures built with voxels of diameters down to 400 nm on the other side of the fiber.

To our knowledge, this is the first demonstration of microfabrication through a multimode optical fiber. We call it endofabrication.

Some of the results presented in this chapter have been submitted for publication under the name: ***“Three-dimensional microfabrication through a multimode optical fiber”***. The article is currently under peer-reviewed process.

## 5.1 Introduction to photo-polymerization

As already mentioned briefly in Chapter 1, additive manufacturing consists on various fabrication techniques that enable the direct construction of objects of any desired shape and size made of materials such as plastics, metals, and ceramics from a computer aided designed (CAD) model. A 3D printing method that allows the fabrication of high resolution microstructures is Direct Laser Writing (DLW). In DLW structures can be made of a broad selection of polymer-based materials of various mechanical, electrical and optical properties. Applications of

micro-structures range from scaffold-like assemblies for cell growth [1, 2] to optical components such as complex micro lenses, waveguides, diffractive optical elements, photonic crystals, components for optical data storage, microfluidics, nanophotonics or micro-electromechanical systems (MEMS) [3-15]. All these structures can be built with hundreds of nanometers in resolution.

DLW is based on photo-polymerization, a phenomenon in which the solubility of a photosensitive material is reduced and becomes solid upon light exposure. Those materials are based on a resin made of chemical compounds called monomers that are mixed with a photo-initiator in order to become cross-linked upon absorption of photons, suffering a subsequent polymerization within the boundaries of the illuminated volume [16]. Similarly as it occurs in fluorescent microscopy, photo-polymerization can also be triggered by multi-photon absorption processes. In the case of two-photon polymerization (TPP), its nonlinear dependence on peak intensity results in a tightly confined volume of both absorption and polymerization within the high energy focused pulses impinging in the photoresists, leading to a smaller volume of polymerization when compared to single photon polymerization. Scanning of the light focus with respect to the photoresists allows the fabrication of structures [10, 17-20]. A post exposure phase known as “development” dissolves and removes the unexposed portion of the photoresists.

Since its first demonstration in 1996 [18], TPP has reached printed micro-structures with resolutions in the order of hundreds of nanometers [21]. As in STED microscopy, where a second light beam can be used to prevent fluorescence around the excitation light focus, a second beam can be used to inhibit polymerization in the surroundings of the light focus used to polymerize, allowing an enhanced resolution (tens of nanometers) in the printed micro structures in a single-photon absorption process [22, 23].

A significant disadvantage of all the existing DLW fabrication methods is that the 3D printed structures can only be fabricated in proximity to very large optical elements. This prevents the microfabrication of objects inside the body or in cavities difficult to access. In this chapter we present a new method that disrupts those limitations.

As explained in chapter 2, different methods to focus and scan light patterns [24-39] and optical pulses [40-44] through scattering media and multimode optical fibers have been developed. The multimode fiber itself does not directly allow the transmission of images or focused optical pulses. In the fiber, dispersion and modal mixing, given by the propagation of light as a set of fiber modes, produces a scrambled intensity profile and a broad temporal profile. We have previously developed the method presented in chapter 2 that allows the transmission of focused optical pulses with a femtosecond temporal profile unaffected by modal dispersion [42].

In the following sections, an experimental demonstration of two-photon polymerization 3D printing through a fiber-based optical system is presented. First, with a very simple setup, we characterize the minimum power and exposure time that allows polymerization of the photoresists with a microscope objective to investigate the feasibility of photo-polymerization under similar light focusing conditions as those available when focusing light through a multimode

optical fiber. Then, using a method for scanning and focusing of optical pulses through multimode fibers based on optical phase conjugation [45, 46] and wavefront shaping [42], fiber modes with the same group velocity are excited and forced to interfere at a given location forming a high intensity optical pulse. This focused pulse is scanned in a 3D volume of a photoresist, producing polymerization within the optical voxel, allowing the fabrication of structures of arbitrary shape with sub-micrometer resolution through the multimode fiber. This scanning method does not require any distal scanning element, allowing an ultra-thin 3D printing probe. In the end of the chapter the 3D printed micro-structures are shown.

From a technological point of view, this ultra-thin 3D printer enables high resolution microfabrication in a whole new set of applications where conventional 3D printing methods cannot have access, such as inside of biological tissue or in the interior of already built structures and places with difficult access.

## 5.2 Principle of two-photon polymerization

All the experiments presented in this chapter were conducted using a Ti:sapphire laser (Coherent Mira 900; with central wavelength  $\lambda_c=800$  nm; spectral width  $\sigma_\lambda=10$  nm; pulse length of 100 fs; repetition rate 76 MHz and maximum output average power of 800 mW). The photoresist used in all our experiments is IP-L 780 from Nanoscribe GmbH, which can be polymerized via two-photon absorption at an excitation wavelength centered at 800 nm.

In order to demonstrate the feasibility of multimode fiber 3D printing, we begin with simple DLW experiments, which consist on producing two-photon polymerization under peak power conditions as close as possible to those expected when focusing light through multimode fibers. To meet such conditions, we use a 40x microscope objective of 0.65 NA to focus the femtosecond light beam on the photoresists as shown in Fig. 5:1 (a). For DLW, objectives with very high NA are typically used (oil immersion objectives with NA = 1.4). However, in this case we use a lower NA objective because our goal is to polymerize through a lensed multimode fiber with a numerical aperture equal to 0.54. A detailed explanation of the DLW experiments is presented in the next paragraphs.

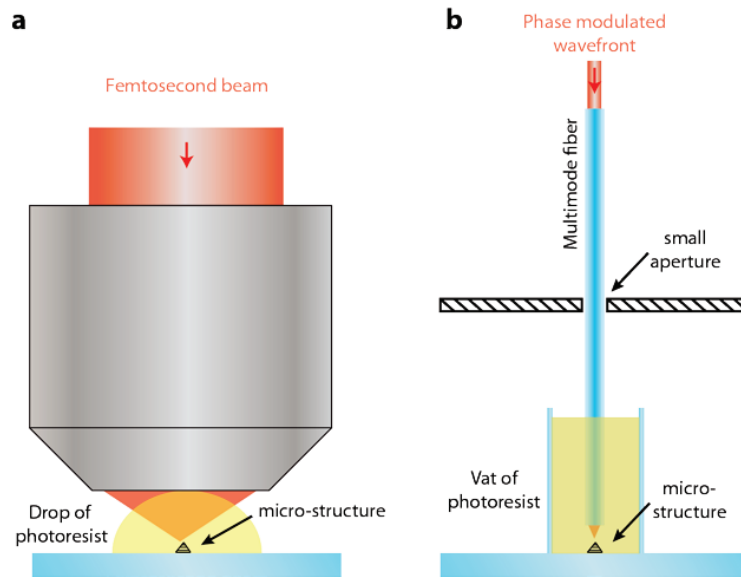


Figure 5:1 Working principle of direct laser writing (DLW). (a) DLW based on a microscope objective. (b) DLW based on a multimode fiber. The fiber can enter and micro-fabricate inside areas difficult to access.

Photoresists for TPP are usually composed of monomers mixed together with photoinitiators. Monomers are molecules capable of forming polymer chains via cross-linking [16]. This makes of the photo-resist a less soluble substance, when placed in the developer, in the regions where cross-linkage occurred. Cross-linking and its subsequent polymerization can be produced by free radicals [47, 48]. Those radicals are generated when the photoinitiator is exposed to light. Photoinitiators are made of molecules that can produce free-radicals when exposed to light.

Oxygen is an element present in the air that can inhibit polymerization as follows: It reacts with the free radicals produced by the illuminated photoinitiator forming peroxy radicals, which does not produce cross-linkage [49]. If the light intensity impinging on the photoresist is low, the oxygen diffused from the surroundings prevents polymerization because free radicals are generated at a smaller rate than the peroxy radicals. On the contrary, if the light intensity is high, the generation rate of free-radicals is larger than the generation rate of the non-polymerizing peroxy radicals, producing polymerization in the illuminated volume [16].

In polymerization the volume where the photoresist is polymerized is called a voxel. Being able to achieve the smallest possible voxel size is essential to create precise 3D micro-structures. As mentioned before, oxygen diffusion, laser power, exposure dose and optical resolution are the quantities that set the minimum achievable voxel size and the power threshold for polymerization.

Another important feature of photopolymerization is the inherent threshold characteristic of the cross-linking process. If the intensity of the light is below a certain threshold value, the photoresists will be removed by the developer, otherwise the exposed volume is polymerized when the light intensity is over the threshold. This occurs due to the non-linear solubility of the photo-resist in the developer as a function of exposure dose [16]. The solubility drops at a



given exposure dose, leading to the threshold behavior as depicted in Fig. 5:4 (a). The intensity distribution corresponds to the light intensity at the focal plane of a microscope objective (line profile of an Airy disk). Only the region of the light focus where the intensity is above the threshold level will produce photopolymerization.

The exposure dose can be expressed as:

$$D \propto \tau P^N$$

Equation 5.1: Exposure dose

Where  $\tau$  is the exposure time,  $P$  the power and  $N$  is the order of the non-linear absorption mechanism. The threshold power  $P_{\text{thres}}$  is proportional to  $\tau^{(-1/N)}$ , as can be derived from Eq. 5:1. The proportionality holds true when the exposure time is small. The threshold is produced by the non-linearity of its solubility [16]. On the other hand, for larger exposure times, the same exposure dose can be achieved by reducing the power. There is a limit in the minimum power that can trigger polymerization. At low light intensities, oxygen diffusion is more significant than the generation rate of radicals, preventing the occurrence of polymerization. Hence, at low intensities, the intensity threshold is given by the oxygen diffusion rather than by exposure time.

Photo-polymerization can occur independently of the excitation mechanism. Hence, it can be produced by single photon or multi-photon absorption.

### 5.3 Demonstration of two-photon polymerization with a microscope objective

These experiments begin with the photopolymerization using a microscope objective as shown in Fig. 5:2 (b)).

As mentioned in the previous section, the voxel diameter depends on the time the photoresist is exposed to light. Hence, in our first experiment, we characterize the 3D printed linewidth at different exposure times. The photoresist is sandwiched and sealed between two coverslips as illustrated in Fig. 5:2 (b). We set an average power at the back aperture of the objective at 20 mW, which is close to the peak power available when polymerizing through the multimode fiber. The excitation is delivered through a 170  $\mu\text{m}$  thickness glass which reaches the photoresists at the flat interface. To achieve different exposures, the microscope objective is moved at different velocities with respect to the photoresists along an 80  $\mu\text{m}$  line. The focused light on the photoresists follows a square zigzag path to ensure illumination of the photoresists even if the sample is slightly tilted with respect to the movement of the objective. To perform a linewidth characterization without shrinkage [47], we measure the linewidth with a differential interference contrast microscope (DIC microscope) without developing the sample. The results are shown in Fig. 5:2 (c). The highest printing velocity for which polymerization was detected is 90  $\mu\text{m/s}$ . This value corresponds to an exposure time per diffraction-limited spatial focus of 8.3 ms. The linewidth decreases for higher writing speeds as expected, with the smallest measured linewidth equal to 1.9  $\mu\text{m}$ . The linewidth is thick due to the layered struc-

ture used which over exposes several times the polymerized voxels when writing the next layer.

As mentioned at the beginning of this chapter, oxygen present in the air diffuses into the photoresist and acts as a cross-link inhibitor. In order to decrease the concentration of oxygen, nitrogen can be bubbled into the recipient that contains the photoresist, lowering the threshold power required for photopolymerization [16]. Hence, for the next experiment, nitrogen is bubbled into the photoresist during 10 minutes. The sandwiched configuration of photoresist between two cover slips was used to isolate the photoresist from the surrounding air and prevent further oxygen diffusion. The sample is exposed with the 40x objective at different velocities and at decreasing powers until identifying the minimum power that produces polymerization. Fig. 5:2 (d) shows the resulting threshold powers at different writing speeds for both cases: with and without nitrogen bubbling. At low writing speeds we can find the limit of the threshold power. Below this minimum power threshold, no matter how large the exposure time is, polymerization do not occurs. For writing speeds above 100  $\mu\text{m/s}$ , the threshold power increases with writing speed following the nonlinear dependence. After nitrogen is bubbled, the threshold power versus printing velocity curve moves downwards in the plot shown in Fig. 5:2 and the threshold average power decreases by half (10 mW, corresponding to a peak power of 45  $\text{GW}/\text{cm}^2$ ) compared to the case in which no nitrogen is used (20 mW, corresponding to a peak power of 90  $\text{GW}/\text{cm}^2$ ) as shown in Fig. 5:2 (d) for all writing speeds. Since our method for focusing femtosecond pulses through multimode fibers relies on a diffractive element (a spatial light modulator) and suffers from fiber coupling losses, a lower threshold power for photopolymerization is desired. Therefore, for all subsequent fiber experiments, nitrogen was bubbled into the photoresist prior to polymerization.

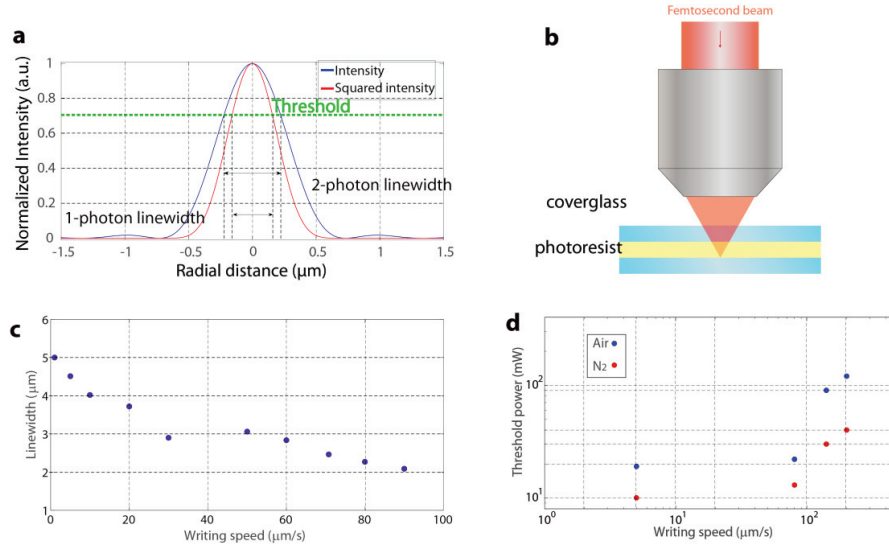


Figure 5:2 Two-photon polymerization with a 40x microscope objective (NA 0.65). (a) Calculated PSFs (one and two-photon). (b) DLW arrangement. (c) Line width dependence on writing speed. (d) Threshold power dependence on writing speed with and without the presence of oxygen.



practice, this is implemented by the quarter wave plates ( $\lambda/4$ ) shown in Fig. 5:3. The first one transforms the linearly polarized beam into a circularly polarized beam and at the other fiber end it transforms the circularly polarized beam coming from the fiber into a linearly polarized beam with same polarization orientation as that of the linearly polarized reference beam used to record the hologram. With this implementation in place, we measured an enhancement of 25% in the spot intensity to background ratio.

The capability to form a sharp bright intensity focus, when focusing light through non-imaging optical elements such as scattering media or multimode optical fibers, depends on the number of degrees of freedom that can be controlled [25]. In the case of the multimode fiber, it depends on the number of modes that can coherently interfere simultaneously through the fiber, which in this case depends on the fiber's diameter, fiber NA and fiber length. Graded index fibers exhibit a smaller temporal multimode broadening when compared to step index fibers [50]. Therefore, they provide a larger number of modes that can be simultaneously controlled to interfere and generate a brighter light focus on the other end of the fiber than using step index fibers. Regarding the fiber length, as the length of the fiber increases, a larger temporal separation occurs between the fiber modes due to modal dispersion, decreasing the number of modes that can be simultaneously controlled with the SLM, generating a spatial focus on the other end with a lower signal to background ratio. The fiber chosen for our experiments is a commercially available graded index fiber from Fiberware GmbH with a 400  $\mu\text{m}$  core diameter, 560  $\mu\text{m}$  cladding diameter, a length of 5 cm and a NA equal to 0.29. We selected this fiber length to produce a light focus whose intensity is close to the threshold for photopolymerization. Using a longer fiber, the light focus generated on the other fiber end would have an intensity below the photopolymerization threshold and thus would not polymerize. The lensed side of the fiber is shown in Fig. 5:9.

In order to enhance the resolution of the 3D printing system we attached a graded index lens of 350  $\mu\text{m}$  diameter to one end of the multimode fiber as shown in the fiber of Fig. 5:3 (a). This increases the numerical aperture of the lensed side of the fiber at the optical axis from 0.29 to 0.54, and reduces the field of view (FOV) of the fiber from 400  $\mu\text{m}$  to 210  $\mu\text{m}$ . An alternative is to build a lens directly on the tip of the fiber as in [51, 52].

As explained above, a beam focused on one side of a multimode optical fiber produces a speckle like pattern on the other side as shown in Fig. 5:4 (a). Therefore, to focus and scan optical pulses through the multimode fiber, we use time-gated digital phase conjugation [41, 42], which consists of two steps: a calibration step that obtains the phase that can be modulated to generate focused spots on the other side of the fiber followed by a reconstruction step that reproduces the phases and generates the spots through the fiber. The fiber is graded index and has a length of 50 mm and a core diameter of 400  $\mu\text{m}$ .

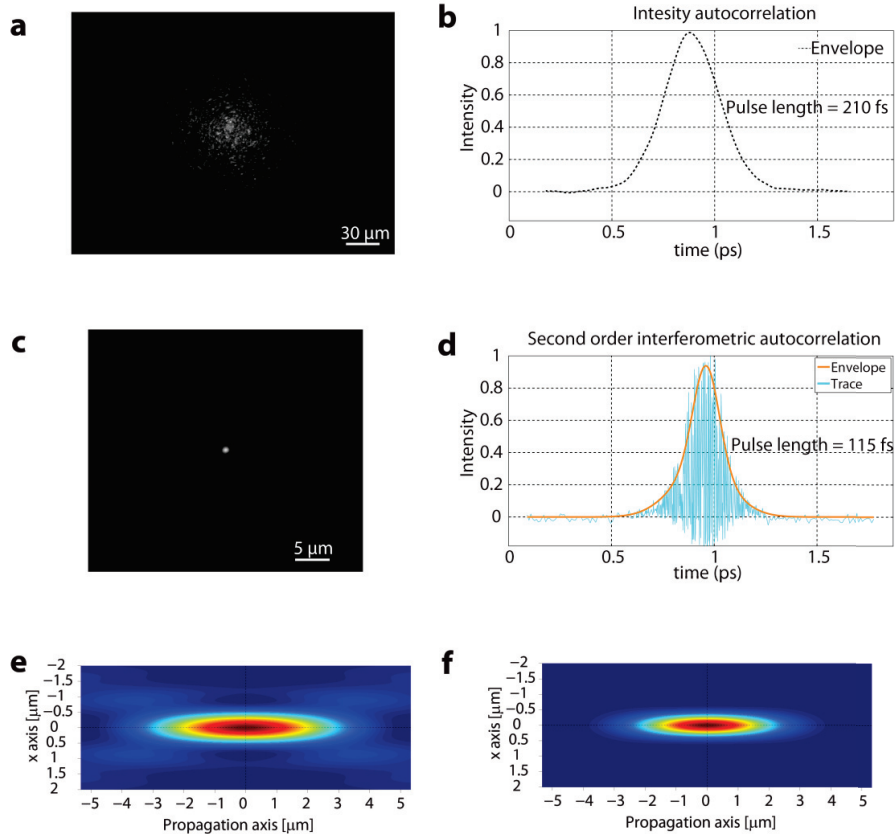


Figure 5:4 Pulsed light transmission through the multimode fiber. (a) Speckle-like pattern produced on one end of the fiber when light is focused with a microscope objective on the other end. (b) Intensity autocorrelation of the speckle like pulse shown in (a). Pulse length is 210 fs. (c) Intensity pattern when light is focused through the fiber using spatial light modulation. (d) Second order interferometric autocorrelation of the spot shown in (c). Pulse length is 115 fs. (e) One-photon 2D PSF of the pulse delivered through the fiber (simulation). (f) Two-photon 2D PSF of the pulse delivered through the fiber (simulation).

The focused pulses generated through the MMF, shown in Fig. 5:4 (c), are 800 times more intense than the average background, with a two-photon spot contrast of 640'000, reducing any possibility that the background intensity will produce any polymerization.

The average pulse length of the pulses focused through the fiber is 115 fs. A sample of those traces is shown in Fig. 5:4 (d). This value is shorter than the 210 fs pulse length that results when no wavefront control is used. This broader pulse is shown in Fig. 5:4 (b).

The maximum average power that our system can deliver through the fiber is 12 mW within the central part of the Airy disk, with a peak power of  $55 \text{ GW}/\text{cm}^2$  corresponding to  $6 \text{ mJ}/\text{cm}^2$  and a pulse energy of 160 pJ.

The pulse lengths of the focused pulses generated through the fiber are measured using second order interferometric autocorrelation. This operation requires the introduction of two replicas of the pulses on the reference arm, which is performed using an interferometer shown in Fig. 5:4 (a). The nonlinearity detection required for this measurement is introduced by fo-

cusing the two replicas of the focused pulses in a two-photon fluorescent sample of PDMS mixed with Rhodamine 6G, which gives the same result as if a second harmonic generation crystal is used [55, 56]. The fluorescent signal propagates through the fiber and is detected by a PMT for each one of the different discrete temporal overlaps between the two replicas of the pulses, resulting in an autocorrelation trace like the one shown in Fig. 5:4 (d). To calculate the value of the pulse length, the  $\text{sech}^2$  pulse shape of the optical pulses is taken into account. For the pulse width measurement in which there is not wavefront control shown in Fig. 5:4 (b) the pulse length is measured using an intensity autocorrelator (Carpe, APE).

## 5.5 Two-photon polymerization at the tip of an ultra-thin needle

After the system is calibrated to focus light through the multimode fiber, the system is able to polymerize over the field of view (FOV) at a 40  $\mu\text{m}$  working distance from the fiber tip. This working distance is selected to prevent the polymerized structure from being attached to the tip of the fiber. The spot is scanned in this plane digitally by changing the phases on the SLM. The vertical scan is performed by a motorized stage that lowers the sample after polymerizing each plane. We use the dip-in arrangement shown in Fig 5:1 (b) in which the fiber is dipped into the photoresist. The photoresist is contained in a recipient, attached to the glass substrate at the bottom. The photoresist is previously bubbled with nitrogen to remove the oxygen that prevents polymerization.

To characterize the polymerization capabilities of our device, we polymerize a grid of voxels separated by 6  $\mu\text{m}$  over a 108  $\mu\text{m}$  diameter FOV. The sample is scanned vertically with a 2  $\mu\text{m}$  step, “printing” one layer of voxels on top of the previous one. The printed rods are shown from above in Fig. 5:5 (a, b), taken with a differential interference contrast microscope (DIC microscope). We print the voxels starting 4  $\mu\text{m}$  inside the glass to ensure the adhesion of the printed structures to the glass substrate even if the sample is slightly tilted.

We measure the full width at half maximum (FWHM) size of the printed rods. We call this value the voxel size or voxel diameter. When focusing light through multimode fibers the numerical aperture depends on the focal position [30]. Additionally, the presence of the graded index lens introduces third order aberrations which become more significant away from the optical axis [42]. This produces a radial dependence of generated spot intensity as a function of position, which in turn leads to a radial dependence of the voxel diameter as shown in Fig. 5:5 (a). Since the exposure dose also affects the voxel size, we perform a radial compensation of exposure in order to equalize the voxel size over the whole field of print (FOP) as shown in Fig. 5:5 (b, c). The small slope of the continuous curve in Fig. 5:5 is produced by the inherent limitation of our phase-only SLM being unable to imprint phase masks faster than a 20 Hz refresh rate, resulting in a non-optimal voxel size compensation for small radii.

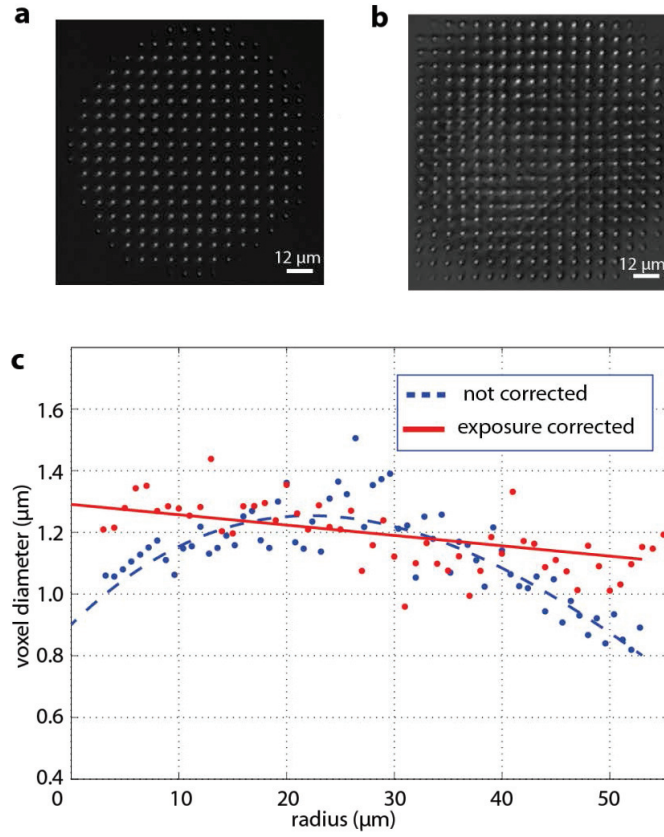


Figure 5:5 Characterization of the 3D printing system. (a) Grid of voxels printed through the multimode fiber. (b) Grid of voxels printed through the multimode fiber in the case of exposure time correction. A radial correction of exposure is applied to polymerize voxels of uniform size. (c) Voxel diameter versus radial position for (a) and (b).

To measure the voxel diameter dependence on exposure, we build the same structure at different exposure times as shown in Fig. 5:6 (a). The voxel diameter versus exposure time curve shown in Fig. 5:6 (c) follows a logarithmic form which corresponds to the exponential decay of the concentration of monomers upon light exposure [53]. At longer exposures, monomers are consumed around the voxel area preventing its growth. The minimum exposure time that we can apply is limited by the refresh rate of the SLM, which is quite low (20 Hz).



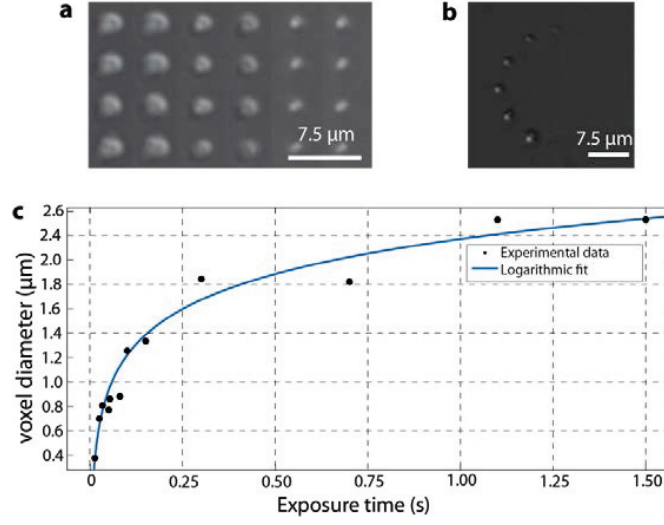


Figure 5:6 Voxel dependence on exposure time. (a-b) Example of voxels printed with 1.5, 1.1, 0.7, 0.3, 0.15, 0.1, 0.05, 0.03, 0.025, 0.0125 seconds of exposure. Scale bars are 7.5 μm. (c) Voxel diameter dependence on exposure time. The logarithmic behavior arises due to an exponential decay of monomer concentration when the photoresists is exposed to light.

To find the smallest spot size without having the slow SLM refresh rate restriction, we designed the following experiment: A circle of 12 voxels at the same radial position of 15 μm separated by an angle of 30° is printed through the fiber. As explained above, without any exposure time correction, the voxel size depends on the radial position. Therefore, in order to keep the same intensity for all the voxels, we build the voxels in a circular arc at a fixed radius. The exposure time per diffraction-limited spot is controlled by setting the motorized stage to different speeds. This way, we can identify the threshold exposure time required for polymerization. The results are shown in Fig. 5:6 (c). The smallest voxel size that we were able to polymerize is 400 nm FWHM, which corresponds to a printing optical resolution of 640 nm. The voxel size can be smaller than the optical resolution due to the threshold behavior of photopolymerization. This is illustrated in Fig. 5:2 (a). If the delivered intensity is slightly above the threshold level, structures with a feature size smaller than the optical resolution can be polymerized. That feature size is called linewidth (see Fig. 5:2 (a) and we refer to its FWHM size as voxel diameter. Intensities below the threshold level are not enough to complete the polymerization and that region of the photoresist is removed in the development process

We clarify that all these measurements were performed before developing the sample, which means that we are not “taking advantage” of the shrinkage effect produced when developing the sample, that can lead to an even better voxel resolution. The shrinkage effect however, is complex to control precisely [54]. Regarding the voxel axial resolution, since the samples were built layer by layer on top of the previous one over exposing the layer below, it cannot be obtained by the polymerized images. To make an indirect estimation, first the two-photon axial resolution has to be calculated. It is given by half of the depth of field:  $d_z = 2.22\lambda/NA^2/\sqrt{2}$ . At the optical axis, it corresponds to a two-photon axial resolution of 4.3 micrometers. However, independent from the nature of the absorption process (two-photon or single-photon), the cross-link of the photoresist is a nonlinear process. Assuming a second or-



der nonlinearity in the photoresist and without taking into account the shrinkage effect, the estimated value of the axial resolution is 3  $\mu\text{m}$ .

## 5.6 The multimode fiber as a 3D printer

Once we are able to polymerize with a uniform voxel resolution over the field of print, we can create arbitrary 3D structures. For instance, we 3D printed a helix of 180 micrometers height. The base of the helix is shown in Fig. 5:7 (a) taken with a DIC microscope as seen from above. A squared scaffold was also manufactured. Figure 5:7 (b,c) shows the scaffold at a height of 0 and 40 micrometers from the base.

Additionally, we created a monolithic model of the Pyramid of Chichén Itzá of 100  $\mu\text{m}$  x 100  $\mu\text{m}$  base size shown in Fig. 5:8. Figure 5:8 (a) shows a DIC image of the undeveloped model. The polymerized photoresists is two-photon fluorescent. Figure 5:8 (b) shows the two-photon image of the developed pyramid at a height of 16 micrometers from its base, taken with a two-photon microscope. The printed pyramid is hollow as seen in the two-photon image. Since the sample is fluorescent, in principle, the printed structure could be visualized, after development, through the same multimode fiber that printed it. For more details on how the fiber can be used as an imaging device, see chapter 4.

Figures 5:8 (c, d) show the scanning electron microscope (SEM) images of the developed model. The lateral printing step used is 1  $\mu\text{m}$  and the axial 2  $\mu\text{m}$ , resulting in a lattice type surface. For a better surface quality, a smaller scanning step could be used. The time required to print this structure was 25 minutes approximately. The printing speed is limited by the refresh rate of the used phase-only SLM (20 Hz).

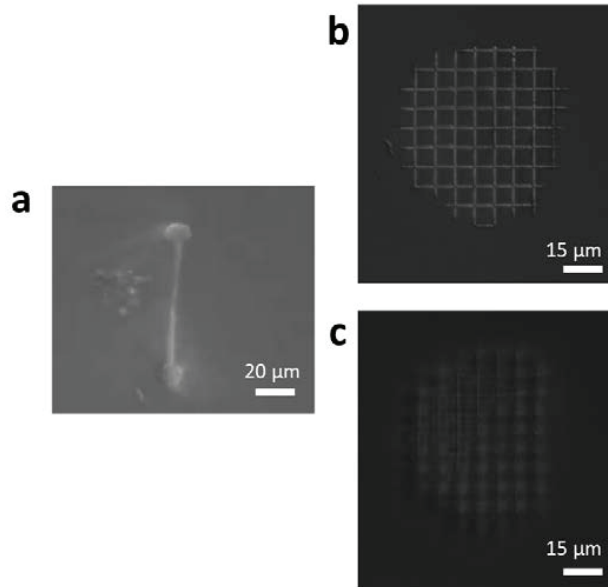


Figure 5:7 3D printed structures. (a) Helix. (b) Base of a scaffold structure. (c) Scaffold structure at a height of 40 micrometers.

To obtain the SEM images, the sample is developed to remove the unexposed photoresist. This is achieved by submerging the sample in Propylene glycol methyl ether acetate (PGMEA) dur-

ing 10 minutes, which is a common developer used in photolithography. Then, the sample is washed with isopropanol. Finally, the sample is coated with a 4 nm gold layer in preparation for the SEM.

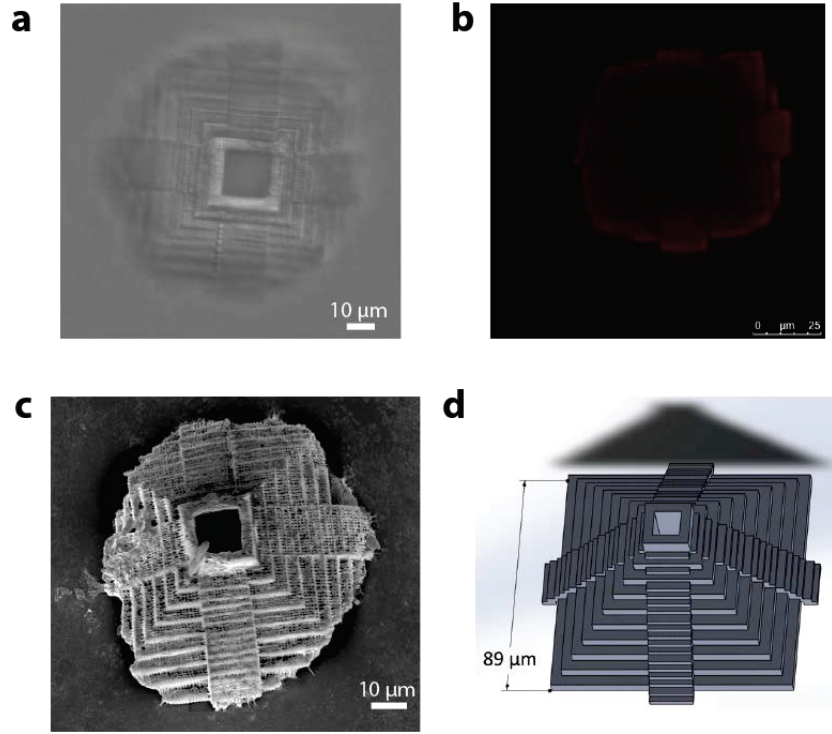


Figure 5:8 Model of the Pyramid of Chichén Itzá 3D printed through a multimode optical fiber. The base diameter is as small as the thickness of a human hair. (a) Image of the pyramid acquired with a differential interference microscope. (b) Two-photon image of the pyramid acquired a 16  $\mu\text{m}$  height from the base. (c,d) Images of the pyramid acquired with a scanning electron microscope.

## 5.7 Discussion on pulsed light focusing through MMFs

There are several methods in addition to time gated phase conjugation to accomplish focusing through turbid media or multimode fibers which can be employed, such as, the measurement of the transmission matrix or iterative methods. In this particular case of multiphoton polymerization through multimode fibers, the power output available in our femtosecond laser gave a peak power at the sample very close to the threshold required for two-photon polymerization. In fact, the threshold average power of 10 mW experimentally measured in our system is close to the 12 mW of maximum average power in the multimode fiber printing system, which corresponds to a peak power of 55 GW/cm<sup>2</sup>. This means that for the projection of more complex light patterns or simultaneous spots through the fiber, generated using the transmission matrix method, a larger power would be required to actually polymerize. Therefore, we used the method of time-gated digital phase conjugation, which is simple but sufficient to generate sequential light foci through the fiber.

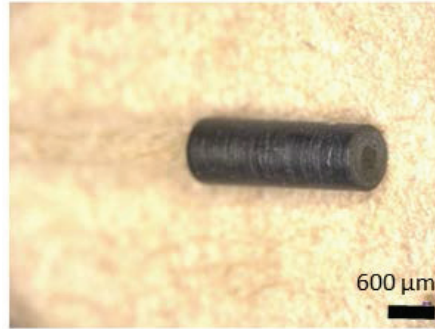


Figure 5:9 Picture of the lensed side of the multimode fiber 3D printing probe. The black case around the fiber and the grin lens holds the fiber and the lens and procures a mechanical stability when the lensed side is manually cleaned after each print. The fiber core and cladding are 400 and 560 micrometers diameter respectively. The fiber length is 5 cm.

The whole potential of the transmission matrix method in 3D printing can be fully exploited in cases where a larger power budget is available, such as in single-photon polymerization or in two-photon polymerization using an amplified laser system. In such cases, two-dimensional light patterns projected on the photoresist could directly polymerize 2D layers, one on top of the previous. The printing speed would then be faster and limited by the refresh rate of the SLM, which is 20 Hz in our case.

## 5.8 Conclusions

In this chapter we demonstrate for the first time additive manufacturing through an ultra-thin probe based on a multimode optical fiber. The fiber is 560  $\mu\text{m}$  diameter, 50 mm long with a minimum voxel size of 400 nm and can microfabricate over a 100  $\mu\text{m}$  diameter field of print. Our method does not have any intrinsic restriction to the height of the printed structure.

The presented 3D printing probe based on a multimode optical fiber does not contain any distal scanning element. Printing is achieved via two-photon polymerization. A focused ultrashort pulse scanned digitally with a SLM from the proximal side can print any arbitrary structure on the other end of the fiber.

The maximum power that we are able to deliver through the fiber is close to the threshold power for polymerization. Therefore, we could only print one voxel at a time. In principle, with a more powerful laser source, we could reconstruct on the SLM simultaneous plane waves either by addition of waves at the SLM point or by projection of 2D light patterns, enabling a faster printing speed, reducing the printing time by a factor of  $N$ , where  $N$  is the number of simultaneous spots generated through the fiber.

This pioneering work enables a new area that we call endofabrication, which consists on the fabrication of micro-structures inside places that are difficult to access by conventional 3D printing devices and that are accessible only through very small apertures.

## 5.9 Acknowledgements

I would like to thank Dr. Miguel A. Modestino from the Laboratory of Optics and the Laboratory of Applied Photonics Devices at EPFL for recording the SEM images. I also thank Dr. Michael Thiel for providing pertinent information about the Nanoscribe IP-L 780 photoresist and the sample development procedure.

## 5.10 References

1. F. Klein, B. Richter, T. Striebel, C. M. Franz, G. von Freymann, M. Wegener, and M. Bastmeyer, "Two-Component Polymer Scaffolds for Controlled Three-Dimensional Cell Culture," *Adv Mater* 23, 1341-1345 (2011).
2. B. Spagnolo, V. Brunetti, G. Lemenager, E. De Luca, L. Sileo, T. Pellegrino, P. P. Pompa, M. De Vittorio, and F. Pisanello, "Three-dimensional cage-like microscavolds for cell invasion studies," *Sci Rep-Uk* 5(2015).
3. M. Vaezi, H. Seitz, and S. F. Yang, "A review on 3D micro-additive manufacturing technologies," *Int J Adv Manuf Tech* 67, 1721-1754 (2013).
4. J. Y. Kim, N. B. Brauer, V. Fakhfour, D. L. Boiko, E. Charbon, G. Grutzner, and J. Brugger, "Hybrid polymer microlens arrays with high numerical apertures fabricated using simple ink-jet printing technique," *Opt Mater Express* 1, 259-269 (2011).
5. H. Yang, C. P. Lin, C. K. Chao, and C. T. Pan, "Hexagonal microlens array fabricated by proximity printing via UV lithography," *Dtip 2003: Design, Test, Integration and Packaging of Mems/Moems 2003*, 356-361 (2003).
6. R. Yang, W. J. Wang, and S. A. Soper, "Out-of-plane microlens array fabricated using ultraviolet lithography," *Appl Phys Lett* 86(2005).
7. B. H. Cumpston, S. P. Ananthavel, S. Barlow, D. L. Dyer, J. E. Ehrlich, L. L. Erskine, A. A. Heikal, S. M. Kuebler, I. Y. S. Lee, D. McCord-Maughon, J. Q. Qin, H. Rockel, M. Rumi, X. L. Wu, S. R. Marder, and J. W. Perry, "Two-photon polymerization initiators for three-dimensional optical data storage and microfabrication," *Nature* 398, 51-54 (1999).
8. M. Deubel, G. Von Freymann, M. Wegener, S. Pereira, K. Busch, and C. M. Soukoulis, "Direct laser writing of three-dimensional photonic-crystal templates for telecommunications," *Nat Mater* 3, 444-447 (2004).
9. M. Malinauskas, A. Zukauskas, V. Purlys, K. Belazaras, A. Momot, D. Paipulas, R. Gadonas, A. Piskarskas, H. Gilbergs, A. Gaidukeviciute, I. Sakellari, M. Farsari, and S. Juodkazis, "Femtosecond laser polymerization of hybrid/integrated micro-optical elements and their characterization," *J Optics-Uk* 12(2010).
10. H. E. Williams, D. J. Freppon, S. M. Kuebler, R. C. Rumpf, and M. A. Melino, "Fabrication of three-dimensional micro-photonic structures on the tip of optical fibers using SU-8," *Opt Express* 19, 22910-22922 (2011).
11. T. Gissibl, M. Schmid, and H. Giessen, "Spatial beam intensity shaping using phase masks on single-mode optical fibers fabricated by femtosecond direct laser writing," *Optica* 3, 448-451 (2016).
12. S. H. Park, T. W. Lim, D. Y. Yang, N. C. Cho, and K. S. Lee, "Fabrication of a bunch of sub-30-nm nanofibers inside microchannels using photopolymerization via a long exposure technique," *Appl Phys Lett* 89(2006).

13. W. C. Lee, Y. J. Heo, and S. Takeuchi, "Wall-less liquid pathways formed with three-dimensional microring arrays," *Appl Phys Lett* 101(2012).
14. H. B. Sun, S. Matsuo, and H. Misawa, "Three-dimensional photonic crystal structures achieved with two-photon-absorption photopolymerization of resin," *Appl Phys Lett* 74, 786-788 (1999).
15. Z. B. Sun, X. Z. Dong, W. Q. Chen, S. Nakanishi, X. M. Duan, and S. Kawata, "Multicolor polymer nanocomposites: In situ synthesis and fabrication of 3D microstructures," *Adv Mater* 20, 914-+ (2008).
16. J. B. Mueller, J. Fischer, F. Mayer, M. Kadic, and M. Wegener, "Polymerization Kinetics in Three-Dimensional Direct Laser Writing," *Adv Mater* 26, 6566-6571 (2014).
17. M. Malinauskas, H. Gilbergs, A. Zukauskas, V. Purlys, D. Paipulas, and R. Gadonas, "A femtosecond laser-induced two-photon photopolymerization technique for structuring micro-lenses," *J Optics-Uk* 12(2010).
18. S. Maruo, O. Nakamura, and S. Kawata, "Three-dimensional microfabrication with two-photon-absorbed photopolymerization," *Opt Lett* 22, 132-134 (1997).
19. B. H. Cumpston, J. E. Ehrlich, S. M. Kuebler, M. Lipson, S. R. Marder, D. McCord-Maughon, J. W. Perry, H. Rockel, and M. Rumi, "Three-dimensional microfabrication using two-photon polymerization," *Materials and Device Characterization in Micromachining* 3512, 168-168 (1998).
20. J. F. Xing, M. L. Zheng, and X. M. Duan, "Two-photon polymerization microfabrication of hydrogels: an advanced 3D printing technology for tissue engineering and drug delivery," *Chem Soc Rev* 44, 5031-5039 (2015).
21. J. F. Xing, X. Z. Dong, W. Q. Chen, X. M. Duan, N. Takeyasu, T. Tanaka, and S. Kawata, "Improving spatial resolution of two-photon microfabrication by using photoinitiator with high initiating efficiency," *Appl Phys Lett* 90(2007).
22. L. J. Li, R. R. Gattass, E. Gershgoren, H. Hwang, and J. T. Fourkas, "Achieving lambda/20 Resolution by One-Color Initiation and Deactivation of Polymerization," *Science* 324, 910-913 (2009).
23. J. Fischer and M. Wegener, "Three-dimensional optical laser lithography beyond the diffraction limit," *Laser Photonics Rev* 7, 22-44 (2013).
24. P. M. Lane, A. L. P. Dlugan, R. Richards-Kortum, and C. E. MacAulay, "Fiber-optic confocal microscopy using a spatial light modulator," *Opt Lett* 25, 1780-1782 (2000).
25. I. M. Vellekoop and A. P. Mosk, "Focusing coherent light through opaque strongly scattering media," *Opt Lett* 32, 2309-2311 (2007).
26. M. Kim, Y. Choi, C. Yoon, W. Choi, J. Kim, Q. H. Park, and W. Choi, "Maximal energy transport through disordered media with the implementation of transmission eigenchannels," *Nat Photonics* 6, 581-585 (2012).
27. D. B. Conkey, A. M. Caravaca-Aguirre, and R. Piestun, "High-speed scattering medium characterization with application to focusing light through turbid media," *Opt Express* 20, 1733-1740 (2012).
28. S. M. Popoff, G. Lerosey, R. Carminati, M. Fink, A. C. Boccara, and S. Gigan, "Measuring the Transmission Matrix in Optics: An Approach to the Study and Control of Light Propagation in Disordered Media," *Phys Rev Lett* 104(2010).
29. I. M. Vellekoop and A. P. Mosk, "Universal optimal transmission of light through disordered materials," *Phys Rev Lett* 101(2008).

30. I. N. Papadopoulos, S. Farahi, C. Moser, and D. Psaltis, "Focusing and scanning light through a multimode optical fiber using digital phase conjugation," *Opt Express* 20, 10583-10590 (2012).
31. I. N. Papadopoulos, S. Farahi, C. Moser, and D. Psaltis, "High-resolution, lensless endoscope based on digital scanning through a multimode optical fiber," *Biomed Opt Express* 4, 260-270 (2013).
32. M. Ploschner, T. Tyc, and T. Cizmar, "Seeing through chaos in multimode fibres," *Nat Photonics* 9, 529-+ (2015).
33. Y. Choi, C. Yoon, M. Kim, T. D. Yang, C. Fang-Yen, R. R. Dasari, K. J. Lee, and W. Choi, "Scanner-Free and Wide-Field Endoscopic Imaging by Using a Single Multimode Optical Fiber," *Phys Rev Lett* 109(2012).
34. D. Loterie, S. Farahi, I. Papadopoulos, A. Goy, D. Psaltis, and C. Moser, "Digital confocal microscopy through a multimode fiber," *Opt Express* 23, 23845-23858 (2015).
35. D. Kim, J. Moon, M. Kim, T. D. Yang, J. Kim, E. Chung, and W. Choi, "Toward a miniature endomicroscope: pixelation-free and diffraction-limited imaging through a fiber bundle," *Opt Lett* 39, 1921-1924 (2014).
36. R. Di Leonardo and S. Bianchi, "Hologram transmission through multi-mode optical fibers," *Opt Express* 19, 247-254 (2011).
37. T. Cizmar and K. Dholakia, "Exploiting multimode waveguides for pure fibre-based imaging," *Nat Commun* 3(2012).
38. T. Cizmar and K. Dholakia, "Shaping the light transmission through a multimode optical fibre: complex transformation analysis and applications in biophotonics," *Opt Express* 19, 18871-18884 (2011).
39. M. Ploschner, B. Straka, K. Dholakia, and T. Cizmar, "GPU accelerated toolbox for real-time beam-shaping in multimode fibres," *Opt Express* 22, 2933-2947 (2014).
40. E. R. Andresen, G. Bouwmans, S. Monneret, and H. Rigneault, "Two-photon lensless endoscope," *Opt Express* 21, 20713-20721 (2013).
41. E. E. Morales-Delgado, S. Farahi, I. N. Papadopoulos, D. Psaltis, and C. Moser, "Delivery of focused short pulses through a multimode fiber," *Opt Express* 23, 9109-9120 (2015).
42. E. E. Morales-Delgado, D. Psaltis, and C. Moser, "Two-photon imaging through a multimode fiber," *Opt Express* 23, 32158-32170 (2015).
43. O. Katz, E. Small, Y. Bromberg, and Y. Silberberg, "Focusing and compression of ultra-short pulses through scattering media," *Nat Photonics* 5, 372-377 (2011).
44. D. B. Conkey, N. Stasio, E. E. Morales-Delgado, M. Romito, C. Moser, and D. Psaltis, "Lensless two-photon imaging through a multicore fiber with coherence-gated digital phase conjugation," *J Biomed Opt* 21(2016).
45. P. R. Forman, F. C. Jahoda, and B. L. Mason, "Multimode Fiber Interferometry with and without Phase Conjugation," *Appl Optics* 30, 1629-1632 (1991).
46. I. McMichael, P. Yeh, and P. Beckwith, "Correction of Polarization and Modal Scrambling in Multimode Fibers by Phase Conjugation," *Opt Lett* 12, 507-509 (1987).
47. I. V. Khudyakov, J. C. Legg, M. B. Purvis, and B. J. Overton, "Kinetics of photopolymerization of acrylates with functionality of 1-6," *Ind Eng Chem Res* 38, 3353-3359 (1999).
48. M. Goppert-Mayer, "Elementary processes with two quantum transitions," *Ann Phys-Berlin* 18, 466-479 (2009).

- 49. E. Andrzejewska, M. B. Bogacki, M. Andrzejewski, and M. Janaszczuk, "Termination mechanism during the photo-induced radical cross-linking polymerization in the presence and absence of oxygen," *Phys Chem Chem Phys* 5, 2635-2642 (2003).
- 50. M. D. Feit and J. A. Fleck, "Light-Propagation in Graded-Index Optical Fibers," *Appl Optics* 17, 3990-3998 (1978).
- 51. S. Bianchi and R. Di Leonardo, "A multi-mode fiber probe for holographic micromanipulation and microscopy," *Lab Chip* 12, 635-639 (2012).
- 52. T. Gissibl, S. Thiele, A. Herkommer, and H. Giessen, "Two-photon direct laser writing of ultracompact multi-lens objectives," *Nat Photon* 10, 554-560 (2016).
- 53. S. Kawata, H. B. Sun, T. Tanaka, and K. Takada, "Finer features for functional micro-devices - Micromachines can be created with higher resolution using two-photon absorption.," *Nature* 412, 697-698 (2001).
- 54. L. J. Jiang, J. H. Campbell, Y. F. Lu, T. Bernat, and N. Petta, "Direct Writing Target Structures by Two-Photon Polymerization," *Fusion Sci Technol* 70, 295-309 (2016).
- 55. M. Muller, J. Squier, and G. J. Brakenhoff, "Measurement of Femtosecond Pulses in the Focal Point of a High-Numerical-Aperture Lens by 2-Photon Absorption," *Opt Lett* 20, 1038-1040 (1995).
- 56. O. Lammel and A. Penzkofer, "Femtosecond pulse duration measurement by two-photon fluorescence detection," *Optical and Quantum Electronics* 32, 1147-1160 (2000).





# Chapter 6 Conclusions and future work

## 6.1 Achieved results

This thesis deals with the control of light propagation through multimode optical fibers with applications in two-photon imaging and 3D printing.

Before our work, endoscopic two-photon imaging was restricted to thick and short graded index lenses or fiber bundles with limited resolution. With our work, we have enabled high resolution two-photon imaging through ultra-thin multimode fibers of 200  $\mu\text{m}$  core diameter and up to 20 cm length.

Regarding 3D printing, two-photon polymerization was technologically restricted to very large printing objectives of several centimeters in diameter unable to reach small places. With our work we have disrupted such limitation enabling 3D printing through ultra-thin needles of 560  $\mu\text{m}$  in diameter, allowing microfabrication through small apertures and cavities.

The following section presents a general summary of what is presented in each chapter.

Chapter 2 presents two methods for monochromatic light focusing through multimode fibers based on spatial light modulation: Digital phase conjugation and the measurement of the optical transmission matrix. Advantages and disadvantages of each method are discussed as well as the applications and challenges of light-modulation based scanning through multimode fibers.

In chapter 3, the method of digital phase conjugation introduced in chapter 2 is extended to the broadband case. We call it time-gated digital phase conjugation and allows focusing and scanning of light pulses with hundreds of femtosecond in pulse length through multimode optical fibers. Scanning does not require any mechanical element on the distal side of the fiber. This method reduces temporal broadening due to modal dispersion and allows the delivery of focused pulses with high peak powers. The presented work enables two-photon absorption at the tip of an ultra-thin needle.

In chapter 4 we demonstrate how, with the use of an adequate pulsed light source with 100 fs pulse length centered at a 800 nm wavelength, the method presented in chapter 3 can be used to conceive a high-resolution two-photon imaging system at the tip of a multimode optical fiber. The proof of principle is simple but powerful: A focused light pulse is scanned over a

fluorescent sample in a 3D scanning volume. For each position of the scanning point, the two-photon fluorescent signal is measured through the fiber and an image is reconstructed. A working prototype and images of biological tissue acquired with the endoscopic system are presented. Our work is the first demonstration of multiphoton imaging through multimode optical fibers.

In chapter 5 we extend the use of our light focusing techniques in a completely different application: two-photon polymerization. We demonstrate for the first time 3D printing through a multimode optical fiber. We call it endofabrication. A working prototype of the 3D printer and printed micro-structures with 500 nm resolution are presented.

## 6.2 Future work

The work presented in this thesis represents a significant progress in two-photon imaging and two-photon polymerization by facilitating their use in places of difficult access reachable through ultra-thin needles. As the result of novel ideas and state of the art research, this work is subject to improvements and can be followed up as mentioned in this section.

The slow refresh rate of the phase spatial light modulators represents a constrain to the applicability of the presented methods for in vivo applications. A future implementation of the presented methods in a commercial device could be reached using a faster spatial light modulator, such as the piston based SLM mentioned in chapter 2. This would allow the demonstration of these methods in real and time in-vivo.

All existing spatial light modulators can only shape either the spatial profile of a light beam, as described in this thesis, or the temporal profile of a light beam as in optical pulse shapers [1, 2]. Their slow refresh rate does not allow their use for simultaneous spatial and temporal modulation of a light beam with hundreds of femtoseconds in pulse length. For phase modulation in the spatial domain, this limitation restricts phase modulation to monochromatic light as in digital phase conjugation. Truthful time reversal cannot be accomplished due to such limitation. This is why we developed the method of time-gated digital phase conjugation which only acts on fiber modes of similar propagation constants in the fiber. The simultaneous coherent control of all fiber modes no matter their propagation speed would require an implementation of a spatio-temporal spatial light modulator. In principle, this could be achieved by constructing a device in which a grating followed by a microlens array forms a pulse shaper after each lens, allowing a discrete spatio-temporal control of a light field. Specific implementation, performance and limitations of such approach are yet to be investigated.

In the imaging and photo-polymerization experiments, commercial graded index and half ball lenses were employed to increase the numerical aperture of the fiber, giving a better resolution for imaging and 3D printing. In a future implementation of the device, a custom built air-spaced objective could be 3D printed directly on the tip of the fiber, as demonstrated in [3]. A custom design could achieve high resolution over a larger field of print. Alternatively, a scattering layer can be placed on the distal end of the fiber as in [4]. Although such scattering layer would affect the collection efficiency of the two-photon fluorescent endoscope, it would be suitable for additive manufacturing.

As shown in [5, 6] light focusing through scattering media has been demonstrated for imaging purposes. A future work could exploit the use of the time-gated transmission matrix of a scattering media to 3D print through it.

### 6.3 References

1. M. Tsang, D. Psaltis, and F. G. Omenetto, "Reverse propagation of femtosecond pulses in optical fibers," *Opt Lett* **28**, 1873-1875 (2003).
2. F. G. Omenetto, B. P. Luce, and A. J. Taylor, "Genetic algorithm pulse shaping for optimum femtosecond propagation in optical fibers," *J Opt Soc Am B* **16**, 2005-2009 (1999).
3. T. Gissibl, S. Thiele, A. Herkommer, and H. Giessen, "Two-photon direct laser writing of ultracompact multi-lens objectives," *Nat Photonics* **10**, 554-+ (2016).
4. I. N. Papadopoulos, S. Farahi, C. Moser, and D. Psaltis, "Increasing the imaging capabilities of multimode fibers by exploiting the properties of highly scattering media," *Opt Lett* **38**, 2776-2778 (2013).
5. O. Katz, E. Small, Y. Bromberg, and Y. Silberberg, "Focusing and compression of ultra-short pulses through scattering media," *Nat Photonics* **5**, 372-377 (2011).
6. I. M. Vellekoop and A. P. Mosk, "Focusing coherent light through opaque strongly scattering media," *Opt Lett* **32**, 2309-2311 (2007).



## Curriculum Vitae

### Edgar E Morales Delgado

Mobile: +41788327433 e-mail: edgar.moralesdelgado@epfl.ch  
Currently at Lausanne, Switzerland



#### Professional expertise

Photonics, laser material processing, additive manufacturing (3D printing), applied sciences, R&D, endoscopy and microscopy, optical networks, wireless networks, optical fibers, programming.

#### Education

**PhD in Sciences: microtechnique and photonics.** École polytechnique fédérale de Lausanne (EPFL)  
March 2013 – February 2017  
Lausanne, Switzerland

**M.Sc. in Electrical Engineering.** King Abdullah University of Science and Technology (KAUST)  
August 2010 – November 2012. GPA: 3.78/4  
Thuwal, Saudi Arabia

**B.Sc. in Telecommunications Engineering.** National Autonomous University of Mexico (UNAM)  
August 2005 – February 2010. GPA: 9.64/10. **First class honors**  
Faculty of Engineering. **Mexico City**, Mexico

**Stanford International Honors Program. Stanford University**  
Summer 2008, Palo Alto, California, USA. (Sponsored by **UNAM**). *Computer science and Artificial Intelligence courses.*

#### Professional experience

**École polytechnique fédérale de Lausanne (EPFL). Doctoral assistant.** (March. 2013 – Feb. 2017)

- Creator of the world's thinnest high resolution 3D printer based on multimode optical fibers. The printer can build structures of hundreds of nanometers in resolution.
- Research and development of a minimally invasive high resolution two-photon endoscope based on multimode optical fibers.

**VentureLab Entrepreneurship Program (at KAUST).** (Sept. 2011 – Aug. 2012)

- Management design and development of an intuitive and secure end to end-encrypted file-sharing platform within the KAUST campus.

**King Abdullah University of Science and Technology (KAUST).** (Jan. – July 2012)

- Master thesis project: Study of strong localization of light in highly disordered systems with FDTD simulations using an IBM Blue Gene supercomputer.
- Design and optimization of the antenna system of an energy harvesting wireless implantable bio-sensor for monitoring the intraocular pressure of the human eye. Summer 2011.

**National Autonomous University of Mexico (UNAM).**

- Undergraduate thesis research project: Invisible watermarking for digital images embedded in the transformed domain with application on copyright protection and steganography. September, 2009 - February, 2010.

**Center for Scientific Research and Higher Education at Ensenada, Mexico (CICESE).**

- Summer research project: Characterization of a piezoelectric actuator. August, 2009.

**Distinctions**

**Government of Mexico City:** Winner of the “Mexico City Engineering Award 2011”

**National Autonomous University of Mexico:** Graduated with first class honors as Telecommunications Engineer. February 2010

**Awarded with the KAUST Discovery Scholarship.** September 2008

**Awarded with the Telmex Foundation Scholarship.** October 2008

**Skills**

- Languages: 

<b>Spanish – Native;</b>	<b>English - Perfect ~ 100%</b>
German – Basic;	French - Basic
- Experience in the design and implementation of complex optical systems for imaging and additive manufacturing (3D printing).
- Experience in the design and use of high resolution microscopes: confocal, multiphoton, DIC.
- Knowledge in optical networks, devices and standardized protocols such as SONET and SDH.
- Experience in the design and simulation of digital wireless and optical communications systems.
- Experience in mobile cellular networks and air interfaces
- Experience in the design and simulation of optical and data systems with Matlab.
- Experience in CAD tools for optics, science and engineering.
- Solid knowledge in Physics and Mathematics.
- Strong abilities using Matlab, C++, php, Java programming languages and mysql.
- Experience using Microsoft Office.

**Peer-reviewed publications and International conferences**

- 4 peer-reviewed publications (three as first author, one as second author).
- 9 oral presentations about my research projects in international conferences.
- 10 proceedings papers.

**Additional Activities**

- **Summer School in Theoretical Physics.** Utrecht University. Summer 2012, Utrecht, Netherlands.
- **Semester in Electrical Engineering.** Rose Hulman Institute of Technology (RHIT) Spring 2010. GPA:3.5/4. *Dean's list* Terre Haute, Indiana, USA. (Sponsored by KAUST)
- **Scientific workshop: Transformations in Optics.** 18-22 May 2015, Leiden Netherlands.
- **University Scholars Leadership Symposium.** Meeting, networking and workshop with young leaders from the Asia-Pacific region. August 2012. Bali, Indonesia.
- **Startup Weekend Riyadh.** October 2011. Riyadh, Kingdom of Saudi Arabia.

**Personal interests and hobbies**

Traveling, golf, paddle boarding, biking and amateur astronomy.

